

Cover Page



Universiteit Leiden



The handle <http://hdl.handle.net/1887/19081> holds various files of this Leiden University dissertation.

Author: Snoeks, Thomas Jan Adriaan

Title: Imaging in pre-clinical cancer research : applied to bone metastases

Date: 2012-06-13



Imaging in Pre-Clinical Cancer Research
applied to bone metastases

Thomas J.A. Snoeks

Imaging in Pre-Clinical Cancer Research

applied to bone metastases

T.J.A. Snoeks

Cover art by T.J.A. Snoeks, based on Figure 2.3.

This thesis was typeset using L^AT_EX 2_ε

Printed by GVO drukkers & vormgevers B.V. Amsterdam, The Netherlands.

ISBN 978-94-6190-845-2

© 2012, T.J.A. Snoeks, 's Gravenhage, The Netherlands. All rights reserved. No parts of this thesis may be reproduced or transmitted in any form, by any means, electronic or mechanical, without prior written permission of the author.

Imaging in Pre-Clinical Cancer Research

applied to bone metastases

Proefschrift

ter verkrijging van de graad van Doctor aan de
Universiteit Leiden, op gezag van Rector Magnificus
prof. mr. P.F. van der Heijden, volgens besluit van het
College voor Promoties te verdedigen op woensdag 13
juni 2012 klokke 16:15 door

Thomas Jan Adriaan Snoeks
geboren te Naarden in 1981

Promotiecommissie

Promotores	Prof. dr. C.W.G.M. Löwik Prof. dr. B.P.F. Lelieveldt
Co-promotores	Dr. E.L. Kaijzel Dr. J. Dijkstra
Overige Leden	Prof. dr. M. Hoehn, Max Planck Instituut, Keulen, Duitsland Prof. dr. F. Ossendorp Prof. dr. S.E. Papapoulos

The studies presented in this thesis have been financially supported by the Dutch Cancer Society, Koningin Wilhelmina Fonds (grant UL2007-3801) and the 6th FP EU grants EMIL (LSH-CT-2004-503569) and DiMI (LSBH-CT-2005-512146) and ctmm project musis.

Financial support for the costs associated with the publication of this thesis was received from the European Society for Molecular Imaging, Caliper Life Sciences, Bontius Stichting Doelfonds Beeldverwerking, J.E. Jurriaanse Stichting and Li-Cor Biosciences.



But there is another alchemy, operative and practical, which teaches how to make the noble metals and colours and many other things better and more abundantly by art than they are made in nature. And science of this kind is greater than all those preceding because it produces greater utilities. For not only can it yield wealth and very many other things for the public welfare, but it also teaches how to discover such things as are capable of prolonging human life for much longer periods than can be accomplished by nature . . . Therefore this science has special utilities of that nature, while nevertheless it confirms theoretical alchemy through its works.

Roger Bacon

Opus Tertium (1266-1268), Chapter 12

Contents

1	General Introduction	9
	Contribution and Outline of this Thesis	16
2	Normalized Volume of Interest Selection and Measurement of Bone Volume in μCT Scans	23
3	Automated Bone Volume and Thickness Measurements in Small Animal Whole-Body μCT Data	41
4	Towards an Integrated Approach for Whole-Body Multimodality Imaging of Bone Metastases	65
5	An <i>in vitro</i> Model That Can Distinguish Between Effects on Angiogenesis and on Established Vasculature: Actions of TNP-470, Marimastat and the Tubulin-Binding Agent Ang-510	83
6	2-Methoxyestradiol Analogue ENMD-1198 Reduces Breast Cancer Induced Osteolysis and Tumor Burden both <i>In Vitro</i> and <i>In Vivo</i>	97
7	Summary & Conclusions and a Future Perspective	119
8	Miscellaneous	133
	Nederlandse Samenvatting	135
	List of Abbreviations	141
	Dankwoord	143
	Curriculum Vitae	145
	List of Publications	147

1

General Introduction

Breast Cancer; a Perspective

Over the last decades, the prognosis of breast cancer has been much improved (Figure 1.1). For instance, the five year survival rate based on all cases registered by the United States Surveillance Epidemiology and End Results (SEER) program in 2001–2007 was 89% compared to 60% in the 1950s.¹ Based on the same SEER data, approximately 12% of the women born in the U.S. today will eventually develop breast cancer during their lifetime.

The chance of survival depends strongly on the stage of the disease at the moment of diagnosis. The 5 year survival rate of breast cancer patients with localized disease is 98% compared to only 23% for patients with distant metastases. This shows that a large number of patients carrying distant metastases cannot be cured. Consequently, treatment of these patients is mainly palliative, aimed at prolonging life and improving the quality of life.^{1,2}

Autopsy revealed bone metastases in approximately 70% off all patients who died of breast cancer.^{3,4} This preference of breast cancer to metastasize to bone, a characteristic shared with prostate cancer, has already been noted by Stephen Paget in 1889. As a metaphor describing this characteristic he wrote that “When a plant goes to seed, its seeds are carried in all directions; but they can only live and grow if they fall on congenial soil”.⁵ This so called seed and soil hypotheses still holds true today, be it slightly rephrased to fit present day scientific knowledge.

Bone metastases are especially difficult to treat due to a strong positive feedback loop between the tumor and the bone micro-environment.⁶ Tools to follow treatment response in a pre-clinical setting of both tumor and bone related processes such as tumor growth, angiogenesis, expression of enzymes and signaling molecules, osteolysis and bone formation are needed in research towards better treatment of bone metas-

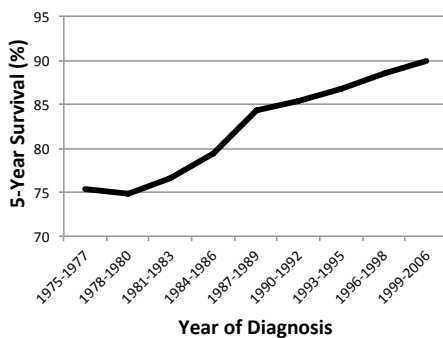


Figure 1.1: Five-year survival of breast cancer patients by year of diagnosis. The five-year survival of all female breast cancer patients has been steadily increasing over the last decades. This can be explained by better treatments on one hand and earlier diagnosis due to extensive mammography screening on the other hand.¹

tases. Only approaches that are capable of following all of these processes will enable a researcher to get a complete understanding in disease progression and treatment efficacy.

Molecular imaging has become one of the main tools in cancer research. The possibility to perform both structural and functional imaging make molecular imaging modalities an attractive research tool. The integrated data handling of different imaging modalities and their possible role in cancer research are discussed within this thesis. The described approaches have been applied in the evaluation of a new compound, ENMD-1198, as possible beneficial compound in the treatment of bone metastases in a pre-clinical mouse model.

Metastatic Bone Disease

Before evaluating the use of various imaging approaches in the field of bone metastases research, it is important to have a general understanding of the biology and pathophysiology of this specific type of metastases. Both breast and prostate cancer have a strong preference to metastasize to bone. In the bone micro-environment, breast cancer is more likely to result in osteolytic lesions while prostate cancer results mainly in osteoblastic lesions, but also mixed lesions exist in some cases.^{7,8} The complications caused by bone metastasis are vast; osteolytic lesions may result in severe bone pain, fracture, life-threatening hypercalcaemia and nerve compression, whereas, osteoblastic lesions can result in severe bone pain or fracture due to the reduced quality of the bone.

There is a multitude of crucial processes during bone metastatic growth. These include tumor growth and tumor–stroma interactions by direct contact and through signaling molecules (reviewed by Lorusso *et al.*⁹ and Mundy¹⁰). The interactions and signaling between the tumor and its direct surroundings result in local pro-angiogenic signaling (reviewed by Voorzanger-Rousselot *et al.*¹¹ and Guise *et al.*¹²), local activation and infiltration of the innate immune system and local suppression of the adaptive immune system (reviewed by Lin *et al.*¹³). All of these processes have a positive feedback on tumor growth. Moreover, the skeletal metastatic sites are often characterized by a distortion of the delicate balance in bone turnover leading to osteolytic and/or osteoblastic lesions at the metastatic tumor site.

A Vicious Cycle

The bone matrix holds an abundant store of growth factors, which are released during bone resorption. Many different cell types are involved in the process of bone metastatic growth: tumor cells, endothelial cells and stromal cells, plus the bone specific osteoblasts and osteoclasts and their precursors. Each of these cell types fulfill their own key role in the context of bone metastasis.

Once settled in the bone micro-environment, breast cancer cells are capable of releasing various signaling molecules such as, bone morphogenic proteins (BMPs),

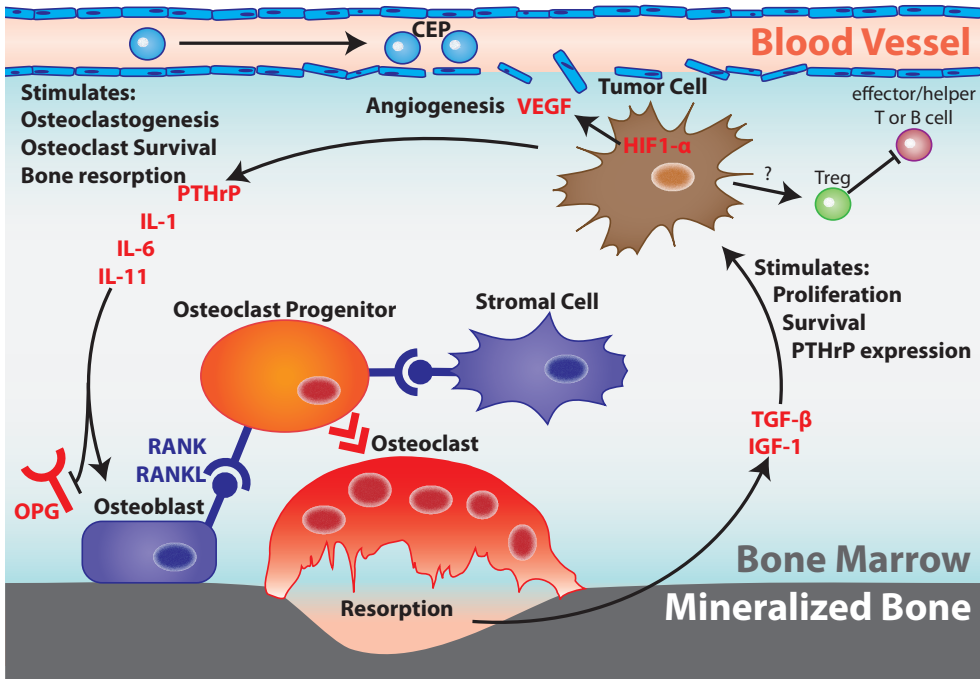


Figure 1.2: Schematic representation of the vicious cycle of bone metastasis. Tumor cells stimulate Osteoblasts and stromal cells to express RANKL by producing osteolytic factors as PTHrP, IL-1, IL-6 and IL-11. These factors lead to a downregulation in OPG expression, an inhibitor of RANKL. In turn, RANKL results in increased osteoclastogenesis and osteoclast survival. Mineralized bone matrix is rich in cytokines and growth factors including TGF-β. These factors are released in the bone marrow space upon bone resorption by osteoclasts. In turn, these factors stimulate tumor cell survival, growth, and production of PTHrP and other osteolytic factors which further stimulate osteoclastic resorption. In addition, bone metastases are generally hypoxic leading to an upregulation of HIF-1α and secretion of VEGF, a strong pro-angiogenic factor. CEPs are attracted by leaky tumor vasculature and further stimulates angiogenesis. Tumors recruit Treg cells via a mechanism which is largely unknown. Treg cells inhibit possible immune reactions against the tumor through the downregulation of T & B effector and helper cells.^{6,10,14}

insulin-like growth factors (IGFs), transforming growth factor- β (TGF- β) and parathyroid hormone-related protein (PTHrP), which in themselves have an effect on bone.^{7,15} PTHrP is a signaling molecule involved in mammary gland development and lactation, hence, its strong presence both in the healthy breast as well as in breast cancer. In addition, PTHrP is involved in many other processes as signaling molecule, amongst which the maintenance of a calcium homeostasis.^{16–18} These multiple functions of PTHrP are at the core of the pathogenesis of osteolytic bone metastases of breast cancer.

PTHrP, released locally in the bone by metastases, stimulates the expression of receptor activator for nuclear factor- κ B ligand (RANKL) on neighboring bone marrow stromal cells and osteoblasts.¹⁰ RANKL signaling stimulates the maturation of osteoclasts from RANK positive precursor cells. Moreover, RANKL prolongs the survival of mature, active, osteoclasts.¹⁹ Osteoclasts resorb the mineralized bone matrix, which in turn causes the release and activation of growth factors and cytokines present in the bone. TGF- β is such a factor which is highly present in bone.^{20,21}

The released TGF- β stimulates tumor cells to produce more osteolytic factors (PTHrP, IL-6, IL-11) that can, in turn, further stimulate osteoclastic resorption and increase the TGF- β release from bone.^{6,20,22} This feed-forward stimulation of osteoclastic bone resorption is referred to as the “vicious cycle” of bone metastasis (Figure 1.2).^{15,22–24} The strong positive feedback between bone destruction and metastatic growth makes these lesions nearly impossible to treat.^{10,14} The local bone destruction is the main cause of morbidity in metastatic bone disease.

Tumor Angiogenesis

Tumors cannot grow without sufficient blood supply making angiogenesis a critical process in tumor growth. In the adult, angiogenesis is a tightly regulated process occurring almost exclusively during wound healing and in ischemic areas. However, at a certain point during tumor growth there is a shift of balance towards angiogenesis. This shift has been called the “angiogenic switch”, a result of crosstalk between the tumor and surrounding healthy tissue.²⁵

In the case of bone metastases, angiogenesis is strongly driven by hypoxia. Hypoxia and the stabilization of hypoxia inducible factor-1 α (HIF-1 α) as a key initiators of (tumor-)angiogenesis has been studied extensively and reviewed by Liao and Johnson.²⁶ VEGF is one of the downstream targets of hypoxia signaling and the main factor involved in pro-angiogenic signaling.²⁷ Most of the vasculogenic and angiogenic effects of VEGF are mediated through the VEGF receptor 1 (VEGFR1, FLT-1) and VEGF receptor 2 (VEGFR2, Flk-1) expressed on endothelial cells.²⁸ During angiogenesis, including tumor angiogenesis, both VEGF and VEGFR2 expression are locally upregulated.^{29,30}

The one sided pro-angiogenic, mainly VEGF mediated, signaling leads to the formation of an abnormal vascular network. The newly formed vessels are leaky, tortuous and often lack pericytes and a basement membrane.^{31,32} Leaky, poorly formed,

vasculature and high levels of VEGF attract circulating endothelial progenitor cells (CEPs). These cells are able to differentiate into endothelial cells and are normally involved in vessel repair, angiogenesis and neo-vascularization, adding up to the already existing pro-angiogenic environment (Figure 1.2).^{33,34}

Molecular Imaging

Molecular imaging is the term used to describe a wide range of imaging tools and techniques that enable the visualization of molecular processes and interactions (functional imaging) or structures and micro-architecture (structural imaging). Molecular imaging modalities can be based on light (e.g. optical imaging), on the use of radioactive tracers (e.g. PET and SPECT), on the use of ultrasound or on differences in magnetic resonance (e.g. MRI). These functional imaging modalities can be combined with structural imaging modalities which provide more anatomical detail such as radiography or computed tomography (CT).

When performing research on bone metastases, it is important to follow both structural and functional developments in and around the tumor. Structural imaging modalities are used to follow diseased induced changes to the skeleton whereas functional imaging is to follow processes such as matrix degeneration, tumor angiogenesis and tumor growth. The non-invasive character of optical imaging, imaging modalities based on detection of light, makes it possible to follow animals over time throughout the experimental period.

Whole Body Optical Imaging

Optical imaging of cancer presents a challenge because tumor cells usually do not have a specific optical quality that clearly distinguishes them from normal tissue. However, the field of whole body optical imaging has been transformed over the last decades by improvements in camera detection systems as well as better tools for making clonal cell lines or transgenic animal models with light-generating capabilities or specific fluorescent properties.

The term optical imaging includes all of the imaging techniques based on the detection of photons with wavelengths in the ultraviolet, visible, near-infrared and infrared parts of the spectrum. These photons are emitted from living cells, tissues or animals through either bioluminescence or fluorescence. As a result, optical imaging can be divided in: bioluminescence imaging (BLI) and fluorescence imaging (FLI). Despite the similarities in their applications, BLI and FLI both have their own characteristics, strengths and weaknesses such as differences in availability, sensitivity, signal to noise ratio (SNR) and interference by background emission from tissues.^{35–38}

The choice of tools, such as whether to use FLI or BLI, is determined by the questions needing to be addressed, e.g. FLI allows total cells *in vivo* to be measured as well as *in vitro* and *ex vivo* analysis to be performed whereas BLI often gives an

indication of metabolizing cell activity. Therefore, BLI has evolved into a standard modality in pre-clinical research to follow tumor growth non-invasively over time.

X-rays and μ CT

X-rays dominated the field of skeletal imaging ever since Rontgen's publication of a photo of his wife's hand and various other shadow images in Science back in 1896.³⁹⁻⁴¹ The subsequent work of people like Alessandro Vallebona and William Watson formed the basis of X-ray tomography. It is during the 1970s that X-ray-based imaging underwent revolutionary changes after advances in digital computing enabled the development of CT by Godfrey Hounsfield.^{42,43}

Radiographs of small animals are made in the same way as their human counterpart. The technique is not much different from the method described by Röntgen. The subject is placed between a concealed photographic film or digital X-ray camera and an X-ray point source. The recorded image is a two dimensional (2D) shadow projection of the subject.

Relatively new are specialized small animal μ CT scanners. These machines can produce high resolution three dimensional (3D) datasets of *in vivo* and *ex vivo* specimens. In general, 3D methodologies are preferable over their 2D counterparts as they give a better approximation of the real life situation. Moreover, μ CT can potentially be used to quantify osteoblastic lesions as well as osteolytic lesions, something that is not possible with radiography. However, data analysis of 3D datasets can be tedious and only few standardized protocols for data analysis are in place since the imaging techniques are relatively new.⁴⁴⁻⁴⁷

Contribution and Outline of this Thesis

The aim of this work was to develop methods to measure structural changes in the skeleton using μ CT. In addition, these new methods should be able to quantify biologically relevant changes. In order to do this, normalized methods to analyze μ CT scans and perform quantitative measurements within these datasets are described in this thesis. These techniques were combined with a biological angiogenesis assay and used as research tools in a study comparing various different combination treatments of bone metastases.

Chapter 2 describes a manual μ CT based method to assess specific changes in bone volume. The method allows the user to select normalized volumes of interest based on manual input. In addition, the user can generate normalized cross sections and longitudinal sections for side-by-side presentations, comparison of cortical thickness and validation of histological findings.

Chapter 3 describes an automated μ CT based method to assess disease induced changes in bone volume and thickness. The segmentation and volume measurements are fully automated in order to minimize observer bias. The segmentation algorithm is able to find the region of interest in whole-body rodent μ CT scans, regardless of the animal posture during the scan. The exact location of volumetric changes can be assessed using automatically generated color coded cortical thickness maps.

Chapter 4 gives an overview of the advances made by the LUMC departments of Endocrinology and Radiology - Image Processing (LKEB) in multi-modality molecular imaging with an emphasis on μ CT. This puts Chapters 2 and 3 in a broader perspective by linking μ CT to other imaging modalities.

Chapter 5 describes an angiogenesis assay. The assay enables the differentiation between anti-angiogenic and vascular disrupting properties of compounds. In addition, the assay will indicate the main mechanism underlying the anti-angiogenic properties.

Chapter 6 discusses the efficacy of the suggested combination treatment consisting of ENMD-1198, "metronomic" cyclophosphamide and bisphosphonates. In addition, this chapter is exemplary on how the described angiogenesis assay, μ CT quantification techniques, radiographs and optical imaging can be combined in a set of experiments to answer biological questions and assess treatment efficacy.

References

1. Surveillance, epidemiology, and end results (seer) program. <http://www.seer.cancer.gov/> - Total U.S., 1969-2009 Counties, National Cancer Institute, DCCPS, Surveillance Research Program, Cancer Statistics Branch, 2011 Apr.
2. DeSantis C, Jemal A, Ward E, and Thun MJ. Temporal trends in breast cancer mortality by state and race. *Cancer Causes Control*, 2008 Jun;19(5):537-45.
3. Abrams HL, Spiro R, and Goldstein N. Metastases in carcinoma; analysis of 1000 autopsied cases. *Cancer*, 1950 Jan;3(1):74-85.
4. Coleman RE. Clinical features of metastatic bone disease and risk of skeletal morbidity. *Clin Cancer Res*, 2006 Oct;12(20 Pt 2):6243s-6249s.
5. Paget S. The distribution of secondary growths in cancer of the breast. *Lancet*, 1889; 1:571-3.
6. Guise TA, Mohammad KS, Clines G, Stebbins EG, Wong DH, Higgins LS, Vessella R, Corey E, Padalecki S, Suva L, and Chirgwin JM. Basic mechanisms responsible for osteolytic and osteoblastic bone metastases. *Clin Cancer Res*, 2006 Oct;12(20 Pt 2):6213s-6216s.
7. Reddi AH, Roodman D, Freeman C, and Mohla S. Mechanisms of tumor metastasis to the bone: challenges and opportunities. *J Bone Miner Res*, 2003 Feb;18(2):190-4.
8. Roodman GD. Mechanisms of bone metastasis. *N Engl J Med*, 2004 Apr;350(16):1655-64.
9. Lorusso G and Rüegg C. The tumor microenvironment and its contribution to tumor evolution toward metastasis. *Histochem Cell Biol*, 2008 Dec;130(6):1091-103.
10. Mundy GR. Metastasis to bone: causes, consequences and therapeutic opportunities. *Nat Rev Cancer*, 2002 Aug;2(8):584-93.
11. Voorzanger-Rousselot N, Juillet F, Mareau E, Zimmermann J, Kalebic T, and Garnero P. Association of 12 serum biochemical markers of angiogenesis, tumour invasion and bone turnover with bone metastases from breast cancer: a cross-sectional and longitudinal evaluation. *Br J Cancer*, 2006 Aug;95(4):506-14.
12. Guise TA and Chirgwin JM. Transforming growth factor-beta in osteolytic breast cancer bone metastases. *Clin Orthop Relat Res*, 2003 Oct;415(Suppl):S32-8.
13. Lin WW and Karin M. A cytokine-mediated link between innate immunity, inflammation, and cancer. *J Clin Invest*, 2007 May;117(5):1175-83.
14. Guise TA and Mundy GR. Cancer and bone. *Endocr Rev*, 1998 Feb;19(1):18-54.
15. Kang Y, Siegel PM, Shu W, Drobnjak M, Kakonen SM, Córdón-Cardo C, Guise TA, and Massagué J. A multigenic program mediating breast cancer metastasis to bone. *Cancer Cell*, 2003 Jun;3(6):537-49.

16. Allgrove J. Physiology of calcium, phosphate and magnesium. *Endocr Dev*, 2009; 16:8–31.
17. Datta NS and Abou-Samra AB. Pth and pthrp signaling in osteoblasts. *Cell Signal*, 2009 Aug;21(8):1245–54.
18. Mamillapalli R, VanHouten J, Zawalich W, and Wysolmerski J. Switching of g-protein usage by the calcium-sensing receptor reverses its effect on parathyroid hormone-related protein secretion in normal versus malignant breast cells. *J Biol Chem*, 2008 Sep; 283(36):24435–47.
19. Boyce BF and Xing L. Functions of rank/rank/opg in bone modeling and remodeling. *Arch Biochem Biophys*, 2008 May;473(2):139–46.
20. Kiriya T, Gillespie MT, Glatz JA, Fukumoto S, Moseley JM, and Martin TJ. Transforming growth factor beta stimulation of parathyroid hormone-related protein (pthrp): a paracrine regulator? *Mol Cell Endocrinol*, 1993 Mar;92(1):55–62.
21. Pivonka P, Zimak J, Smith DW, Gardiner BS, Dunstan CR, Sims NA, Martin TJ, and Mundy GR. Model structure and control of bone remodeling: a theoretical study. *Bone*, 2008 Aug;43(2):249–63.
22. Yin JJ, Selander K, Chirgwin JM, Dallas M, Grubbs BG, Wieser R, Massagué J, Mundy GR, and Guise TA. Tgf-beta signaling blockade inhibits pthrp secretion by breast cancer cells and bone metastases development. *J Clin Invest*, 1999 Jan;103(2):197–206.
23. Deckers M, van Dinther M, Buijs J, Que I, Löwik C, van der Pluijm G, and ten Dijke P. The tumor suppressor smad4 is required for transforming growth factor beta-induced epithelial to mesenchymal transition and bone metastasis of breast cancer cells. *Cancer Res*, 2006 Feb;66(4):2202–9.
24. Kang Y, He W, Tulley S, Gupta GP, Serganova I, Chen CR, Manova-Todorova K, Blasberg R, Gerald WL, and Massagué J. Breast cancer bone metastasis mediated by the smad tumor suppressor pathway. *Proc Natl Acad Sci U S A*, 2005 Sep;102(39):13909–14.
25. Hanahan D and Folkman J. Patterns and emerging mechanisms of the angiogenic switch during tumorigenesis. *Cell*, 1996 Aug;86(3):353–64.
26. Liao D and Johnson RS. Hypoxia: a key regulator of angiogenesis in cancer. *Cancer Metastasis Rev*, 2007 Jun;26(2):281–90.
27. Iliopoulos O, Levy AP, Jiang C, Kaelin WG Jr, and Goldberg MA. Negative regulation of hypoxia-inducible genes by the von hippel-lindau protein. *Proc Natl Acad Sci U S A*, 1996 Oct;93(20):10595–9.
28. Millauer B, Wizigmann-Voos S, Schnürch H, Martinez R, M°ller NP, Risau W, and Ullrich A. High affinity vegf binding and developmental expression suggest flk-1 as a major regulator of vasculogenesis and angiogenesis. *Cell*, 1993 Mar;72(6):835–46.

29. Rissanen TT, Vajanto I, Hiltunen MO, Rutanen J, Kettunen MI, Niemi M, Leppänen P, Turunen MP, Markkanen JE, Arve K, Alhava E, Kauppinen RA, and Ylä-Herttuala S. Expression of vascular endothelial growth factor and vascular endothelial growth factor receptor-2 (kdr/flk-1) in ischemic skeletal muscle and its regeneration. *Am J Pathol*, 2002 Apr;160(4):1393–403.
30. Vajkoczy P, Farhadi M, Gaumann A, Heidenreich R, Erber R, Wunder A, Tonn JC, Menger MD, and Breier G. Microtumor growth initiates angiogenic sprouting with simultaneous expression of vegf, vegf receptor-2, and angiopoietin-2. *J Clin Invest*, 2002 Mar;109(6):777–85.
31. Carmeliet P and Jain RK. Angiogenesis in cancer and other diseases. *Nature*, 2000 Sep;407(6801):249–57.
32. Eberhard A, Kahlert S, Goede V, Hemmerlein B, Plate KH, and Augustin HG. Heterogeneity of angiogenesis and blood vessel maturation in human tumors: implications for antiangiogenic tumor therapies. *Cancer Res*, 2000 Mar;60(5):1388–93.
33. Rabelink TJ, de Boer HC, de Koning EJP, and van Zonneveld AJ. Endothelial progenitor cells: more than an inflammatory response? *Arterioscler Thromb Vasc Biol*, 2004 May;24(5):834–8.
34. Asahara T, Masuda H, Takahashi T, Kalka C, Pastore C, Silver M, Kearne M, Magner M, and Isner JM. Bone marrow origin of endothelial progenitor cells responsible for postnatal vasculogenesis in physiological and pathological neovascularization. *Circ Res*, 1999 Aug;85(3):221–8.
35. Snoeks TJA, Löwik CWGM, and Kaijzel EL. 'in vivo' optical approaches to angiogenesis imaging. *Angiogenesis*, 2010 Jun;13(2):135–47.
36. Snoeks TJA, Khmelinskii A, Lelieveldt BPF, Kaijzel EL, and Löwik CWGM. Optical advances in skeletal imaging applied to bone metastases. *Bone*, 2011 Jan;48(1):106–14.
37. Taroni P, Pifferi A, Torricelli A, Comelli D, and Cubeddu R. In vivo absorption and scattering spectroscopy of biological tissues. *Photochem Photobiol Sci*, 2003 Feb;2(2):124–9.
38. Weissleder R and Ntziachristos V. Shedding light onto live molecular targets. *Nat Med*, 2003 Jan;9(1):123–8.
39. Goodspeed AW. Experiments on the rontgen x-rays. *Science*, 1896 Feb;3(59):236–7.
40. Pupin MI. Rontgen rays. *Science*, 1896 Feb;3(59):231–5.
41. Röntgen WC. On a new kind of rays. *Science*, 1896 Feb;3(59):227–31.
42. Ambrose J and Hounsfield G. Computerized transverse axial tomography. *Br J Radiol*, 1973 Feb;46(542):148–9.
43. Hounsfield GN. Computerized transverse axial scanning (tomography). 1. description of system. *Br J Radiol*, 1973 Dec;46(552):1016–22.

44. Bussard KM and Mastro AM. Ex-vivo analysis of the bone microenvironment in bone metastatic breast cancer. *J Mammary Gland Biol Neoplasia*, 2009 Dec;14(4):387–95.
45. Johnson LC, Johnson RW, Munoz SA, Mundy GR, Peterson TE, and Sterling JA. Longitudinal live animal micro-ct allows for quantitative analysis of tumor-induced bone destruction. *Bone*, 2011 Jan;48(1):141–51.
46. Kaijzel EL, Snoeks TJA, Buijs JT, van der Pluijm G, and Löwik CWGM. Multimodal imaging and treatment of bone metastasis. *Clin Exp Metastasis*, 2009;26(4):371–9.
47. Kok P, Baiker M, Hendriks EA, Post FH, Dijkstra J, Löwik CWGM, Lelieveldt BPF, and Botha CP. Articulated planar reformation for change visualization in small animal imaging. *IEEE Trans Vis Comput Graph*, 2010;16(6):1396–404.

2

Normalized Volume of Interest Selection and Measurement of Bone Volume in μ CT Scans

Thomas J.A. Snoeks¹
Eric L. Kaijzel¹
Ivo Que¹
Isabel M. Mol¹
Clemens W.G.M. Löwik¹
Jouke Dijkstra²

Bone. 2011 Sep 16. [Epub ahead of print]

¹Dept. of Endocrinology, LUMC, Leiden, The Netherlands

²Dept. of Radiology, Division of Image Processing LKEB, LUMC, Leiden, The Netherlands

Abstract

Quantification of osteolytic lesions in bone is pivotal in the research of metastatic bone disease in small animal models. Osteolytic lesions are quantified using two dimensional X-ray photographs, which often neglects to take into account any changes in three dimensional structure. Furthermore, measurement errors are inadvertently introduced when a region of interest with predefined dimensions is used during μ CT analysis. To study osteolytic processes, a normalized method of selecting a region of interest is required. Here we describe a new method to select volumes of interest in a normalized way regardless of curvature, fractures or dislocations within the bone. In addition, this method enables the user to visualize normalized cross-sections in an exact 90° angle or along the longitudinal axis of bone, at any given point. As a result, the user can compare measurements of diameter, volume and structure between different bones in a normalized manner.

Introduction

Certain types of cancer preferentially metastasize to bone. In cases of breast cancer, *post mortem* examination revealed that over 70% of the patients carried bone metastases.¹ Bone metastases are the cause of severe morbidity.²⁻⁴ As a result, much research is being conducted toward an optimal treatment regimen. Therefore, quantification of osteolytic lesion size and treatment evaluation in small animal models are pivotal for preclinical research in being able to characterize metastatic bone disease.

At present, osteolytic lesions are quantified using two dimensional (2D) radiographs.^{5,6} The scoring of radiographs is performed by manual drawing of a region of interest (ROI) around the lesion, a method prone to observer bias. This procedure cannot be automated because of high variability of shape and grey-values of the bones and lesions. The grey-value intensity of the lesion depends heavily on the location of the lesion and the chance of multiple lesions being projected on top of each other. The shape of the bone itself can be altered drastically due to fractures or the bone can even be partially destroyed in case of severe osteolytic lesions, making the reproducible selection of a ROI more difficult. Small lesions and subtle changes in bone thickness are not visible or easily overlooked.

μ CT scans provide three dimensional (3D) structural information which allows a more exact assessment of the disease-induced changes. In contrast to conventional radiography, μ CT scans can be used to quantify both the decrease in bone volume in case of osteolysis as well as the increase in bone volume in case of osteoblastic lesions. However, analysis of μ CT scans is difficult and time consuming.

A normalized method of selecting a region of interest is required in order to study volumetric changes. The murine tibia for instance, is slightly curved in a healthy state. This curved shape makes it impossible to make a μ CT scan composed entirely of slices that are perpendicular to the center-line of the bone. In the case of severe osteolysis, parts of the bone might be missing or fractured increasing the complexity of volume of interest (VOI) selection. Therefore, the μ CT scan must be reformatted in order to be able to perform a normalized selection of a VOI independent of the scan orientation.

Here we describe a new method to reformat μ CT scans and select a VOI in a normalized way regardless of curvature, fractures or dislocations within the bone. This method makes use of curved planar reformation along a center-line defined by the user. The selection of the VOI was performed in this reformatted μ CT scan. To prevent any measurement errors introduced by the reformation, the actual volume measurements of the selected VOI are performed in the original scan volume. In addition, we can visualize normalized cross-sections at an exact 90° angle or along the longitudinal axis of bone, at any given point. This method allows side-by-side visualizations of cross-sections and enables the comparison of diameter and volume measurements between different scans in a normalized manner.

Materials & methods

Animals

Female athymic mice (BALB/c nu/nu, 5 weeks old) mice were acquired from Charles River (Charles River, L'Arbresle, France), housed in individually ventilated cages while food and water were provided *ad libitum*. All surgical and analytical procedures were performed under isoflurane gas anesthesia. At the end of the experimental period, animals were sacrificed by cervical dislocation. Animal experiments were approved by the local committee for animal health, ethics and research of Leiden University Medical Center.

Cell lines & culture conditions

The MDA-231-B/Luc+ cell line (hereafter MDA-BO2), a bone-seeking and luciferase-expressing subclone from the human breast cancer MDA-MB-231,^{7,8} was cultured in DMEM (Invitrogen, Carlsbad, CA USA) containing 4.5 g glucose/l supplemented with 10% fetal calf serum (FCS) (Lonza, Basel, Switzerland), 100 units/ml penicillin, 50 µg/ml streptomycin (Invitrogen) and 800 µg/ml geneticin/G418 (Invitrogen). Cultures were maintained in a humidified incubator at 37°C and 5% CO₂.

Experimental setup

Intra-osseous inoculations with MDA-BO2 cells and sham operations; Mice received an intra-osseous inoculation with MDA-BO2 cells ($n = 8$) into the right tibia as described previously.⁸ After 42 days, mice were sacrificed by cervical dislocation and the hind limbs were fixed overnight in 4% formaldehyde. Mice in the sham operated group (partial bone marrow ablation) underwent the same procedure as the MDA-BO2 inoculated animals except that the intra-osseous injection contained only PBS and no tumor cells. After 10 and 42 days mice were sacrificed by cervical dislocation ($n = 5$), the hind limbs were fixed.

Bisphosphonate treatment

Mice received daily sub-cutaneous injections with risedronic acid (150 µg/kg/day) or a similar volume of PBS ($n = 6$). After 42 days mice were sacrificed by cervical dislocation, the left hind limbs were fixed.

Radiograph and µCT analysis

After the experimental period, the hind limbs of all mice with a tumor were analyzed by radiography (Kodak X-OMAT TL film, Eastman Kodak Company, Rochester, NY USA) using a Faxitron 43805 X-ray system (Hewlett-Packard, Sunnyvale, CA USA).

The radiographs were digitized and subsequently analyzed using Adobe Photoshop CS3 V10.0.1 (Adobe Systems, San Jose, CA USA).

After the experimental period, μ CT scans of the fixed hind limbs were made using a SkyScan 1076 μ CT scanner (SkyScan, Kontich, Belgium) using a source voltage and current set to 40 kV and 250 μ A, with a step size of 0.9° over a trajectory of 180° . Images were taken with an image pixel size of 9.03 μ m and a frame averaging of 3 to reduce noise. Reconstructions were made using nRecon V1.6.2.0 software (SkyScan) with a beam hardening correction set to 20% and a ring artifact correction set to 5. Processing, volume measurements and visualizations were performed using MeVisLab V1.6 (MeVis Medical Solutions AG, Bremen, Germany). All μ CT scans presented here were made using an identical scanning protocol and reconstructed with identical settings.

The method is very similar to the analysis of coronary arteries in CT angiography images using multi-plane reformatting. First, a center-line through the bone was defined. To do this, the user indicated manually the location of the center-line on several slices throughout the original 3D data set (hereafter referred to as the original space) after which a cubic B-spline was fitted through these points. Next, regular spaced planes perpendicular to the center-line were extracted. These planes were stacked into a new volume (hereafter referred to as the reformatted space). The user defined a VOI by indicating a start and an end plane relative to anatomical features in the reformatted space. These cut-off planes were transformed back into the original space after which a region grower, initiated at a single or multiple seed point(s) was used to select bone material. All connected voxels above a certain threshold value were considered as bone. For the scans presented here, a lower threshold of 50 and an upper threshold of 255 were used. Multiple seed points were needed in case there was fractured bone. This threshold value was determined using the best separation value from the intensity histogram and kept constant for all of the scans used within these experiments. The region grower was set to stop when no further connected voxels met the bone criterion or at the cut-off planes indicated by the user. This method can be used for μ CT datasets acquired using a different scanning protocol, scanner or reconstruction parameters. In which case, threshold values would be required to be optimized.

Results

All the reconstructed scans underwent a first visual assessment to check the quality of the data sets. None of the scans contained obvious scanning artifacts which would interfere with later analysis.

Center-line definition and generation of normalized cross-sections

The definition of a center-line is the pivotal first step of the analysis method. All further steps and volume measurements are performed relative to this center-line. The

center-line is calculated using several center points throughout the scan, indicated manually by the user.

A center-line was successfully fitted through each of the scans. This center-line was used to render cross-sections and longitudinal sections from the original space. The orientation of the section planes was relative to the center-line, even though the actual sections were generated from the original scan data (Figure 2.1). These normalized cross-sections and longitudinal sections can be generated anywhere along the center-line. Such normalized visualizations allow for side-by-side comparison between multiple scans or between scans and histological sections.

Using a reformatted space to define a normalized volume of interest

A reformatted space is used to define a VOI relative to the bone architecture in multiple scans, regardless of scan orientation or changes to the original bone anatomy. The reformatted space was generated by straightening the center-line and reformatting the rest of the scan around the new center-line accordingly. After selecting a normalized VOI in this reformatted space, the VOI was mapped back to the original scan space. This allowed the user to conduct measurements without distortion of the data due to the reformatting steps.

To generate the reformatted space, regular spaced planes perpendicular to the center-line were extracted from the original scan volume and stacked to form a new, normalized, volume. In this new volume, the naturally curved bone was straightened and orientated along the z-axis of the new stack regardless of its shape and position in the original volume. Longitudinal sections of this reformatted bone could be rendered and used for the assessment of the cortical thickness along the whole bone (Figure 2.2a–c). In contrast to visualizations based on the original scan data, the visualizations based on the reformatted data did not have artifacts resulting from the angle between the bone and the sectioning plane.

The new reformatted space allowed the user to navigate through the scans and locate positions relative to dominant anatomical features. For volume measurements, the VOI was defined by two cut-off planes perpendicular to the bone. Throughout these studies, the knee and the branch point between the tibia and fibula were used as dominant anatomical features relative to which these cut-off planes were defined. The cut-off planes were transformed back into the original space where the actual volume was determined using a region grower with a threshold set for calcified tissue (Figure 2.2d–e).

The center-line definition and generation of a reformatted space was tested on a scan of a more complex pathological case. This was also to evaluate the performance of the method in more extreme conditions. A scan of a fractured dislocated bone with a callus was used to generate a complex dataset. A reformatted space was generated and used to produce longitudinal cross-sections regardless of the fracture, dislocation and callus (Figure 2.3).

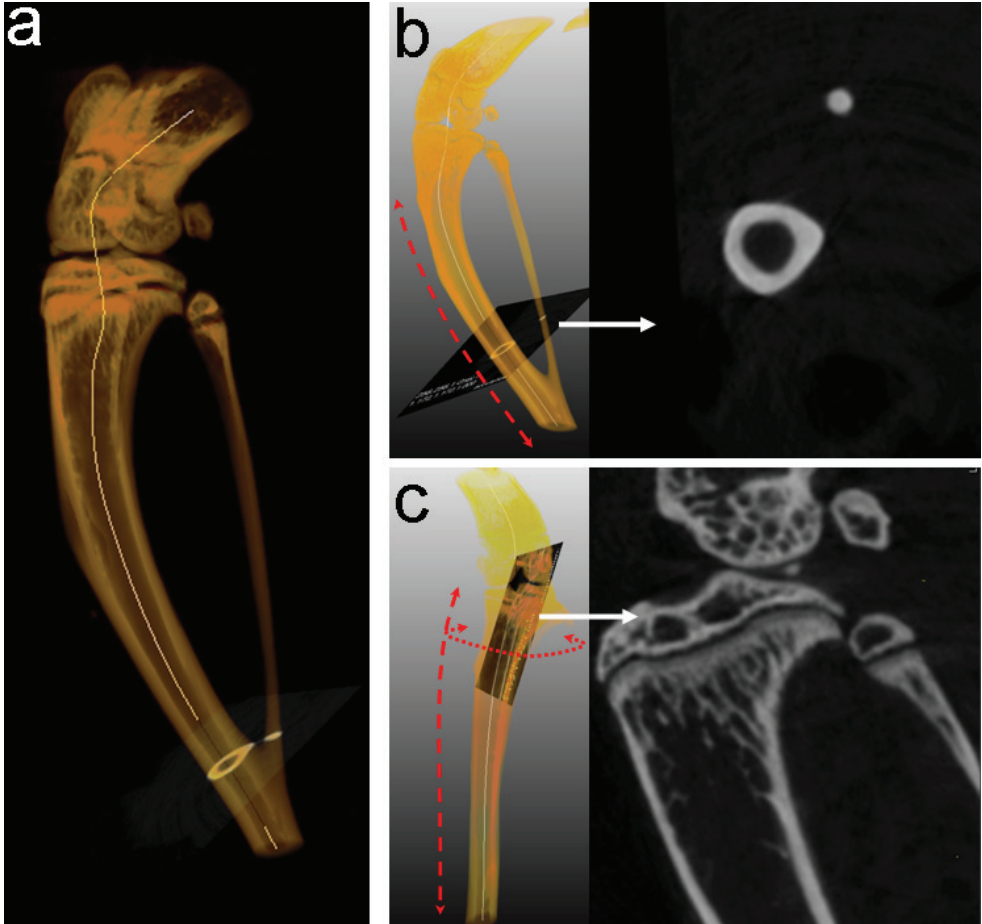


Figure 2.1: Fitting a spline and rendering cross-sections. (a) Semi transparent reconstruction of the original scan volume with a global threshold set for bone. Several center points were indicated manually and a spline has been fitted through these points. (b) Transversal cross-sections can be generated perpendicular to the center-line at any point along the center-line. Since the center-line follows the curvature of the bone, these cross-sections will always be perpendicular, i.e. in a 90° angle, to the bone. These cross-sections can be used for exact side-by-side comparison of the same section between different scans. (c) In a similar fashion, osculating planes can be generated anywhere along the center-line resulting in longitudinal cross-sections of the original scan volume. The spline tangent vector at the point of intersection with the longitudinal sectioning plane then forms the axis of rotation of the plane.

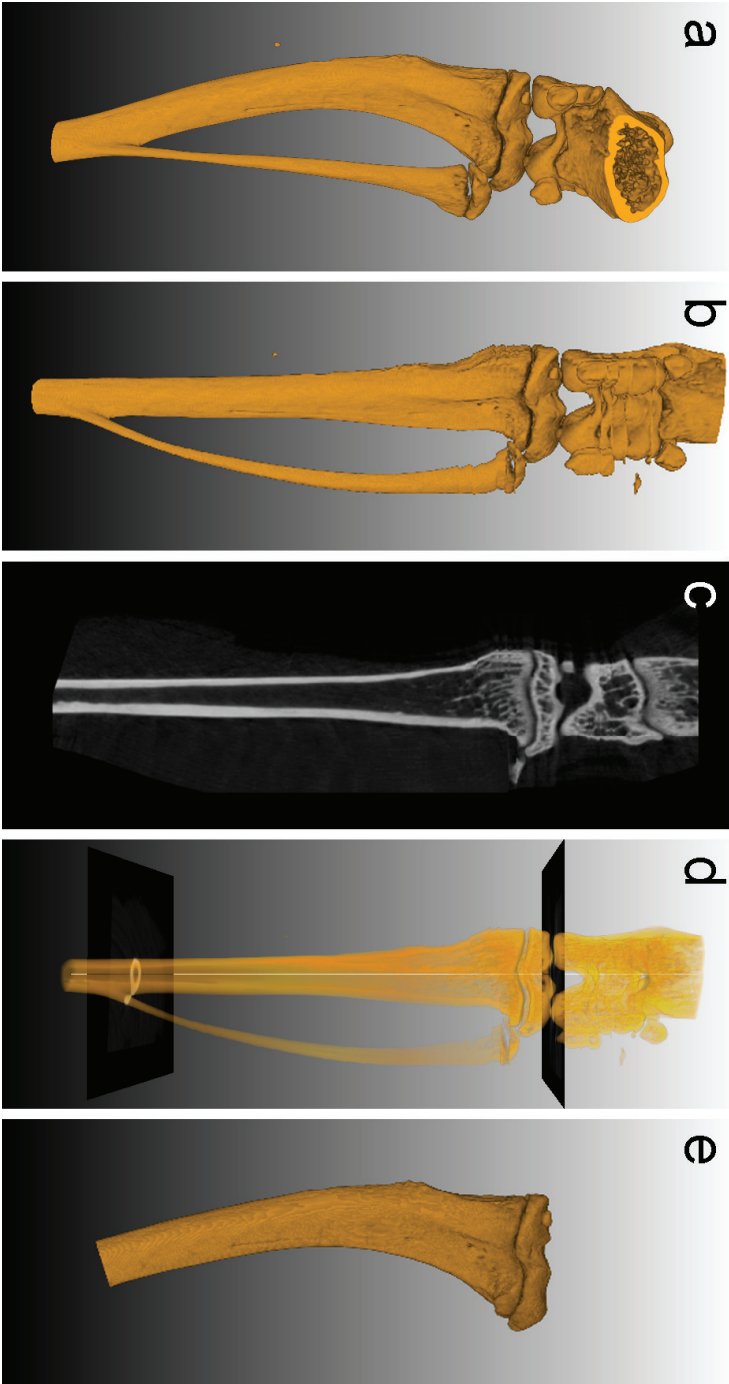


Figure 2.2: Selecting a VOI using orthogonal cross-sections. (a) 3D rendering of the original scan volume. (b) 3D rendering of the complete image stack of perpendicular cross-sections generated along the center-line (generated as shown in Figure 2.1). (c) Longitudinal cross-section generated from the reformatted space. The sectioning plane can be rotated along the longitudinal axis. These sections can be used for side-by-side comparison between different scans. (d) Definition of transversal cut-off planes using the reformatted space to calculate the relative position between the knee and the branch point of the fibula and tibia. (e) 3D rendering of a VOI. The volume was selected in the original space using a region grower limited by the cut-off planes which were mapped back from the reformatted space.

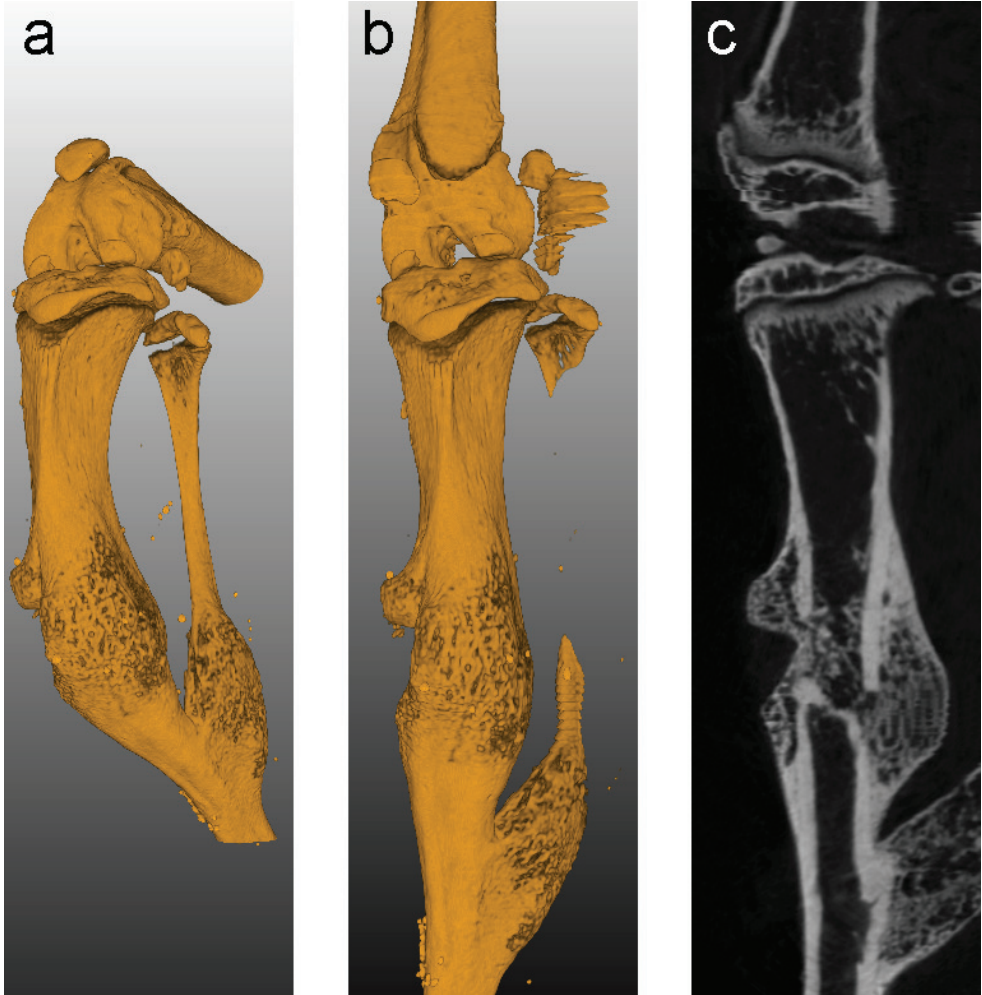


Figure 2.3: Generation of a reformatted space in a more severe pathological case. (a) Original scan volume. (b) Volume rendering of the reformatted space. (c) Longitudinal cross-section generated from the reformatted space. The reformatted space contains some artifacts due to the planar reformation. These artifacts have no influence on the measured bone volume since all actual measurements are performed within the original scan data.

Volume measurements using normalized volumes of interest

Next, the variability between observations was assessed to demonstrate that the VOI selection and volume measurement could be reproduced. In addition, we showed that the volume measurements could be used to quantify biologically relevant changes in bone volume.

To test the precision of the selection and quantification of a VOI, the center-line definition and volume measurements of mouse tibiae were repeated ten times on the same bone on ten different days performed by the same observer. The measured bone volume was the tibial volume between the knee and the branch point of the tibia and fibula, but not including the fibula (as shown in Figure 2.2e). The coefficient of variation (*cv*) of these ten repeated measurements, defined as the ratio of the standard deviation to the mean, was 0.001 indicating the low variation between observations.

To evaluate whether these volume measurements could be used to identify differences in bone volume, the tibial bone volumes of the left tibiae of risedronic acid treated mice were compared to that of untreated control mice of identical background, sex and age. The tibia was selected by placing two cut-off planes in the reformatting space, one through the knee and a second one at the branch point between the tibia and fibula. The fibula was not included in the VOI. Bone volume increased by approximately 22% (from $7.82\text{mm}^3 \pm 0.22$ to $9.58\text{mm}^3 \pm 0.58$) after treatment with risedronic acid. The longitudinal cross-sections indicate the increase in trabecular bone volume (Figure 2.4a).

Influence of intra-osseous inoculation on volume measurements

Intra-osseous inoculation of tumor cells is a method commonly used to study bone metastasis of cancer.⁹ During the intra-osseous procedure the bone marrow is partially flushed out of the bone. This partial bone marrow ablation has profound effects on the local bone turnover. One week after ablation, the bone formation induced from ablation of bone marrow reaches a maximum. After the first week, the bone volumes had normalized over time as the bone recovered from the procedure.^{10,11} We evaluated the effects of intra-osseous inoculation procedure on volume measurements of various VOIs to see how much it would interfere with the measurement of tumor-induced volumetric changes.

Four different VOI definitions were used to gain an insight in the location of volumetric changes; (1) the tibia from the branch point with the fibula up to the knee (referred to as whole bone), (2) the distal half of the whole bone volume (referred to as lower half), (3) the proximal half of the whole bone volume (referred to as upper half) and (4) the proximal 25% of the whole bone volume (referred to as the upper quarter).

The measurements were performed on a group of ten mice which received a sham operation with PBS on the right tibiae following the protocol of intra-osseous injection of cancer cells. The left tibiae were used as untreated controls. The mice were sacrificed at 10 and 42 days after the procedure. The volume increase was defined

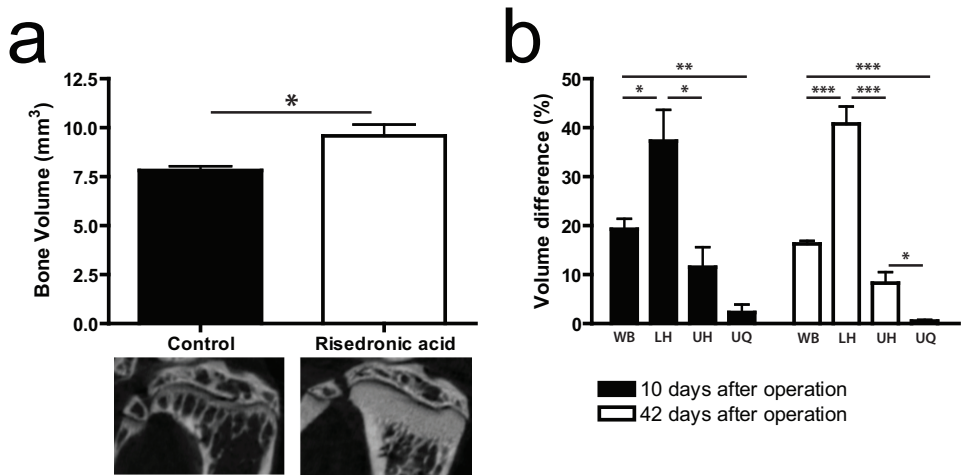


Figure 2.4: Quantification of various volumes of interest. (a) Tibial volumes of saline treated controls and risedronic acid treated animals after 42 days of treatment. The volumes of the tibiae increased with approximately 22%, from $7.82\text{mm}^3 \pm 0.22$ to $9.58\text{mm}^3 \pm 0.58$. The increase in trabecular bone volume can be appreciated from the detailed cross-sections of the epiphysis. Error bars indicate SEM, * : $p < 0.05$. (b) The effect of bone marrow ablation on healthy animals. The graph shows the relative difference in bone volume between bones after a partial bone marrow ablation (right hind limbs) compared to untreated control bones (left hind limbs) 10 days and 42 days after the surgical procedure. The whole bone (WB), lower half (LH) upper half (UH) and upper quarter (UQ) were measured in the same set of scans for comparison. The effect of bone marrow ablation was less toward the proximal end of the bone bath after 10 and 42 days. Error bars indicate SEM, * : $p < 0.05$, ** : $p < 0.01$, *** : $p < 0.001$.

as a difference in percentage compared to the whole bone volume. The whole bone volume increased approximately 19.5% (± 2.1) within the first ten days after bone marrow ablation. This relative volume increase was not the same for every region of the bone. In the lower half, the volume increase was approximately 37.2% (± 6.2) after 10 days, this was approximately 11.7% (± 4.1) in the upper half and approximately 2.1% (± 1.6) in the upper quarter. 42 days after partial bone marrow ablation, the whole bone volume was still increased by approximately 16.2% (± 0.5) and the lower half volume was increased by approximately 40.9% (± 3.4), the upper half volume by approximately 8.0% (± 2.2) and the upper quarter volume was completely normalized after 42 days (Figure 2.4b). Following intra-osseous injection of cancer cells, a tumor usually develops in the upper half of the bone.

Quantification of osteolysis induced volume changes

The relevance of volume measurements as a measure of cancer-induced osteolysis was tested. In addition, improvement of data quality was observed when a smaller pre-defined VOI around the area where osteolysis occurred was selected. This minimized

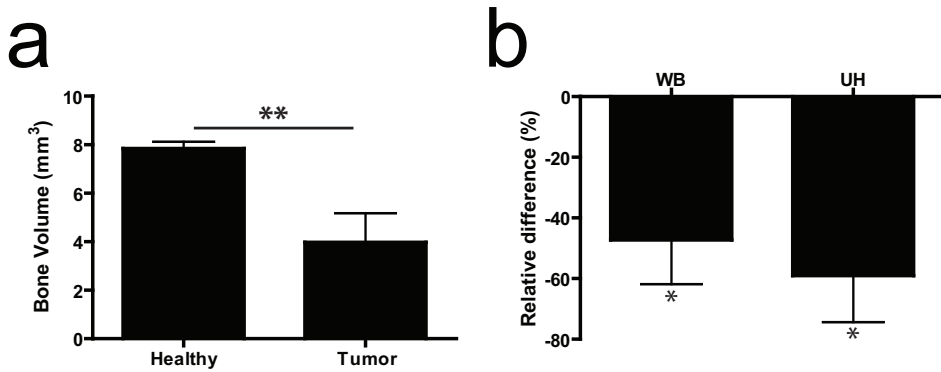


Figure 2.5: Quantification bone volume with and without osteolysis. (a) Bone volumes of the upper half of the tibia of healthy control limbs (left hind limbs) and tumor bearing limbs (right hind limbs) of the same animals, 42 days after tumor cell inoculations. Error bars indicate SEM, **: $p < 0.01$. (b) Relative changes in bone volume between bones of healthy control limbs (left hind limbs) and tumor bearing limbs (right hind limbs) of the same animals, 42 days after tumor cell inoculations. The whole bone (WB) and upper half (UH) were measured in the same scans for comparison. By measuring a smaller VOI, the relative difference bone volume between the groups is enlarged. Both the WB and UH measurements were significantly different from 0, but the p-value was smaller for the UH measurement (p-values of 0.031 and 0.018 for the WB and UH measurement respectively). Error bars indicate SEM, *: $p < 0.05$.

the influence of the inoculation induced changes on volume measurements as well. Mice received an intra-osseous inoculation of MDA-BO2 cells, an osteolytic breast cancer cell line. The mice were sacrificed after 42 days, this is comparable to other experiments performed using this specific MDA subclone.^{12–14} μ CT scans were made of both hind limbs, with and without a tumor.

The volumes of the upper half of the tibiae were used to quantify the loss of bone volume in the diseased limbs compared to the healthy limbs (Figure 2.5a). The choice for measuring the upper half of the tibiae was based on the differential effects of the intra-osseous inoculation method on bone volume as described in Figure 2.4b and the localization of tumor growth after the inoculation procedure. The bone volume of the upper half decreased significantly compared to the same volume in the healthy bone.

Volume measurements of the whole bone and the upper half were compared to evaluate whether the selection of a smaller VOI improved data quality. Whole bone and upper half volume measurements were performed on the same μ CT data sets to show the effect of selecting a smaller VOI and its impact on the decrease in bone volume. The osteolysis-induced bone loss was calculated as a percentage decrease in bone volume of the pathologic bone compared to the healthy bone. The volume of the whole osteolytic bones decreased by approximately 47% compared to the healthy control bones. This volume decrease was approximately 59% when measured in the

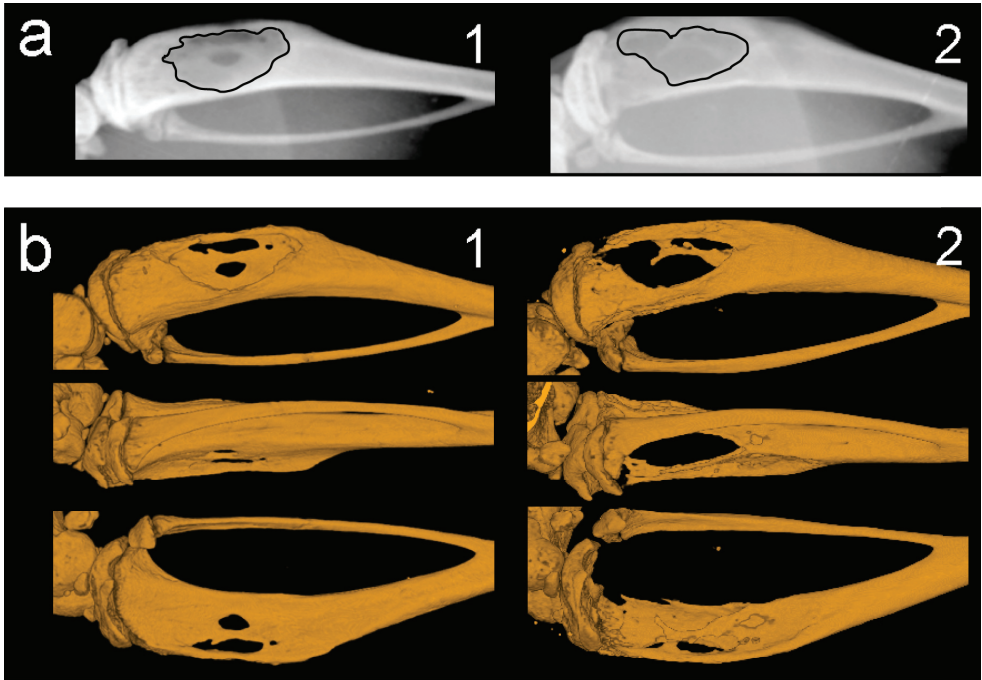


Figure 2.6: Radiography measurements are dependent on the projection. (a) Radiographs of two bones. The osteolytic lesion surface of bone #1 was 3420 pixels, the osteolytic lesion surface of bone #2 was 3402 pixels. (b) μ CT scans of the same two bones as in (a). It can be concluded from the μ CT scans by visual assessment that the osteolytic lesion in bone #1 is smaller than the osteolytic lesion in bone #2. Quantification of the upper half bone volume confirms this observation, the upper half volumes of bones #1 and #2 are 6.5mm^3 and 3.9mm^3 , respectively. This example is illustrative for how the flattening of a 3D structure can result in incorrect observations.

upper half of the tibiae. In both cases the standard error of the mean was 15 (Figure 2.5b). These results indicate that volume differences can be magnified by selection of a smaller VOI, thereby improving the sensitivity of volume measurements as a method to quantify osteolysis.

Finally, radiographs of the osteolytic bones were made to show how the flattening of a 3D structure can influence measurements of osteolysis. To illustrate this problem, two bones with a comparable osteolytic surface on radiographs were selected for μ CT analysis. The volumetric analysis of the μ CT scans of these bones revealed that the osteolytic lesion of one bone was more severe than the other (Figure 2.6). The radiographs were acquired on one film simultaneously and processed identically.

Discussion

A new method to select VOIs and quantify bone volumes in a normalized way is presented in this study. Drugs and diseases can induce major structural changes in bone. Traditional quantification methods often use the growth plate as primary landmark which is often destroyed in cases of severe osteolysis. The current method reduces the dependency on this structure by using the knee and the branch point of tibia and fibula, two structures which are very unlikely to disappear. Moreover, performing the VOI selection relative to a centerline makes it possible to compensate for large structural deformations such as fractures and dislocations. Since all bone segments are presented in a normalized way, the user can indicate identical start and end planes to define a VOI in different scans. In addition, the use of a center-line enables the user to generate normalized sections that can be used to compare between scans or to compare scans with histological sections. The actual measurement of the selected volume is performed in the original scan to prevent measurement errors due to compression and/or expansion and errors in surface voxel definition that occur during reformation of a scan.

Osteolysis is currently quantified using radiography analysis. However, μ CT scans are rarely used for quantification and instead they are used for visual representation as supportive data. One of the reasons for this is the lack of reliable methods for normalized processing of μ CT scans. However, volume measurements can provide a valuable addition, not only for the quantification of osteolytic lesions, but for osteoblastic lesions as well. 2D radiographs are able to show the shadow projection of a bone with a specific 3D structure. The projection and flattening of a 3D structure can result in lesions projected on top of each other or along the side of the bone. However, the problem is that measurement errors are inadvertently introduced as shown in Figure 2.6. Moreover, volume measurements are not prone to observer bias when using detailed predefined definitions of a VOI relative to the bone.

Volume measurements can be used to quantify changes in bone volume of both osteolytic and osteoblastic lesions. This in contrast to 2D modalities which cannot be used to quantify subtle increases in bone volume. However, interpretation of the data becomes more complex in cases where both osteolytic and osteoblastic processes occur in the same bone. For instance, procedures commonly used to inoculate bones with cancer cells can induce changes in bone volume (Figure 2.4). As a result, measurements of the entire tibial volume can be misleading. We showed that the increase in bone volume mainly occurs in the lower half of the tibia. Thus, the effects of bone marrow ablation on the volume measurements can be minimized by limiting the VOI to the upper half of the tibia, which is the actual area of the bone where a tumor grows. This is an example of how careful selection of a VOI is crucial to generate reliable data.

Recent advances have been made in using μ CT scans for the quantitative assessment of osteolysis. Johnson *et al.* followed bone loss over time in μ CT scans made at multiple time points. The authors elegantly showed that there is no effect

of repeated X-ray exposure on tumor growth following their μ CT scanning protocol. Using the entire bone volumes, they were able to visually detect osteolytic lesions one week after tumor cell inoculation and statistically differentiated lesions at week three more effectively than radiography.¹⁵ It is feasible that the results from their study could be further improved by selection of a smaller VOI. As we have shown from our own study, the work of Johnson *et al.* could have also benefited from use of a smaller VOI. This could have eliminated the disruption of the volume measurements by other processes such as the direct effect of intra-osseous inoculations.

The relative change in bone volume is increased when measuring a smaller VOI, this while the standard error of the mean remains the same (Figure 2.5). Optimization of the measured VOI increases the sensitivity of volume measurements for detecting differences between osteolytic or osteoblastic lesion sizes. Observer bias is still minimal as the VOI is pre defined as a volume relative to the anatomy of the bone.

Other methods used to analyze smaller VOIs in μ CT scans, which use a sub-volume instead of the entire bone volume, make use of a VOI with predefined dimensions. This VOI is ‘a box’ which is placed around a part of the scan. As a result, the selected VOI strongly depends on the scan orientation. Moreover, the curved shape of the tibia and possible fractures make it impossible to have two planes in a z-axis where both would cut the bone in a 90° angle. We eliminated these problems by using a VOI which is relative to the anatomy of the bone.

The reliable and reproducible selection of a VOI is pivotal when performing volume measurements in order to quantify the effects of osteolytic or osteoblastic effects. Here, we presented a curved planar reformation based approach to generate various normalized cross-sections. By using a reformatted space to select a VOI relative to the anatomy, we were able to eliminate measurement errors due to the orientation of the scan and deformations of the bone (e.g. dislocations, fractures). The effect of other processes elsewhere in the bone is eliminated by selecting a small VOI around the lesion. In conclusion, we found that by selecting a smaller VOI, the relative changes in bone volume are magnified which increases the sensitivity of our method of analysis as compared to other approaches.

Acknowledgments

This work has been supported by the Dutch Cancer Society Koningin Wilhelmina Fonds (grant UL2007-3801) (TS). The authors thank David Panzarella for the outstanding CG-support and Dr. Alan Chan for proofreading the manuscript.

References

1. Abrams HL, Spiro R, and Goldstein N. Metastases in carcinoma; analysis of 1000 autopsied cases. *Cancer*, 1950 Jan;3(1):74–85.
2. Clines GA and Guise TA. Hypercalcaemia of malignancy and basic research on mechanisms responsible for osteolytic and osteoblastic metastasis to bone. *Endocr Relat Cancer*, 2005 Sep;12(3):549–83.
3. Guise TA and Mundy GR. Cancer and bone. *Endocr Rev*, 1998 Feb;19(1):18–54.
4. Mundy GR. Metastasis to bone: causes, consequences and therapeutic opportunities. *Nat Rev Cancer*, 2002 Aug;2(8):584–93.
5. Nakai M, Mundy GR, Williams PJ, Boyce B, and Yoneda T. A synthetic antagonist to laminin inhibits the formation of osteolytic metastases by human melanoma cells in nude mice. *Cancer Res*, 1992 Oct;52(19):5395–9.
6. Sasaki A, Boyce BF, Story B, Wright KR, Chapman M, Boyce R, Mundy GR, and Yoneda T. Bisphosphonate risedronate reduces metastatic human breast cancer burden in bone in nude mice. *Cancer Res*, 1995 Aug;55(16):3551–7.
7. Peyruchaud O, Winding B, Pécheur I, Serre CM, Delmas P, and Clézardin P. Early detection of bone metastases in a murine model using fluorescent human breast cancer cells: application to the use of the bisphosphonate zoledronic acid in the treatment of osteolytic lesions. *J Bone Miner Res*, 2001 Nov;16(11):2027–34.
8. Wetterwald A, van der Pluijm G, Que I, Sijmons B, Buijs J, Karperien M, Löwik CWGM, Gautschi E, Thalmann GN, and Cecchini MG. Optical imaging of cancer metastasis to bone marrow: a mouse model of minimal residual disease. *Am J Pathol*, 2002 Mar;160(3):1143–53.
9. Arguello F, Baggs RB, and Frantz CN. A murine model of experimental metastasis to bone and bone marrow. *Cancer Res*, 1988 Dec;48(23):6876–81.
10. Patt HM and Maloney MA. Bone marrow regeneration after local injury: a review. *Exp Hematol*, 1975 Apr;3(2):135–48.
11. Bab I, Gazit D, Muhlrad A, and Shteyer A. Regenerating bone marrow produces a potent growth-promoting activity to osteogenic cells. *Endocrinology*, 1988 Jul;123(1):345–52.
12. Boucharaba A, Serre CM, Grès S, Saulnier-Blache JS, Bordet JC, Guglielmi J, Clézardin P, and Peyruchaud O. Platelet-derived lysophosphatidic acid supports the progression of osteolytic bone metastases in breast cancer. *J Clin Invest*, 2004 Dec;114(12):1714–25.
13. van der Pluijm G, Que I, Sijmons B, Buijs JT, Löwik CWGM, Wetterwald A, Thalmann GN, Papapoulos SE, and Cecchini MG. Interference with the microenvironmental support impairs the de novo formation of bone metastases in vivo. *Cancer Res*, 2005 Sep;65(17):7682–90.

14. Buijs JT, Que I, Löwik CWGM, Papapoulos SE, and van der Pluijm G. Inhibition of bone resorption and growth of breast cancer in the bone microenvironment. *Bone*, 2009 Feb;44(2):380–6.
15. Johnson LC, Johnson RW, Munoz SA, Mundy GR, Peterson TE, and Sterling JA. Longitudinal live animal micro-ct allows for quantitative analysis of tumor-induced bone destruction. *Bone*, 2011 Jan;48(1):141–51.

3

Automated Bone Volume and Thickness Measurements in Small Animal Whole-Body μ CT Data

Martin Baiker ¹ & Thomas J.A. Snoeks ²
Eric L. Kaijzel ²
Ivo Que ²
Jouke Dijkstra ¹
Boudewijn P.F. Lelieveldt ^{1 3}
Clemens W.G.M. Löwik ²

Mol Imaging Biol. 2011 Oct 13. Epub ahead of print

¹Dept. of Radiology, Division of Image Processing LKEB, LUMC, Leiden, The Netherlands

²Dept. of Endocrinology, LUMC, Leiden, The Netherlands

³ICT Group, Dept. of Mediamatics, Delft University of Technology, Delft, The Netherlands

Abstract

Purpose Quantification of osteolysis is crucial for monitoring treatment effects in preclinical research and should be based on μ CT data rather than conventional two dimensional radiographs to obtain optimal accuracy. However, data assessment is greatly complicated in the case of three dimensional data. This paper presents an automated method to follow osteolytic lesions quantitatively and visually over time in whole-body μ CT data of mice.

Procedures This novel approach is based on a previously published approach to coarsely locate user-defined structures of interest in the data and present them in a standardized manner (Baiker *et al.*, *Med Image Anal* 14:723–737, 2010; Kok *et al.*, *IEEE Trans Vis Comput Graph* 16:1396–1404, 2010). Here, we extend this framework by presenting a highly accurate way to automatically measure the volumes of individual bones and demonstrate the technique by following the effect of osteolysis in the tibia of a mouse over time. Besides presenting quantitative results, we also give a visualization of the measured volume to be able to investigate the performance of the method qualitatively. In addition, we describe an approach to measure and visualize cortical bone thickness, which allows assessing local effects of osteolysis and bone remodeling. The presented techniques are fully automated and therefore allow obtaining objective results, which are independent of human observer performance variations. In addition, the time typically required to analyze whole-body data is greatly reduced.

Results Evaluation of the approaches was performed using μ CT follow-up datasets of 15 mice ($n = 15$), with induced bone metastases in the right tibia. All animals were scanned three times: at baseline, after 3 and 7 weeks. For each dataset, our method was used to locate the tibia and measure the bone volume. To assess the performance of the automated method, bone volume measurements were also done by two human experts. A quantitative comparison of the results of the automated method with the human observers showed that there is a high correlation between the observers ($r = 0.9996$), between the first observer and the presented method ($r = 0.9939$), and also between the second observer and the presented method ($r = 0.9937$). In addition, Bland-Altman plots revealed excellent agreement between the observers and the automated method (inter-observer bone volume variability, $0.59 \pm 0.64\%$; Obs1 vs. Auto, $0.26 \pm 2.53\%$ and Obs2 vs. Auto, $-0.33 \pm 2.61\%$). Statistical analysis yielded no significant difference ($p = 0.10$) between the manual and the automated bone measurements and thus the method yields optimum results. This could also be confirmed visually, based on the graphical representations of the bone volumes. The performance of the bone thickness measurements was assessed qualitatively.

Conclusions We come to the conclusion that the presented method allows to measure and visualize local bone volume and thickness in longitudinal data in an accurate and robust manner, proving that the automated tool is a fast and user friendly alternative to manual analysis.

Introduction

Breast cancer metastasizes preferentially to bone. *Post mortem* evaluation revealed that 70% of patients who died of breast cancer had bone metastases present in the skeleton.¹ Bone metastases cause severe morbidity in living patients such as bone pain, fracture, hypercalcemia, and nerve compression.^{2,3} As a result, quantification of osteolytic lesion size is pivotal in preclinical research of metastatic bone disease and treatment evaluation in small animal models. Osteolysis is currently quantified using two dimensional (2D) radiographs.^{4,5} The scoring of these radiographs is performed manually by drawing a region of interest (ROI) around the lesion and measuring the bone area. The problem with this procedure is that lesions may be projected on top of each other and will therefore be underestimated when quantified, due to the flattening of the three dimensional (3D) structure.⁶ The same may happen for lesions on the side of bone. Furthermore, performing the analysis manually is prone to observer bias. μ CT datasets provide spatial information, suitable for measurements of various bone parameters such as bone volume, bone thickness, and bone mineral density. These measurements are potentially more informative than the radiographic analyses. Also, μ CT enables the researcher to study the overall bone structure.

The use of μ CT for quantitative measurements is not without difficulties. The shape and position of a volume of interest (VOI, the 3D counterpart of a ROI in 2D) in a 3D dataset greatly influence the measurement results. Therefore, it is crucial that the selection of a VOI is reproducible and not affected by the scan orientation or the observer who performs the procedure. We previously published a manual approach for the normalized selection of a region of interest in complex shapes (Chapter 2).⁶ This manual approach provides good and reproducible results but is very time-consuming and requires well trained observers.

The comparison of whole-body datasets from longitudinal studies is even more difficult. Variation in posture of the animal during scans taken at different scan dates makes it nearly impossible to spot subtle disease induced differences between scans.⁷

We previously published an approach to automatically align the skeletons of animals that were scanned at different points in time. The method can handle large postural differences between animals and as a result, specifically designed holders that are sometimes used to coarsely align animals⁸ are not required. In addition, the user can select individual bones and generate side-by-side visualizations of these bones from multiple longitudinal datasets (Figure 3.1). Such normalized visualizations greatly facilitate detailed qualitative assessment of structures in multiple complex and large datasets.⁹

Here we describe an addition to this method, which enables the user to perform automated quantitative measurements of bone volume and thickness alongside the visual output. For evaluation, we applied the method to segment the femur and the tibia / fibula in whole-body follow-up μ CT datasets and measured the bone volume and cortical thickness at three points in time: baseline, 3 and 7 weeks. To test whether this approach could be used to quantify biologically relevant changes in bone

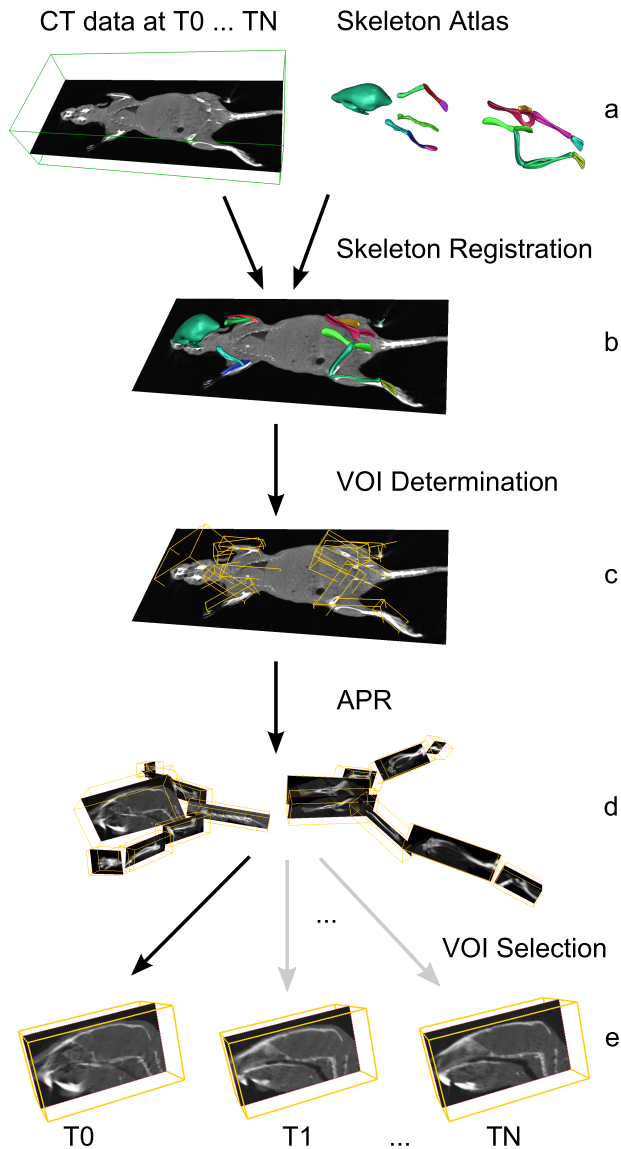


Figure 3.1: An overview of our previously published approach to coarsely locate user-defined structures of interest in follow-up whole-body data⁷ and present them in a standardized manner.⁹ (a) The skeleton of an atlas is registered (*aligned*) to μ CT data acquired at N time points $T_0 \dots T_N$. (b) An example of the registration result for one dataset. (c) Based on the registration result, we can determine volumes of interest (VOIs) around individual bones. The VOIs are shown as yellow boxes. (d) Based on the VOIs, the data can be put in a standardized layout using Articulated Planar Reformation (APR).⁹ (e) The advantage of the standardized layout is, is that the same structures in datasets from different time points ($T_0 \dots T_N$) can be visualized side-by-side, greatly facilitating data comparison.

volume, breast cancer cells were injected into the right tibia after the baseline scan. The left tibia remained untreated and served as a reference. The results of the automated measurements are compared with manual measurements of two experts. We show that the automated segmentation and volume measurements perform equally accurate and reproducible as manual segmentation and volume measurements.

In summary, the goals of this work are to:

- Automate the task of measuring the volume of a user-defined bone in whole-body *in vivo* μ CT data and demonstrate the method by measuring the bone volume of the proximal tibia / fibula at several points in time
- Compare the automated measurements with two human observers and show that the results are not significantly different
- Present a way to assess the measurement quality visually, by providing proper visualization
- Present a method to assess effects of osteolysis and bone remodeling locally (site-specific bone loss or gain) by automatically measuring and visualizing cortical bone thickness

Materials & methods

Animals

Fifteen ($n = 15$) female nude mice (BALB/c nu/nu, 6 weeks old) were acquired from Charles River (Charles River, L'Arbresle, France), housed in individually ventilated cages, food and water were provided *ad libitum*. Surgical procedures and μ CT imaging were performed under injection anesthesia (100mg/kg ketamine + 12.5mg/kg xylazine). Animals were sacrificed by cervical dislocation at the end of the experimental period. Animal experiments were approved by the local committee for animal health, ethics and research of Leiden University Medical Center.

Cell lines & culture conditions

The cell line MDA-231-B/Luc+ (hereafter MDA-BO2), a bone-seeking and luciferase-expressing subclone from the human breast cancer MDA-MB-231,^{10,11} was cultured in DMEM (Invitrogen, Carlsbad, CA, USA) containing 4.5g glucose/l supplemented with 10% fetal calf serum (FCS) (Lonza, Basel, Switzerland), 100 units/ml penicillin, 50 μ g/ml streptomycin (Invitrogen), and 800 μ g/ml geneticin/G418 (Invitrogen). The cells were monthly checked for mycoplasma infection by PCR. The cells were donated by G. van der Pluijm (Leiden University Medical Center, Leiden, The Netherlands).

Experimental setup

MDA-BO2 cells were injected into the right tibiae as described previously.¹¹ In brief, two holes were drilled through the bone cortex of the right tibia with a 25-gauge needle (25G 5/8, BD MicroFine, Becton Dickinson, Franklin Lakes, NJ, USA) and bone marrow was flushed out. Subsequently, 250,000 MDA-BO2 cells per 10 μl PBS were injected into the right tibiae of the animals. μCT scans were made before the tumor cell inoculation (T0) in supine position, 3 weeks after tumor cell inoculation (T1) in prone position, and 7 weeks after tumor cell inoculation (T2) in supine position. The animals were scanned with arbitrary limb position.

μCT data acquisition

μCT scans were made using a SkyScan 1076 μCT scanner (SkyScan, Kontich, Belgium) using a source voltage and current set to 50kV and 200 μA , respectively, with an X-ray source rotation step size of 1.5° over a trajectory of 180°. Reconstructions were made using the nRecon V1.6.2.0 software (SkyScan) with a beam hardening correction set to 10%, a ring artifact correction set to 10, and the dynamic range set to $-1,000 - 4,000$ Hounsfield units. The datasets were reconstructed with voxel size $36.5 \times 36.5 \times 36.5 \mu\text{m}^3$. Neither cardiac nor respiratory gating was used.

Manual segmentation of the tibia / fibula

To assess the performance of the automated tibia volume measurements, two field experts were asked to segment the proximal part of the right tibia. To be able to use the data at full resolution, this was not based on the whole-body dataset but on a sub-volume, corresponding to the right tibia, which was automatically determined following the procedure in Figure 3.1. An example of such a sub-volume is shown in Figure 3.2. Starting with this sub-volume, the experts were asked to segment the proximal part of the tibia / fibula, i.e., the part between the knee and the location where tibia and fibula separate. The manual segmentation was performed using a tool that was developed in-house with MeVisLab V1.6 (MeVis Medical Solutions AG, Bremen, Germany) as described in Chapter 2.⁶

After segmentation, the number of bone voxels was determined using a threshold value to separate bone from background. To determine the optimum threshold for the *in vivo* datasets, the tibia of one of the animals was scanned *ex vivo* with high resolution ($9.125 \times 9.125 \times 9.125 \mu\text{m}^3$) after the follow-up experiment. Subsequently, the tibial bone volume was measured. To find the optimum threshold, for segmentation of bone from the background in the low-resolution data, the threshold was set such that the volume of the tibia of the same mouse in the low resolution data was the same as the volume of the tibia in the high resolution data. This threshold was kept constant for segmentation of all datasets. The result was a volume dataset with the same size as the initial sub-volume with voxels labeled as relevant bone, i.e., the proximal tibia / fibula, and background (including irrelevant bone).

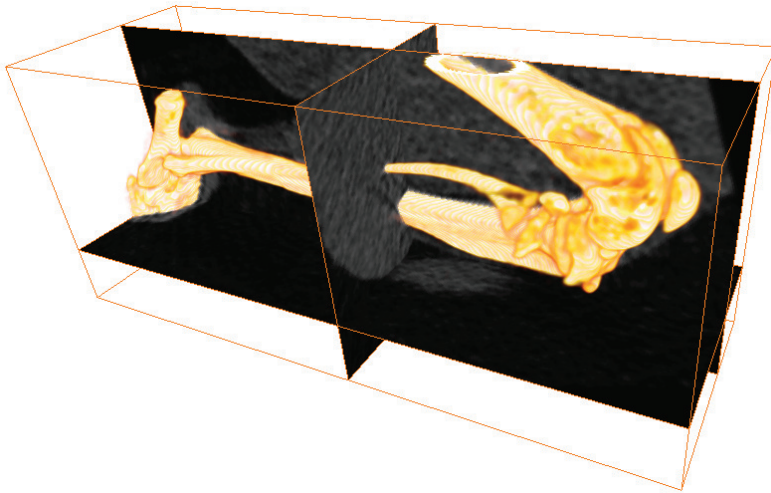


Figure 3.2: Example of an automatically determined sub-volume, including the right tibia. The bone surface is shown together with the corresponding sub-volume.

Therefore, the bone volume of the proximal tibia / fibula could be determined by multiplying the total amount of bone voxels with the voxel volume, i.e., in our case *amount of voxels* $\times (36.5 \times 36.5 \times 36.5)\mu\text{m}^3$. To be able to assess the quality of the segmentation visually, we provided a surface representation of the manually segmented sub-volume. The tibia / fibula bone volume served as the reference for the automated method presented in the next subchapter.

Automated segmentation of the tibia / fibula

An automated method should yield results that are as similar as possible to the results a human observer would obtain. Therefore, it should be designed such that it mimics the manual procedure as much as possible. Just as for the manual segmentation, presented in the previous subchapter, the automated segmentation was based on a sub-volume as shown in Figure 3.2 and the goal was to segment the proximal part of the tibia / fibula. First, a center-line was determined that runs through the center of the femur, the knee and the center of the tibia, based on the registration of the skeleton atlas to the μCT data. To this end, we defined 21 bone center locations (10 in the femur, 11 in the tibia) in the atlas. Subsequently, if the atlas bones are registered to the data (Figure 3.1b), these atlas bone center locations are approximately in the bone centers of the femur and the tibia in the μCT data (the bone center locations do only have to be defined once for the atlas). Subsequently, a bone center-line was derived using cubic B-spline fitting through the bone centers. Next, the volume was segmented into bone and background using global thresholding with

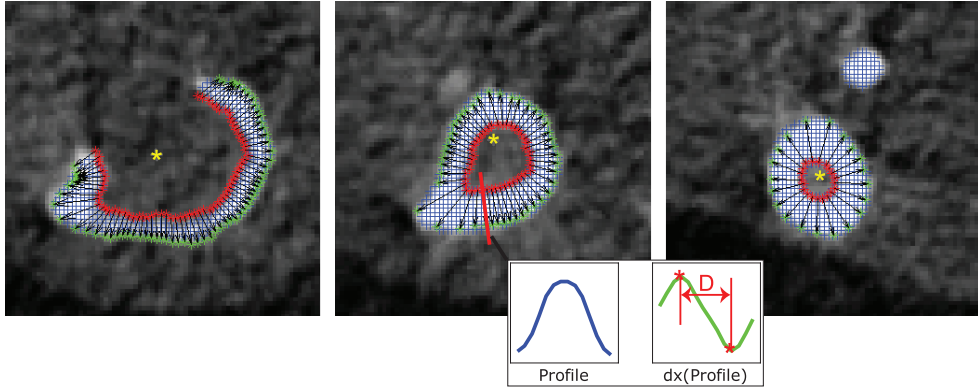


Figure 3.3: Demonstration of how the bone thickness D is determined automatically if osteolytic lesions are present. The slices from the μ CT sub-volume that are orthogonal to the center-line, with an overlay of the voxels labeled “bone” (blue net), are shown. Along the bone center-line (orange stars), grey-value profiles are taken in axial direction at evenly spaced locations along the center-line. The location close to the knee (left) and the locations halfway between the knee and the tibia / fibula separation (middle) and close to the tibia / fibula separation (right) are shown. Points on the inner boundaries are indicated by red stars, corresponding points on the outer boundaries by green stars. The black arrows indicate the directions, along which the grey value profiles for the bone thickness measurement are derived. An example of a profile path is shown in red (middle). The inset shows an example of a grey-value profile in blue and its gradient values in green (dx symbolizes a mathematical derivation). The bone boundaries can be found where the gradients are maximum (red stars in the inset) and the bone thickness D is the distance between the boundaries.

the same threshold as was used for the manual segmentation (see previous subsection). Following the bone center-line from the knee towards the distal part of the tibia, the separation of the tibia and the fibula was determined using a hierarchical clustering technique with single linkage¹² that determined the number of bone clusters at regular spaced locations along the center-line. The Euclidean distance between points was chosen as the dissimilarity measure. The transition from two clusters (tibia and fibula) to one cluster identified the location of bone separation. Figure 3.3 (right) shows a slice, perpendicular to the center-line, which is close to this point (tibia = large spot, fibula = small spot).

Separation of the tibia / fibula from the femur was done in a slightly different way as compared with the manual procedure because it is very difficult to automatically determine a flat separation plane within the knee. Therefore, we chose to rely on a classifier that automatically separates all voxels labeled as “bone” (i.e., after thresholding) into the two classes “femur” and “tibia / fibula”. The classifier was trained using volumetric (tetrahedral) meshes of the femur and tibia atlas after registration (Figure 3.1b). Each node location of the meshes was weighted with a 3D Gaussian probability density function with width h (Parzen kernel density estimation¹²). Subsequently, all individual probability densities were summed up, yielding a bone-dependent posterior probability density value within the entire data volume.

A voxel labeled as “bone” can thus be identified as “femur” or “tibia / fibula”, depending on its location in the volume, depending on which of the two classes has the highest posterior probability at that location. The parameter h was optimized using a leave-one-out test, based on the available datasets. Finally, the bone volume of the proximal tibia / fibula could be derived by counting the bone voxels classified as “tibia / fibula” along the center-line, up to the tibia / fibula separation determined before and multiplying the total amount of bone voxels with the voxel volume. To assess the quality of the automated segmentation visually, we provided a surface representation of the result.

Automated segmentation of the femur

As a proof of concept that the automated segmentation method can be applied to other skeletal elements besides the tibia as well, we demonstrate an automated segmentation of the femur. The femur is connected proximally to the pelvis and distally to the tibia. Following the procedure given in the “Automated Segmentation of the tibia / fibula” section, the tibia was separated from the femur in a first step. Second, volumetric meshes of the atlas femur and the atlas pelvis after skeleton registration were used to derive a 3D posterior probability density function for these bones and to determine the separation of pelvis and femur, following the same procedure as described in the “Automated Segmentation of the tibia / fibula” section. The kernel width h was identical to the one used for the separation of the tibia and the femur. To assess the reproducibility of the volume measurements, the volume of the left femur of three animals was measured at all points in time and compared with the volume of the right femur over time. In addition, the bones were segmented manually to assess measurement accuracy. To ensure that the influence of the induced cancer cells had a minimal effect on the femur bone volume, we chose three animals where osteolysis had only slightly progressed over time.

Automated bone thickness measurements and visualization

Accurate knowledge of local bone thickness enables to follow the progress of osteolysis and bone remodeling over time. Therefore, a method is required to measure bone thickness in 3D and to relate the measurement to the exact location on the bone. Above that, the method should be able to handle severe structural changes over time, induced by osteolysis.

There are mainly two approaches described in the literature to assess bone thickness in volumetric data: volume-based methods and surface (feature)-based methods.¹³ These are focusing mainly on measuring trabecular bone and the approaches generally take the entire image domain into account. The advantage is that structures with very different shape can be analyzed. Although the approaches could be used for measuring cortical bone as well, the tube-like shape of long-bones enables another approach. Since the registration of the skeleton atlas to the data yields a

coarse segmentation of the skeleton, we can map a bone center-line, defined in the atlas femur and tibia, to the femur and tibia in the data. Subsequently, we can employ a technique similar to that presented in Van der Geest *et al.*,¹⁴ where the authors measure the diameter and wall thickness of blood vessels in magnetic resonance angiography and computed tomography angiography, based on slices that are orthogonal to the vessel center-line. The great advantage of relying on a center-line is that it is possible to determine exactly at which locations along the center-line the thickness should be measured. The main difference between analyzing vessels and potentially osteolytic bone is that vessels are continuous structures while bone can be highly fractured and contain holes.

The methods for trabecular thickness measurement generally take the entire image domain into account, which can be very time-consuming especially for large volumes or surfaces with a great amount of vertices. The proposed approach enables to greatly reduce computational burden. Above that, being able to define the thickness measurement based on a center-line allows to sample certain areas more densely than others, yielding more accurate measurements.

To determine the cortical bone thickness of the tibia automatically, we relied on the bone center-line presented in the previous section and the sub-volume according to Figure 3.2. At regularly spaced locations, following the center-line in distal direction, grey-value profiles were extracted in axial direction, starting from the center-line and progressing outwards. In total, 360 profiles were taken per location, with 1° angle difference between them, thus covering an entire circle, oriented orthogonal to the center-line. Since the center-line lies in an area with low intensity (bone marrow), the grey-value profile will consist of low values at the beginning, high values, when the bone is crossed and again low values outside the bone (muscle tissue). An example of such a profile is given in Figure 3.3 (middle). Subsequently, the inner boundary of the bone can be determined, using the highest positive gradient of the profile. Doing this for all 360 profiles yielded 360 points that are located at the inner boundary of the bone. However, since the center-line may not always lie exactly in the center these points are usually not evenly distributed along the boundary. Therefore, we applied an additional resampling step so that the points had a minimum distance of one voxel. Examples of resulting inner boundaries are shown in Figure 3.3 (red stars). Next, again grey-value profiles were taken, but this time orthogonal to the inner boundary of the bone, starting inside the bone and progressing outwards. An example path of such a profile is shown as a red line in Figure 3.3 (middle). Finally, the bone thickness D could be determined using the highest positive and the highest negative gradient of the profile, demarcating the inner and the outer boundary of the bone. This is demonstrated in the inset in Figure 3.3 (middle). Hence, our definition of bone thickness is the distance from the inner boundary to the outer boundary of the cortex, orthogonal to the inner boundary.

The bone thickness measurements can be uniquely related to the location on the bone, where they were derived. To be able to assess the bone thickness locally and still have the anatomical context information available, we present a visualization

that is based on a surface representation of all bone in the sub-volume (Figure 3.2). To each location on the bone surface, we linked the corresponding bone thickness and assigned a value-dependent color. The result is a surface representation of the bone, on which the color indicates the bone thickness.

The automated segmentations and bone thickness measurements and visualizations were performed using Matlab 2010b (The Mathworks, Natick, USA).

Quantitative analysis of measurement results

To assess how similar the results of the automated method and the human experts are, Bland-Altman¹⁵ plots as well as Pearson's correlation coefficients are presented. To investigate in detail the influence of the time point (i.e., baseline, first, and second follow-up), the bone (i.e., healthy and pathologic), and the observer (i.e., automated, observer 1, and observer 2) on the bone volume measurement, we performed a statistical analysis using a three-way repeated measures analysis of variance (ANOVA),¹⁶ with the bone volume as the dependent variable and observers, bone (i.e., healthy and pathologic), and time point as the independent variables ($3 \times 2 \times 3$ levels). A repeated measure design requires the variances of the differences between levels to be equal. Therefore, Mauchly's sphericity test should be non-significant if we are to assume that the condition of sphericity has been met. If the results of the test indicated that the assumption of sphericity was violated, the degrees of freedom were corrected using Greenhouse-Geisser estimates of sphericity.¹⁶ To identify significant differences between group means for main and interaction effects, a Tukey honest significant difference (HSD) post hoc test was used. Effects were considered to be significant if $p < 0.05$. The statistical analysis was performed using Statistica 8.0 (StatSoft, Tulsa, USA).

Results

To be able to assess the accuracy of a manual and an automated segmentation of the proximal tibia / fibula, surface visualizations are generated after the measurements. Examples are shown in Figure 3.4.

The results of the correlation tests are shown in the top row of Figure 3.5 and the measurement agreements are presented in the bottom row of Figure 3.5. To assess possible influence of the time point on the agreement, the data are shown for each time point individually (see legends).

Mauchly's test indicated a violation of the sphericity assumption and therefore degrees of freedom were corrected using Greenhouse-Geisser estimates of sphericity (see Table 3.1). The results show that there are significant differences in measured bone volume for the main effect Time, $F(1.39, 16.73) = 28.80$ ($p < 0.001$), as well as the interaction effects Method \times Time, $F(1.63, 19.59) = 16.71$, ($p < 0.001$), and Bone \times Time, $F(1.08, 12.93) = 12.75$ ($p < 0.05$). The Tukey HSD post hoc tests revealed a significant difference in bone volume between T0 and T1 ($p < 0.001$) as

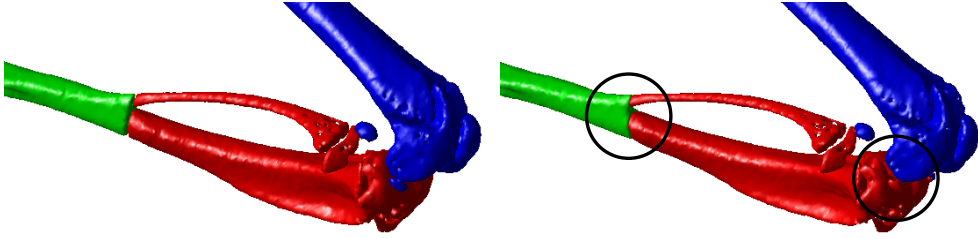


Figure 3.4: Manual and automated segmentation. Bone surface visualization after manual segmentation of the proximal tibia / fibula (left). Bone surface visualization after automated segmentation of the proximal tibia / fibula (right; blue femur, red proximal tibia / fibula, green distal tibia / fibula). The circles highlight differences between the segmentations.

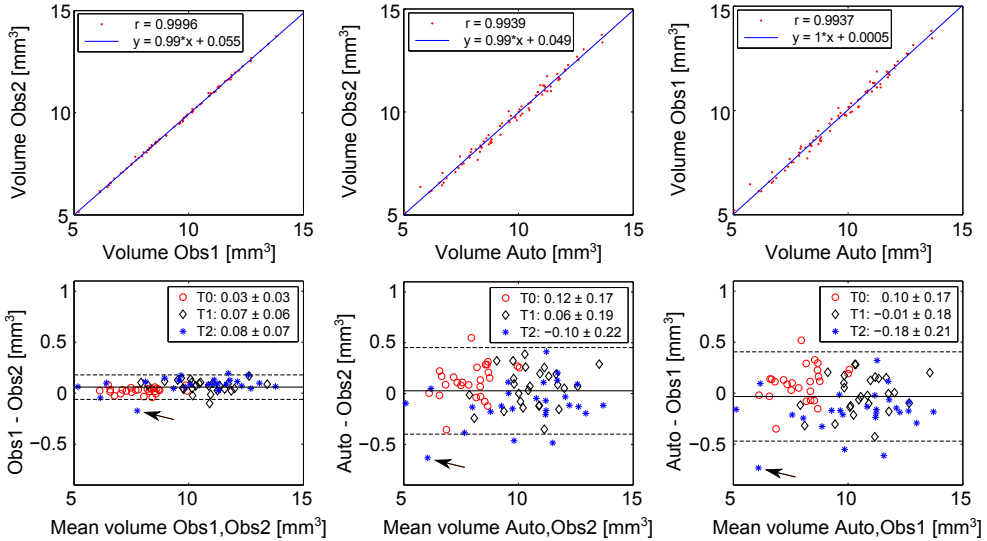


Figure 3.5: Correlation and agreement between human observers and the automated method.

Correlation between the measurements (in mm^3) of the two human observers and the automated method (top row). Obs1 vs. Obs2, Auto vs. Obs1 are shown. The blue line represents a linear best fit, defined by the function in the legend. The Pearson correlation r , based on the data (red), is also shown in the legend. Bland-Altman plots representing the measurement agreement between the two human observers and the automated method (bottom row). The black lines indicate the grand means (line) ± 1.96 times the standard deviation (broken line), which are 0.06 ± 0.12 , 0.03 ± 0.43 and $-0.03 \pm 0.44 \text{mm}^3$, respectively. The arrows indicate the measurement with maximum disagreement between the observers. To assess, if the agreement is dependent on the time point when the data was acquired, these are shown in different colors (red circles baseline or T0, black diamonds T1, blue stars T2). Note that the values in the legends are the means ± 1 times the standard deviation.

well as T0 and T2 ($p < 0.001$). There was no significant difference between T1 and T2 ($p > 0.05$).

For the Bone \times Time interaction effect (Figure 3.6, top left), relevant significant effects were present for healthy vs. pathologic bone at T2 ($p < 0.001$), but not at T0 and T1 (both $p > 0.05$). For the Method \times Time interaction effect (Figure 3.6, top right), relevant significant effects were present for Obs1 vs. Auto and Obs2 vs. Auto at T0 ($p < 0.05$ and $p < 0.001$) but not for Obs1 vs. Obs2 at T0 ($p > 0.05$). Furthermore there were significant effects for Obs1 vs. Auto and Obs2 vs. Auto at T2 ($p < 0.001$ and $p < 0.05$) but not for Obs1 vs. Obs2 at T2 ($p > 0.05$). There were no significant effects at T1.

The results of the comparison of the difference in bone volume between healthy and pathologic bone for six different mice are given in Figure 3.6 (middle and bottom rows).

The results of the femur segmentation and subsequent volume measurements are shown in Figure 3.7. The average volume of the right and the left femur was $0.89 \pm 0.64\%$ when measured manually and $0.83 \pm 0.53\%$ when measured automatically. To see if there is a significant difference between the human observer and the automated method, a similar statistical analysis as presented in the “Quantitative Analysis of Measurement Results” section was performed, this time including one human observer instead of two. Mauchly’s test indicated no violation of the sphericity assumption ($p > 0.05$). The results show that the main effect method is significant $F(1, 2) = 92.894$, $p < 0.05$, and the mean difference between the automated and the manual method is $2.15 \pm 0.75\%$. This means that the automated method results in lower measured volumes than the manual method.

A comparison of the development of the bone thickness over time for a healthy and a pathologic bone are given in Figure 4.4 by means of bone surface visualizations, where color indicates the bone thickness.

Discussion

In this article, we described a fully automated approach to analyze skeletal changes in rodent whole-body μ CT scans. The automated approach is capable to (1) align scans of the same animal, taken at different time points; (2) automatically segment a sub-volume (VOI) in these scans; (3) measure the bone volume; (4) measure cortical thickness; and (5) visualize it by means of assigning thickness-dependent colors. In addition, the user can visually check the segmentation performance using 3D bone surface representations and can generate normalized sections of identical sectioning planes in longitudinal scans for side-by-side comparison.

Conventional analysis of radiographs involves identifying osteolytic lesions manually. The procedure of manually drawing a region of interest is prone to observer bias and small changes in thickness or multiple lesions projected on top of each other are easily overlooked.⁶ Manual analysis of μ CT data is a better alternative, but is very labor intensive (Chapter 2).⁶

Table 3.1: Results of Mauchly's test and Greenhouse-Geisser correction

	Mauchly's test				Greenhouse-Geisser correction							
	W	x^2	df	p	df M	df E	F	P	E	Adj. df1	Adj. df2	Adj. p
Method	0.05	33.72	2	0.00	2	24	3.18	0.06	0.51	1.02	12.29	0.10
Bone	1				1	12	0.69	0.42	1	1.00	12	0.42
Time	0.57	6.26	2	0.04	2	24	28.80	0.00	0.70	1.39	16.73	0.00
Method \times Bone	0.18	18.9	2	0.00	2	24	0.80	0.46	0.55	1.10	13.18	0.40
Method \times Time	0.03	35.3	9	0.00	4	24	16.71	0.00	0.41	1.63	19.59	0.00
Bone \times Time	0.14	21.3	2	0.00	2	24	12.75	0.00	0.54	1.08	12.93	0.00
Method \times Bone \times Time	0.05	31.3	9	0.00	4	24	2.81	0.04	0.55	2.18	26.18	0.07

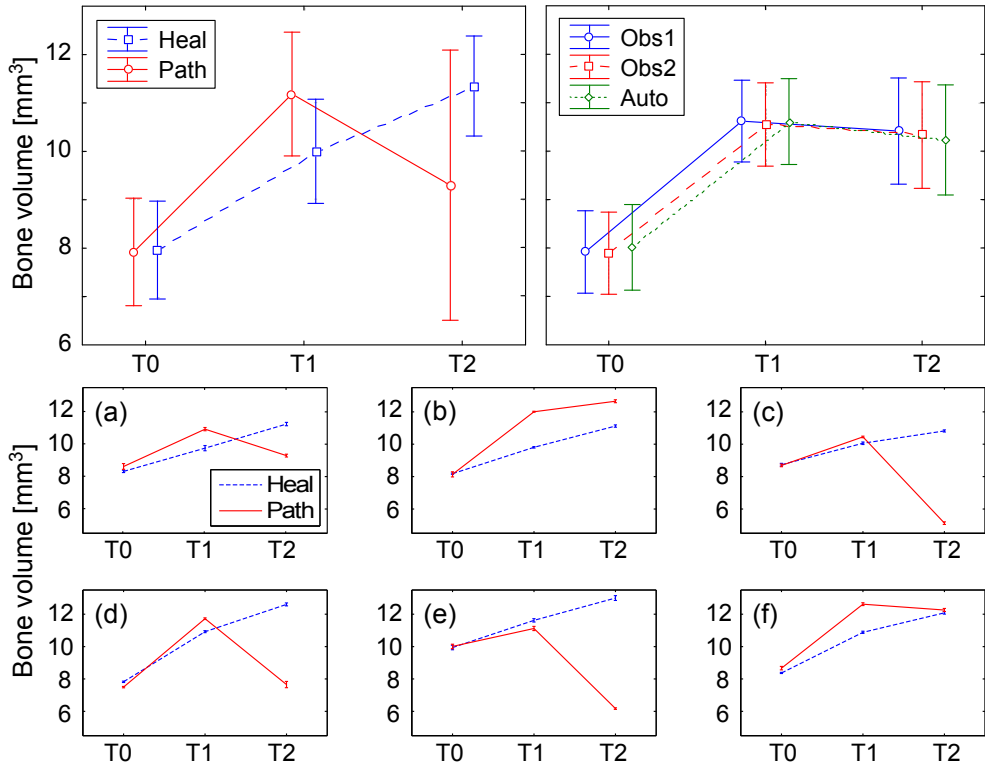


Figure 3.6: Mean volumes of the tibia. Mean bone volume (mm^3) over time for the pathologic (Path) and the healthy (Heal) bones, respectively (top row), Bone \times Time interaction (left) and bone volume over time for the two human observers (Obs1, Obs2) and the automated method (Auto), Observer \times Time interaction (right). The results are based on including all mice. Error bars indicate 95% confidence intervals. Mean bone volume (mm^3) and the standard deviation of the healthy (Heal) and pathologic (Path) bones for six different mice (a-f) over time, averaging the measurements of the automated method and the two human observers (middle and bottom rows).

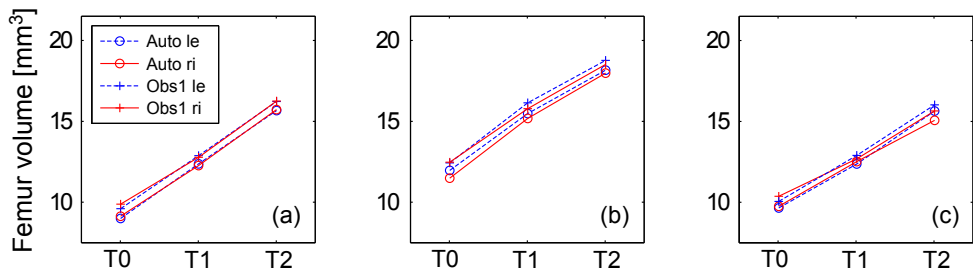


Figure 3.7: Volume measurements of the femur. Result of the automated (Auto) and manual (Obs1) volume measurement for the right (ri) and left (le) femur for three different mice (a-c) over time.

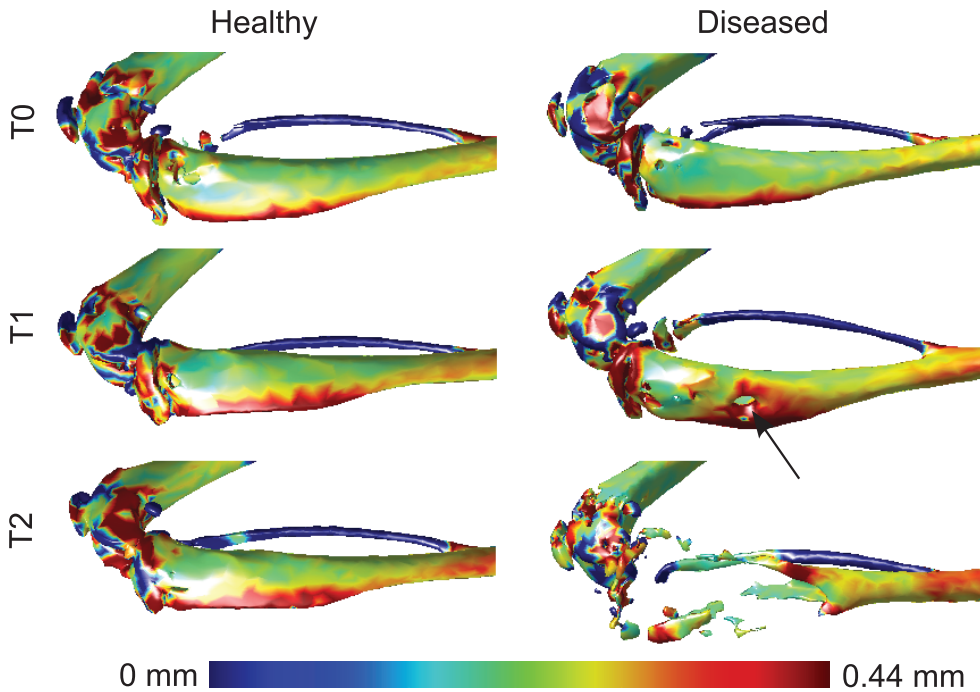


Figure 3.8: Bone thickness maps. Comparison of the bone thickness development over time for a healthy and a pathologic bone. Bone surface representations are shown. The colors indicate the bone thickness at each location on the bone. The bone marrow was partially flushed out of the bone during the intra-osseous inoculation used to induce bone metastases. This partial bone marrow ablation leads to a local increase in bone volume preceding cancer-induced osteolysis.⁶ The arrow indicates this local increase in bone thickness around the site of early osteolysis. Note that the measurements at the distal end of the femur and the proximal end of the tibia are not meaningful because at these locations, a substantial amount of trabecular bone is present. However, bone thickness measurements are only meaningful for cortical bone.

An automated method for μ CT analysis has several advantages over manual analysis. The risk of non-objectivity and inter-observer variability is greatly reduced by minimizing the active manual input of the researcher. Only an automated approach can be purely objective and handle every dataset in exactly the same manner. Additionally, an automated analysis method is much faster than any manual procedure. Thus, by automating the analysis, a relatively larger number of scans can be evaluated, compared to a human observer

Researchers want to know exactly how quantified data is generated and tend to dislike automated black-box approaches. To enable the researcher to check every step along the way, the automated method generates visualizations of the segmented volume. These visualizations can be evaluated after the analysis is complete. The automatic segmentation can be overruled manually or some datasets can be excluded from further analysis. Moreover, the cortical thickness maps enable the researcher to directly pinpoint where structural changes of the cortical bone occurred. This way, the cortical thickness maps help identify areas of interest in the original scan data and in other modalities such as histological sections. The assessment of trabecular bone is not possible with the proposed method because the relatively low resolution of the *in vivo* data ($36.5 \times 36.5 \times 36.5 \mu\text{m}^3$) renders measuring the trabecular thickness accurately very difficult.¹⁷

We validated the presented automated method by comparing it to the “best available” method, namely manual bone segmentation and bone volume measurements. Therefore, we acquired datasets of 15 mice ($n = 15$) with induced bone metastases in the tibia at three points in time. The volume measurement results show that there is an excellent correlation between the human observers and the automated method: $r_{Obs1Obs2} = 0.9996$, $r_{AutoObs2} = 0.9939$, and $r_{AutoObs1} = 0.9937$. The Bland-Altman plots (Figure 3.5, bottom row) based on all data indicate excellent agreement among the two human observers (inter-observer variability) as well as the observers and the automated method. There is no obvious relation between the difference and the mean. Residual disagreement can therefore be explained by the bias and the deviation, which is very low in all cases, namely $0.59 \pm 0.64\%$, $0.26 \pm 2.53\%$, and $-0.33 \pm 2.61\%$, respectively. The residual errors are the result of mainly two factors that may influence the measurement outcome: the registration accuracy, and subsequently the segmentation accuracy, and the chosen threshold to separate bone from the background. The registration accuracy has the largest influence on the result and therefore, improving the accuracy would require a modification of the registration method. Special attention should be paid to the robustness of potential methods with respect to bone resorption. The thresholding procedure also influences the measured volume because both values are inversely related, i.e., if the threshold value increases, the volume decreases and vice versa. We chose a global threshold since the resolution of the *in vivo* data does not allow reliable segmentation of the trabecular bone¹⁷ but methods including local thresholds may be more accurate, if data resolution increases.

Ideally, the automated measurements are identical to the manual measurements.

The ANOVA revealed no significant difference between observers (Method, $p = 0.10$). This means that the automated method is performing equally well as the two human observers. However, the low p value indicates that significant interaction effects may be present. It appears that there is some dependency of the performance of the automated method on the time point since the automated method is significantly different from the human observers at T0 and T2. Visual inspection of Figure 3.6 (top right) suggests overestimation of the volume at T0 and underestimation of the volume at T2. There is no significant difference at T1. This is supported by the Bland-Altman plots (Figure 3.5, bottom row) in which the mean difference in measurement is close to zero at T1. However, these differences are borderline and probably due to the very small variation between the human observers.

The bone volumes of pathologic bones were significantly decreased compared to the healthy bones at T2 (Figure 3.6, top left). There are no significant differences at T0 and T1. There are two explanations why there is no volume decrease at earlier time points. Firstly, the bone marrow is partially flushed out of the bone during the intra osseous injection of tumor cells. This partial bone marrow ablation has profound anabolic effects on local bone turnover. Bone formation induced by bone marrow ablation reaches a maximum of 1 week after the intervention. After this initial week, the bone volume normalizes gradually over time as the bone recovers from the procedure, a process that can take weeks.^{18,19} Secondly, starting osteolytic lesions around the tumor create weak areas in the bone. The mechanical stress on other healthy parts of the bone will increase due to these weak areas. Both the anabolic effects due to the partial bone marrow ablation and due to the increased mechanical stress result in a local increase of bone volume alongside osteolytic lesions. Combined, these anabolic and osteolytic processes influence the volume measurements as can be seen in Figure 3.6 (middle and bottom rows, a–d and f). The cortical thickness maps provide an excellent tool to see exactly where the volume changes occur in relation to the osteolytic lesion site (Figure 4.4).

The presented segmentation method is not restricted to the tibia, but can be applied to any bone of the skeleton in whole-body μ CT scans, as long as it is contained in the MOBY mouse atlas.^{7,9,20} We are currently implementing the volume measurements of every segmented skeletal element using the same principle. We segmented the femur as preliminary proof of concept. Several conclusions can be drawn from the results in Figure 3.7. The volumes of the right and the left femur are very similar for the manual and the automated measurement, meaning that measuring the femur is highly reproducible. The automated method, however, underestimates the volume compared the manual method. This underestimation is to be expected since the femur included in the MOBY mouse atlas does not include the femoral head and neck. Therefore the segmentation result “cuts” the femoral neck approximately in the middle and the amount of underestimated volume thus corresponds to the volume of the femoral head and part of the femoral neck. Note that this is a systematic error and only leads to inaccurate results if the femoral head and neck are of particular interest within a study. The same type of measurement error may occur for other bones as

well, since most of the bones in the MOBY atlas are simplified versions of the real bone shape. However, as is the case for the femur, this should not lead to problems because the error is systematic. In the cases where higher segmentation accuracies are required in a particular part of the bone that is simplified, another animal model with more details could be employed. One should however bear in mind that using simplified bone shapes has the advantage that the influence of, e.g., differences in strain or animal size can be minimized by leaving out the fine details.

The increased radiation dose of μ CT compared with radiographs has always been a major concern limiting its use in cancer research. This is not a problem anymore as modern μ CT scanners can perform whole-body scans in less than a minute.²¹ The delivered radiation dose during these scans is well below a dose that would affect tumor growth, even during longitudinal follow-up studies.^{21–23}

All datasets used in this article have been generated with a standard scanning protocol using the Skyscan 1076 μ CT. However, the described methods can be performed on any other whole-body μ CT dataset acquired on a different machine and with a different protocol. Other scans might require an adjustment of threshold values and the initial scan resolution will always be a limiting factor during further analysis.

Finally, we want to stress that the described method is general and can be applied to others species as well. The only prerequisite is that an anatomical skeleton atlas is available for the animal of interest.

Conclusion

We suggested a new μ CT analysis paradigm based on the combined approach of previously published methods for animal posture correction, normalized visualization of follow-up data, and the quantification and visualizations discussed in this paper. Together, this results in a fast and automated workflow, in which the user can easily compare whole-body μ CT scans on the whole-body level, zoom in to the level of a single bone or bone segment of choice, and gain qualitative and quantitative data of that segment. The animals can be scanned in any posture. Normalized and interactive side-by-side visualizations of the exact same section of skeletal elements at different time points can be generated from longitudinal scans in which one animal is scanned multiple times over time. The detailed side-by-side visualizations greatly help the researcher to identify changes in the skeleton. The researcher can then identify and zoom in on the bone or bone segment of interest and automatically generate quantitative volumetric data alongside visualizations of the segmented volume and visualizations of the cortical thickness of that specific skeletal element. This new workflow greatly reduces analysis time, aids the handling of complicated scan data and improves the overall qualitative and quantitative assessment of μ CT scans. The method was validated by quantification of osteolytic effects over time in the tibia but can easily be adapted to other bones of the skeleton. In addition, the approach can be used for other species as well, given that an animal skeleton atlas exists for that

animal.

Acknowledgments

The authors gratefully acknowledge Marieke Thurlings and Ron Wolterbeek for helping with the statistical analysis. This research was supported by the Dutch Cancer Society Koningin Wilhelmina Fonds (grant UL2007-3801) (TS) and the European Network for Cell Imaging and Tracking Expertise (ENCITE), which was funded under the 7th framework program.

References

1. Abrams HL, Spiro R, and Goldstein N. Metastases in carcinoma; analysis of 1000 autopsied cases. *Cancer*, 1950 Jan;3(1):74–85.
2. Guise TA and Mundy GR. Cancer and bone. *Endocr Rev*, 1998 Feb;19(1):18–54.
3. Mundy GR. Metastasis to bone: causes, consequences and therapeutic opportunities. *Nat Rev Cancer*, 2002 Aug;2(8):584–93.
4. Nakai M, Mundy GR, Williams PJ, Boyce B, and Yoneda T. A synthetic antagonist to laminin inhibits the formation of osteolytic metastases by human melanoma cells in nude mice. *Cancer Res*, 1992 Oct;52(19):5395–9.
5. Sasaki A, Boyce BF, Story B, Wright KR, Chapman M, Boyce R, Mundy GR, and Yoneda T. Bisphosphonate risedronate reduces metastatic human breast cancer burden in bone in nude mice. *Cancer Res*, 1995 Aug;55(16):3551–7.
6. Snoeks TJA, Kaijzel EL, Que I, Mol IM, Löwik CWGM, and Dijkstra J. Normalized volume of interest selection and measurement of bone volume in microct scans. *Bone*, 2011 Dec;49(6):1264–9.
7. Baiker M, Milles J, Dijkstra J, Henning TD, Weber AW, Que I, Kaijzel EL, Löwik CWGM, Reiber JHC, and Lelieveldt BPF. Atlas-based whole-body segmentation of mice from low-contrast micro-ct data. *Med Image Anal*, 2010 Dec;14(6):723–37.
8. Kovacevic N, Hamarneh G, and Henkelman M. Anatomically guided registration of whole body mouse mr images. In R Ellis and T Peters, editors, *Medical Image Computing and Computer-Assisted Intervention - MICCAI 2003*, volume 2879 of *Lecture Notes in Computer Science*, pages 870–877. Springer Berlin / Heidelberg. ISBN 978-3-540-20464-0, 2003;.
9. Kok P, Baiker M, Hendriks EA, Post FH, Dijkstra J, Löwik CWGM, Lelieveldt BPF, and Botha CP. Articulated planar reformation for change visualization in small animal imaging. *IEEE Trans Vis Comput Graph*, 2010;16(6):1396–404.
10. Peyruchaud O, Winding B, Pécheur I, Serre CM, Delmas P, and Clézardin P. Early detection of bone metastases in a murine model using fluorescent human breast cancer cells: application to the use of the bisphosphonate zoledronic acid in the treatment of osteolytic lesions. *J Bone Miner Res*, 2001 Nov;16(11):2027–34.
11. Wetterwald A, van der Pluijm G, Que I, Sijmons B, Buijs J, Karperien M, Löwik CWGM, Gautschi E, Thalmann GN, and Cecchini MG. Optical imaging of cancer metastasis to bone marrow: a mouse model of minimal residual disease. *Am J Pathol*, 2002 Mar;160(3):1143–53.
12. Webb AR. *Statistical Pattern Recognition, 2nd Edition*. John Wiley & Sons, 2002 October.
13. Hildebrand T and Ruegsegger P. A new method for the model-independent assessment of thickness in three-dimensional images. *Journal of Microscopy*, 1997;185(1):67–75.

14. Ho V and Reddy G, editors. *Chapter 84 - Advanced three-dimensional postprocessing in computed tomographic and magnetic resonance angiography. In: Cardiovascular Imaging: Vascular imaging. Pt. 11. Vascular anatomy and circulation.* Expert radiology series. Saunders/Elsevier, 2011. ISBN 9781416053354.
15. Bland JM and Altman DG. Statistical methods for assessing agreement between two methods of clinical measurement. *Lancet*, 1986 Feb;1(8476):307–10.
16. Field A and Miles J. *Discovering Statistics Using SAS.* SAGE, 2010. ISBN 9781849200912.
17. Waarsing JH, Day JS, and Weinans H. An improved segmentation method for in vivo microct imaging. *J Bone Miner Res*, 2004 Oct;19(10):1640–50.
18. Bab I, Gazit D, Muhlrad A, and Shteyer A. Regenerating bone marrow produces a potent growth-promoting activity to osteogenic cells. *Endocrinology*, 1988 Jul;123(1):345–52.
19. Patt HM and Maloney MA. Bone marrow regeneration after local injury: a review. *Exp Hematol*, 1975 Apr;3(2):135–48.
20. Segars WP, Tsui BMW, Frey EC, Johnson GA, and Berr SS. Development of a 4-d digital mouse phantom for molecular imaging research. *Mol Imaging Biol*, 2004; 6(3):149–59.
21. Lim E, Modi K, Christensen A, Meganck J, Oldfield S, and Zhang N. Monitoring tumor metastases and osteolytic lesions with bioluminescence and micro ct imaging. *J Vis Exp*, 2011;,(50).
22. Foster WK and Ford NL. Investigating the effect of longitudinal micro-ct imaging on tumour growth in mice. *Phys Med Biol*, 2011 Jan;56(2):315–26.
23. Johnson LC, Johnson RW, Munoz SA, Mundy GR, Peterson TE, and Sterling JA. Longitudinal live animal micro-ct allows for quantitative analysis of tumor-induced bone destruction. *Bone*, 2011 Jan;48(1):141–51.

4

Towards an Integrated Approach for Whole-Body Multimodality Imaging of Bone Metastases

Thomas J.A. Snoeks ¹
Martin Baiker ²
Eric L. Kaijzel ¹
Boudewijn P.F. Lelieveldt ^{2 3}
Clemens W.G.M. Löwik ¹

submitted

¹Dept. of Endocrinology, LUMC, Leiden, The Netherlands

²Dept. of Radiology, Division of Image Processing LKEB, LUMC, Leiden, The Netherlands

³ICT Group, Dept. of Mediamatics, Delft University of Technology, Delft, The Netherlands

Abstract

The pathogenesis of bone metastases is a complex and multifaceted process. Often multiple imaging modalities are needed to follow both the structural and functional changes over time during metastatic bone disease. Researchers face extended datasets of one experiment acquired with multiple modalities at multiple points in time. This review gives an overview of an integrated approach for handling this kind of complex data. It focuses on the analysis of whole-body μ CT and optical data handling. We show how researchers can generate side-by-side visualizations of scans taken with one imaging modality at multiple time points and with multiple modalities at one time point. Moreover we highlight methods for normalized volumes of interest selection and quantification of bone volume and thickness.

Introduction

Bone is one of the preferred sites of breast cancer and prostate cancer metastases. *Post mortem* examination revealed that approximately 70% of patients who died of breast or prostate cancer carried bone metastases.¹ The attraction of certain types of cancer towards bone was already noted in 1889 by Stephen Paget² and has been well studied ever since.

The clinical manifestations of overt bone metastases are vast, ranging from severe osteolysis to osteoblastic calcifications outside the bone and inside the marrow cavity.³ Bone metastases are a clinical predictor of poor survival for both breast and prostate cancer patients. The pathology of this so called metastatic bone disease is a result of a complex interactions between the tumor and the bone micro-environment. The crosstalk between the tumor and bone results in the disruption of the delicate balance between osteoclasts and osteoblasts.^{4,5}

Key regulators involved in osteolytic bone metastases are parathyroid hormone related protein (PTHrP) produced by the tumor and transforming growth factor- β (TGF- β) released from the bone upon resorption. PTHrP stimulates osteoclastogenesis and prolongs osteoclast survival. The released TGF- β stimulates PTHrP production by the tumor. It furthermore stimulates proliferation and apoptosis resistance together with other growth factors which are released from the resorbed bone matrix. This positive feedback loop is known as the vicious cycle of osteolytic bone metastases.^{4,5}

Bone metastases are difficult to treat because of the strong positive feedback loop between the tumor and the bone micro-environment. Research towards treatment of bone metastases is in need of reliable methods to quantify bone specific effects of experimental treatments *in vivo*. Imaging can be an informative tool for that purpose, providing qualitative as well as quantitative results. Here we give an overview of both the structural and functional whole-body imaging modalities which can be used in research on metastatic bone disease as well as on other bone related diseases. We will focus on recent advances in normalized comparison of datasets of one animal made at different points in time and combining data generated with multiple imaging modalities.

Structural Imaging

Pre-clinical imaging modalities can be grouped in two classes, structural imaging modalities such as X-ray based imaging and functional imaging modalities such as bioluminescence imaging (BLI), fluorescence imaging (FLI), positron emission topography (PET) and single photon emission computed tomography (SPECT). Structural imaging modalities are used to visualize and quantify structural and architectural features of the skeleton, whereas functional imaging modalities are used to gain insight in cellular, metabolic and molecular processes within and around cancerous bone lesions. Since decades, structural imaging of bone and bone lesions has been

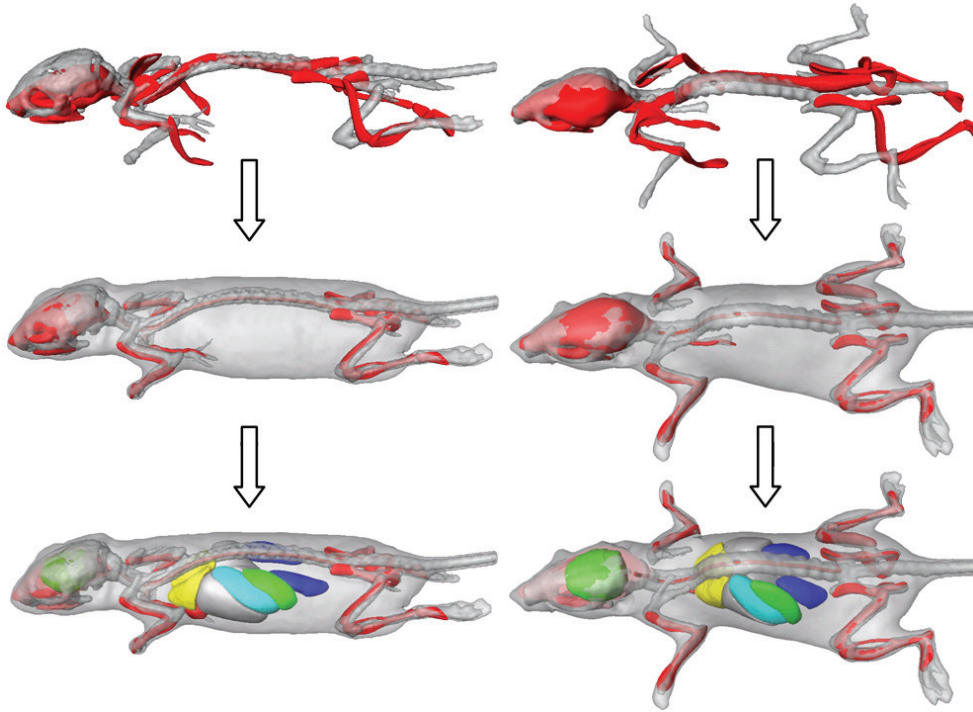


Figure 4.1: Aligning the articulated atlas with μ CT data. Registration results between the atlas (red) and two different subjects (grey) after coarsely aligning the skeleton (top), after the articulated registration (middle), and after organ approximation (bottom). Adapted with permission from⁸

performed with radiography. The advances in digital computing enabled the development of three dimensional (3D) computed tomography (CT) by Godfrey Hounsfield during the 1970s which was a major revolution in the field of X-ray based imaging.^{6,7} Nowadays, specialized micro-CT (μ CT) scanners are available for small laboratory animals with resolutions of several micrometers.

Posture Correction

The posture of entire animals varies greatly between scans taken at multiple time points. As a result, it can be difficult to identify small osteolytic lesions in longitudinal μ CT datasets, even for an experienced observer.⁹ For some applications, dedicated animal holders can be used to reduce the postural variability,¹⁰ but such holders are often not sufficient and limit the throughput, especially for multi-modality studies. Therefore, compensation for large posture variations between scans taken at different time points is needed, to enable the user to identify small lesions within these large,

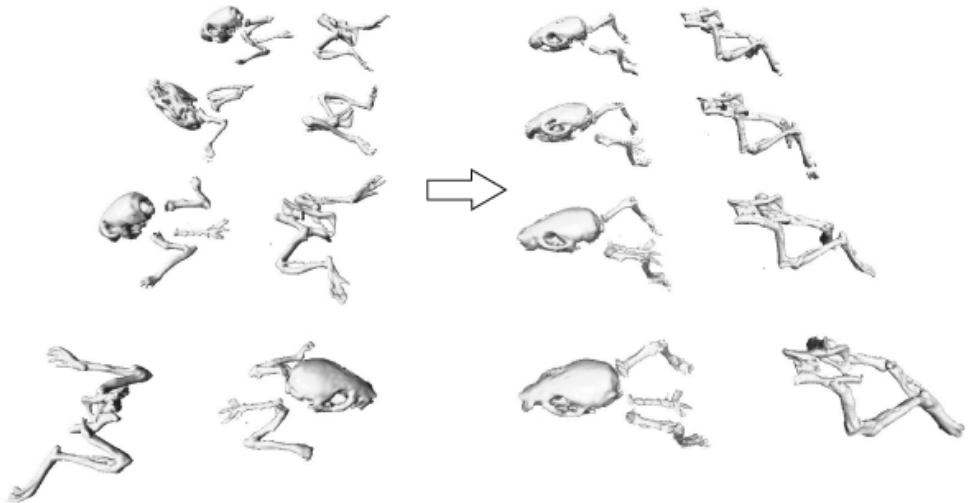


Figure 4.2: Demonstration of mapping the skeletons of four different animals to a common reference domain. The large postural differences of the animals (left) are not present anymore (right), enabling a more intuitive comparison of different time points. Adapted with permission from ⁸

complex whole-body μ CT datasets.

To compensate for the postural differences between scans, a method has been developed based on matching an atlas to whole-body μ CT datasets. For this purpose Khmelinskii *et al.* developed kinetic mouse and rat atlases. The skeletons of these atlases have been segmented and each individual skeletal element has been identified. In addition, each joint position has been annotated and the kinetic degrees of freedom have been specified.⁸ The posture of such an articulated atlas can be changed to fit the skeleton of an actual animal μ CT scan. Also, the positions of major internal organs without μ CT contrast are approximated based on the positions of the skeletal elements, lungs and skin (Figure 4.1).⁹ Baiker *et al.* developed a fully automated system for aligning the atlas with μ CT scans. The automated system can effectively perform posture corrections in the absence of soft-tissue contrast in *in vivo* μ CT data and without requiring user initialization. The approach is robust with respect to large postural variations and to moderate, pathology-induced structural variations.⁹ After aligning the atlas with the scan data, the skeletal elements of the scanned animal can be repositioned to a standardized posture. This articulated atlas-based repositioning of the skeleton facilitates fast data comparison (Figure 4.2).⁸

Side-by-side Visualizations

Intra-cardiac injection of bone specific MDA-MB-231 breast cancer cells is a popular method to induce osteolytic cancer metastases in the skeleton. Bone metastases will develop at several sites throughout the skeleton within one to three weeks after inoculation with cancer cells. Disease progression of these osteolytic lesions can be followed by comparing whole body μ CT scans taken at different time points. However, the initial structural disease induced changes in this kind of follow-up datasets can be very small and difficult to identify in complex 3D datasets. Posture normalization of the datasets is helpful, but often not enough. Kok *et al.* developed an approach which enables side-by-side visualizations of an individual skeletal element at different time points. The data used for these detailed visualizations is extracted from longitudinal whole-body μ CT datasets.¹¹

The generation of side-by-side visualizations individual skeletal elements is a multi-step process. First, the μ CT datasets taken at each time point are aligned. Next, the scan is divided in normalized sub-volumes which are placed around each of the skeletal elements. These sub-volumes are then used to generate an “exploded view” (Figure 4.3a) of the skeleton. Finally, the sub-volumes are mapped into a common reference frame using articulated planar reformation (APR), where corresponding volumes of interest (VOIs) are visualized side-by-side (Figure 4.3b-c). The visualizations of the different time points are coupled, in other words, the user selects a section or visualization of a skeletal element of a scan taken at one time point and the system will automatically generate the corresponding visualization of the other time points.¹¹

Methods of mapping data into a common reference frame make the use of animal holders during data acquisition obsolete because postural differences can be compensated for afterwards. The use of sub-volumes per skeletal element not only has the advantage of aligning structures of interest between time-points, it also enables data analysis at full resolution because only a small part of the whole-body dataset is loaded. This is often not possible for whole-body datasets because of the extreme computing requirements due to the large amount of data.

Quantification

Treatment and intervention studies on bone metastases often require the quantification of several bone parameters. Currently, the quantification of osteolytic lesions is performed by drawing a region of interest (ROI) around the lesion on two dimensional (2D) radiographs and measuring the lesion surface.^{12,13} Lesions projected on top of each other and lesions on the side of bone will be underestimated when quantified due to the flattening of the 3D structure (Figure 2.6).¹⁴ The large dependency on manual input results in a strong dependence on experience of the observer and makes the method prone to observer bias. The scoring of such radiographs cannot be automated due to variability of shape and grey-values between various bones and lesions.

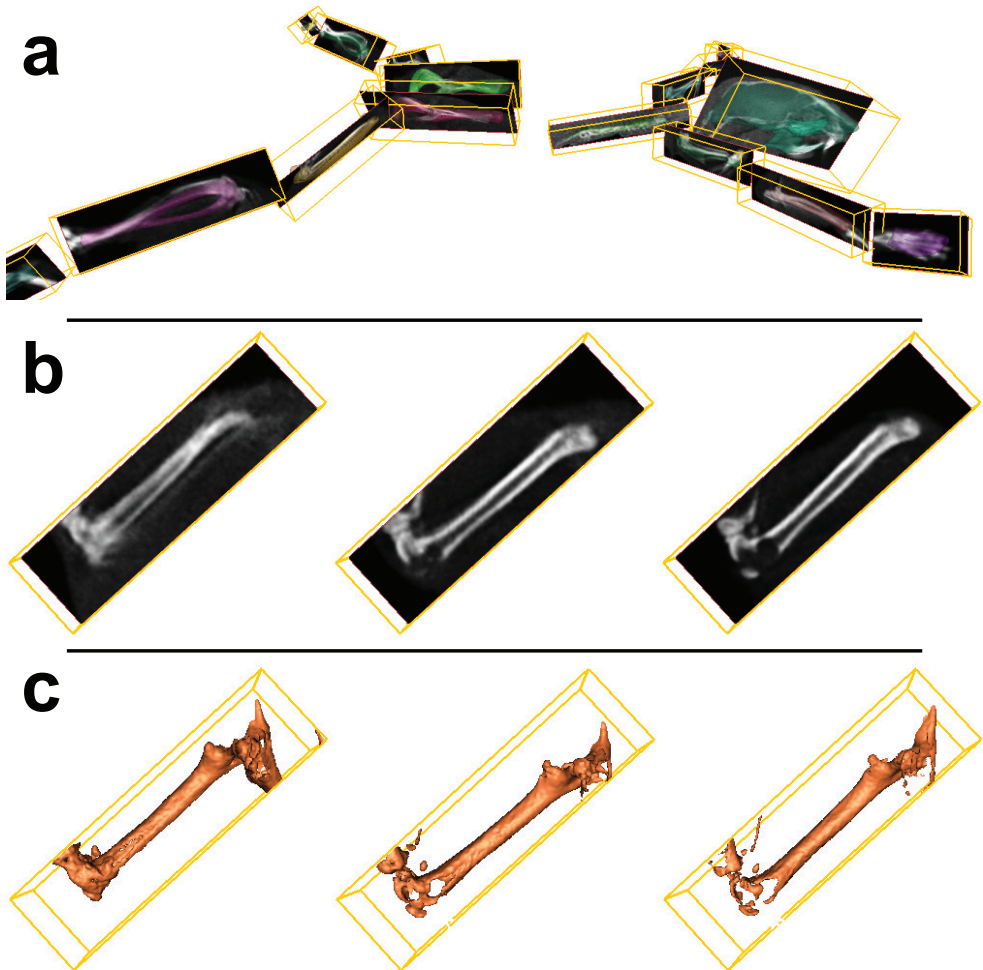


Figure 4.3: Exploded view and side-by-side visualizations of longitudinal μ CT data. Osteolytic bone metastases were induced by intra-cardiac injection of $1 \cdot 10^6$ MDA-MB231-BO2 cells (an osteolytic, bone specific subclone of the MDA breast carcinoma cell line) in a 6 week old nude mice. μ CT scans were made 3, 5 and 6 weeks after inoculation. The animal was scanned in a different posture per time-point, supine (week 3) and prone (week 5 and 6). (a) Longitudinal μ CT data has been aligned with the articulated mouse atlas to eliminate differences in posture. Next, the scans were divided over sub-volumes per skeletal element. Structural changes between time points have been highlighted. These areas are potentially interesting to the user for further, in depth, inspection. The femur has been selected and is shown side-by-side in detailed views for the three available time points at 3, 5 and 6 weeks into the experiment (b) and (c). Shown for each time point are an image plane that can be interactively moved through the volume (b) and a surface rendering of the entire femur (c). At 5 and 6 weeks, bone resorption can clearly be seen near the knee area (indicated by the arrows), even though the animal posture in the original data was highly variable. Note that between the first and second time point, with the subject at 10 and 12 weeks of age respectively, some growth is still taking place, which has to be taken into account when analyzing the images. Figure adapted with permission from¹¹

μ CT is a 3D modality and therefore datasets provide more accurate information on disease induced changes like an increase or decrease in bone volume, bone thickness and bone density, both for visual and quantitative assessment. However, the selection of a VOI in 3D datasets is more complex than ROI selection in 2D data.

A multi-planar reformation (MPR) based approach for normalized selection of VOIs in complex 3D shapes has been published (Chapter 2).¹⁴ The approach makes use of a center-line which has been fitted through an individual bone. This naturally curved center-line can then be “straightened” to generate a new, normalized volume. The straightened bone is orientated along the z-axis of this new volume. The volume can then be used to extract normalized cross-sections or to define a normalized VOI (Figure 2.2). The selected VOI is mapped back to the original scan volume, where the actual volume measurements are performed. This way, the volume measurements are not influenced by introduced artifacts due to the straightening procedure. The VOIs selected following this method are predefined and relative to the anatomy of the bone. This way, the VOI selection is independent of the observer, reducing the chance of observer bias. Moreover, it becomes possible to select exactly the same part of multiple bones, enabling data comparison between multiple scans.¹⁴ This approach has been automated and integrated it in the exploded view visualization system (Chapter 3).¹⁵

In addition to volume measurements, μ CT scans can be used to determine cortical bone thickness. This type of measurements were added to the exploded view workflow. The cortical thickness is measured and projected as a color code on a volume rendering of the bone. Figure 4.4 shows an example of such thickness maps. In this example, osteolytic breast cancer cells were inoculated in the tibia of nude mice. There is an initial increase in cortical bone thickness around the lesion. After this initial increase, the bone disappears as the local tumor grows and stimulates osteolysis.¹⁵ These kind of visualizations are, like volume measurements, of use for the evaluation of both osteolytic and osteosclerotic lesions.

Altogether, the automated workflow for whole-body μ CT scans described above enables the user to select and zoom in on each individual skeletal elements, visually assess structural changes over time of the selected bone and quantify the volumes of pre-defined VOIs within that bone. μ CT provides excellent structural and volumetric information and can be used to track changes over time, however this modality is limited to tissues with a high X-ray contrast.

Functional Imaging

Functional imaging modalities are used to gain an insight in cellular, metabolic and molecular processes. Functional imaging includes not only optical imaging modalities such as BLI and FLI but also MRI and radioactive imaging methods such as PET and SPECT.

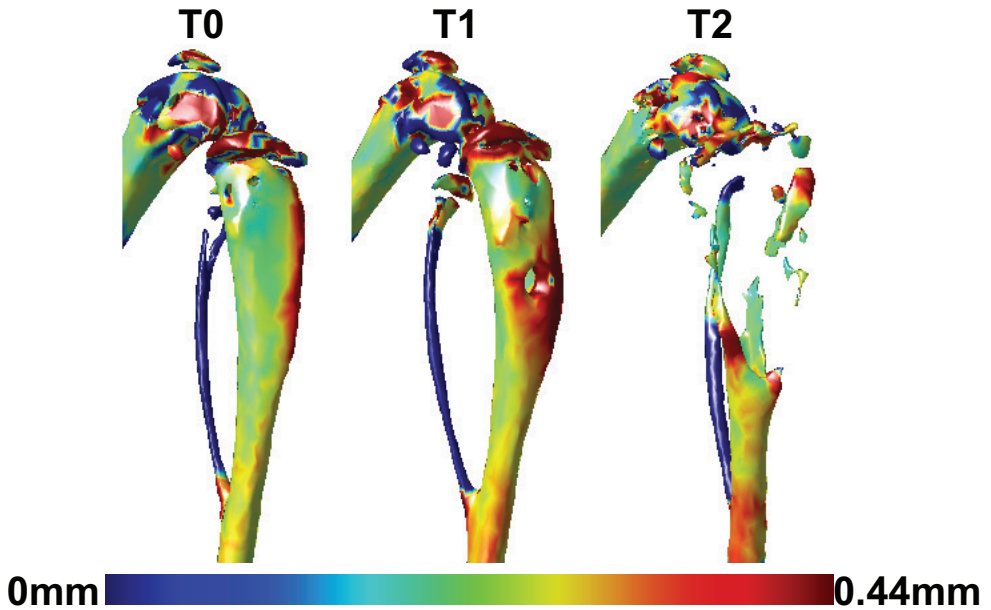


Figure 4.4: Cortical thickness maps. MDA-231-B/luc+ cells ($2.5 \cdot 10^5$ cells) were inoculated directly into the right tibia of a 6 week old female nude mouse. Whole-body μ CT scans were made before inoculation (T0), 3 weeks after inoculation (T1) and 6 weeks after inoculation (T2). The measured cortical thickness is mapped to surface representations of tibia, by means of a colormap. The initial osteolytic lesion is surrounded by an area of increased bone thickness at T1. The increased thickness is mainly a result of the inoculation procedure. Most of the cortical bone has disappeared at T2. This method of evaluating bone thickness can only be used for cortical bone and not at the distal part of the femur or the proximal part of the tibia because of distortion of the measurement due to the presence of trabecular bone. Adapted with permission from ¹⁵

Optical Imaging

Optical imaging modalities are based on capturing photons in the visible and near infrared (NIR) part of the spectrum originating from cells and tissues. These photons can be produced by either fluorescence or bioluminescent enzymatic reactions. The choice between using fluorescence or bioluminescence greatly depends on the research question. Bioluminescence gives an indication of cell metabolic activity or activation of certain signaling cascades whereas fluorescence can be used for imaging of cell tracking and enzymatic activity.

BLI is most commonly used to follow *in vivo* tumor growth of luciferase expressing tumor cells over time.¹⁶ In addition, there are a number of transgenic animal models expressing luciferase under tissue specific promoters such as the prostate specific PSA-Luc mouse¹⁷ and transgenic animals that lumines upon upregulation or activation of certain signaling cascades such as the VEGF receptor 2 luciferase mouse (FVB/N-Tg-(VEGFR2-Luc)-Xen).¹⁸

FLI can be used for tracking of cells expressing certain fluorescent proteins. Other approaches to FLI make use of targeted fluorescent dyes or probes which fluorescence upon enzymatic activation such as the matrix metalloproteinase specific MMPsense (PerkinElmer)¹⁹ and various cysteine proteinase activity-based probes (ABPs).^{20–24} The fluorophore of ABPs binds specifically and covalently to the active domain proteases. The fluorescence can be monitored *in vivo*, but can also be detected in histology can sections or on western blots because of the covalent bond. This enables the exact *ex vivo* validation and quantification of the signal after the *in vivo* study. Two other fluorescent probes of interest to the cancer and bone field are Osteosense (PerkinElmer)²⁵ and BoneTag (LI-COR),^{26,27} both commercially available dyes, which bind specifically to bone at areas of high turnover such as osteolytic and osteosclerotic lesion sites.

BLI and FLI are essentially 2D modalities. However, recent developments in imaging equipment enabled 3-dimensional data capturing and reconstruction. The technological advancements of optical imaging and the use of optical imaging in the field of bone research have been reviewed in detail by Snoeks *et al.*²⁷

PET, SPECT and MRI

PET and SPECT are two closely related radioisotope imaging modalities. Most modern animal PET and SPECT scanner are combined with a CT scanner to provide more structural information. The use of PET and SPECT is limited to a few institutions because of the infrastructure, which is needed for the complicated handling of radio tracers. There is a multitude of radio tracers, which can be used to image and quantify various targets in metastatic bone. Most common are the clinically used radioactive labeled bisphosphonates to assess local hotspots in bone turnover,^{28,29} $\alpha\beta3$ integrin targeted tracers to measure endothelial cell activation³⁰ and radiolabeled deoxyglucose to image areas of high metabolic activity such as tumors and inflammation.^{29,31–33} Both PET and SPECT offer excellent quantification

possibilities but are limited in anatomical and spacial contrast.

Of the functional imaging approaches, MRI is the modality that gives the best anatomical and soft tissue contrast without the use of ionizing radiation. It was first used to image and quantify diffuse bone metastases with and without osteolysis.³⁴ Later measurements of cortical bone thickness were included in MRI analysis to be able to quantify osteolysis in addition to the tumor size.³⁵ Recently, Bauerle *et al.* described a more integrated approach.³⁶ They combined MRI quantification of the tumor size with volumetric measurements performed with μ CT. In addition, they performed vessel size imaging, blood volume measurements and measurements regarding the cellularity of the tumor lesions. This combination of μ CT with various MRI-based measurements provides complementary information on tumor growth, angiogenesis and vascularization, bone destruction and the morphological state of the tumor, and it can be used to follow changes over time and treatment response.³⁶

Integrated Approaches

Imaging can be used to visualize and quantify both structural and functional characteristics of tumors and tissues *in vivo*. Every modality has its own strengths and weaknesses. It is key to combine the data acquired with each modality in order to come to a complete understanding of the disease process or treatment effects. In order to do that, an integrated approach is needed which maps all the data generated with various modalities throughout an experiment and align this data in space and time (Figure 4.5).

The newly developed 3D optical data capturing techniques and subsequent optical 3D datasets allow for projection of this data on more structural modalities such as μ CT (figure 4.6a-c).^{16,27} Optical modalities such as BLI completely lack structural information other than the skin. This is the reason why it is important to acquire the optical data together with structural data like μ CT in the same posture to assure a good estimation of the signal source location. The optical data, coupled to the μ CT data, can then be handled in the same workflow as the other modalities.

MRI and SPECT datasets contain enough anatomical data to be able to fit the articulated atlas.^{8,38} These datasets can then be handled in a similar fashion as the μ CT data. This enables not only side-by-side visualizations of data generated with one modality at different time-points (as is the case in Figure 4.3) but also side-by-side visualizations of data generated at one time-point with different modalities (figure 4.6d-f).^{37,38} The data is semi interactive; the user can select a certain field of view in one dataset and the corresponding field of view will be automatically generated in the datasets of the other modalities.

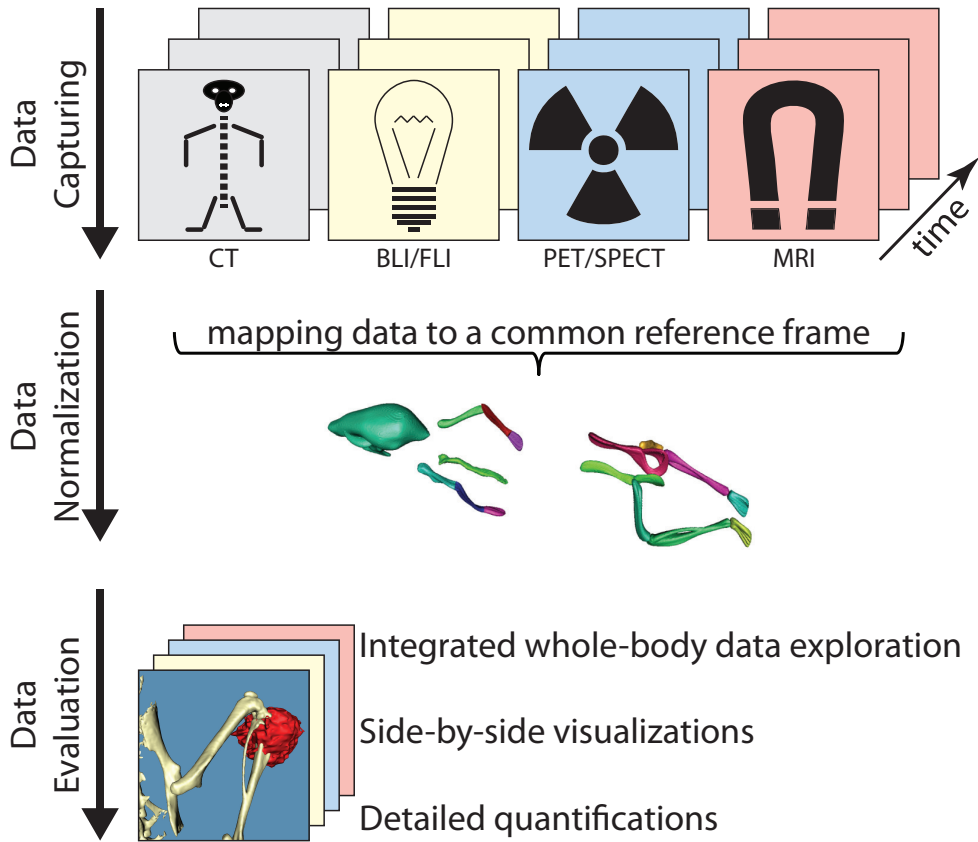


Figure 4.5: Overview of the integrated data workflow. The data generated at different points in time using different modalities is mapped to a common reference frame based on an articulated animal atlas. The atlas is then used to reposition the animal and divide the large datasets in smaller normalized sub volumes. This enables normalized whole-body data evaluation, side-by-side visualizations of a VOI with data generated using multiple modalities at one time-point, side-by-side visualizations of a VOI with data generated using one modality at different time points and various quantifications per modality.

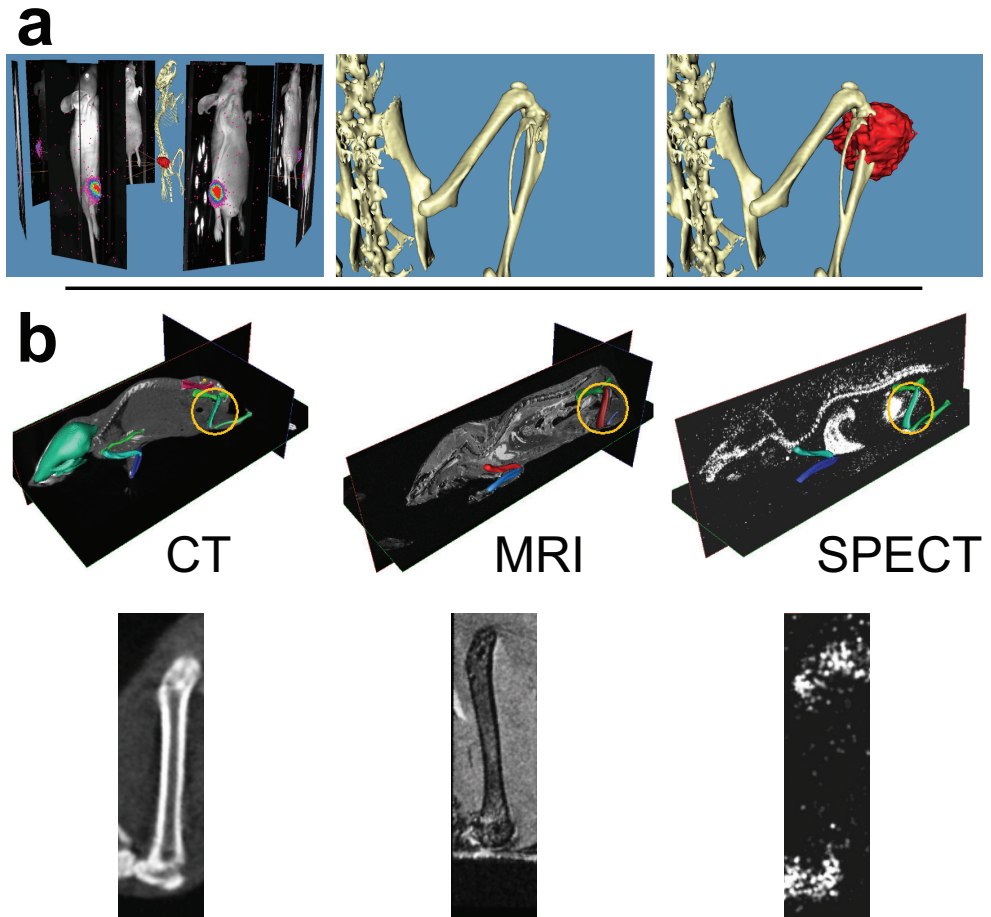


Figure 4.6: Multi-modality visualization of bone metastasis. (a) MDA-231-B/luc⁺ cells ($2.5 \cdot 10^5$ cells) were inoculated directly into the right tibia of a 6 week old female nude mouse. Three weeks after tumor cell inoculation, bone metastases were analyzed with an IVIS 3D BLI Imaging system (Caliper Life Sciences, Alameda, CA). The animal was subsequently scanned in a SkyScan 1076 μ CT scanner (SkyScan, Kontich, Belgium) in the same position as during the BLI measurement. Left: The bioluminescent data captured from 8 positions around the animal was reconstructed and projected back onto a CT reconstruction of the animal. Middle: Detail of the CT volume visualization of the right hind limb. Right: The tumor induced osteolytic lesion is clearly visible. Detail of the BLI tumor volume estimation projected onto the CT reconstruction. The source of the bioluminescent signal co-localizes with the osteolytic lesion site. Adapted with permission from²⁷. (b) Animals imaged with CT, MRI and SPECT at one time point. The articulated atlas has been fit to the scan data (middle row) and side-by-side visualizations of one specific segment have been generated using the atlas-based planar reformation approach. In the near future it will be possible to generate similar multi-modality representations using scans of the same animal. Adapted with permission from³⁷.

Conclusion

The integrated data handling in which all datasets from an experiment are mapped into one common reference frame, as summarized in Figure 4.5, enables the user to explore the data in an intuitive way. The user can assess disease induced lesions by generating side-by-side views of changes over time in one skeletal element. A greater understanding of what is happening in a diseased area of the animal is achieved by combining functional and structural data acquired with various imaging modalities.

Recently a start has been made to implement detailed quantifications, such as bone volume and thickness, into this workflow. This facilitates the objective monitoring of disease induced lesions and the effectiveness of treatment interventions. The detailed quantitative assessment of optical data is still a challenge. The development of whole body articulated atlases containing information on optical properties of various tissues might facilitate the development of better signal quantification methods. The overall logic and workflow of integrated data handling can serve as a vehicle to implement this kind of future developments.

Acknowledgements

This work has been supported by the Dutch cancer Society Koningin Wilhelmina Fonds (grant UL2007-3801) (TS).

References

1. Abrams HL, Spiro R, and Goldstein N. Metastases in carcinoma; analysis of 1000 autopsied cases. *Cancer*, 1950 Jan;3(1):74–85.
2. Paget S. The distribution of secondary growths in cancer of the breast. *Lancet*, 1889; 1:571–3.
3. Mundy GR. Metastasis to bone: causes, consequences and therapeutic opportunities. *Nat Rev Cancer*, 2002 Aug;2(8):584–93.
4. Guise TA and Mundy GR. Cancer and bone. *Endocr Rev*, 1998 Feb;19(1):18–54.
5. Guise TA, Mohammad KS, Clines G, Stebbins EG, Wong DH, Higgins LS, Vessella R, Corey E, Padalecki S, Suva L, and Chirgwin JM. Basic mechanisms responsible for osteolytic and osteoblastic bone metastases. *Clin Cancer Res*, 2006 Oct;12(20 Pt 2):6213s–6216s.
6. Ambrose J and Hounsfield G. Computerized transverse axial tomography. *Br J Radiol*, 1973 Feb;46(542):148–9.
7. Hounsfield GN. Computerized transverse axial scanning (tomography). 1. description of system. *Br J Radiol*, 1973 Dec;46(552):1016–22.
8. Khmelinskii A, Baiker M, Kaijzel EL, Chen J, Reiber JHC, and Lelieveldt BPF. Articulated whole-body atlases for small animal image analysis: construction and applications. *Mol Imaging Biol*, 2011 Oct;13(5):898–910.
9. Baiker M, Milles J, Dijkstra J, Henning TD, Weber AW, Que I, Kaijzel EL, Löwik CWGM, Reiber JHC, and Lelieveldt BPF. Atlas-based whole-body segmentation of mice from low-contrast micro-ct data. *Med Image Anal*, 2010 Dec;14(6):723–37.
10. Kovacevic N, Hamarneh G, and Henkelman M. Anatomically guided registration of whole body mouse MR images. In *Proc. MICCAI*. 2003; pages 870–877.
11. Kok P, Baiker M, Hendriks EA, Post FH, Dijkstra J, Löwik CWGM, Lelieveldt BPF, and Botha CP. Articulated planar reformation for change visualization in small animal imaging. *IEEE Trans Vis Comput Graph*, 2010;16(6):1396–404.
12. Nakai M, Mundy GR, Williams PJ, Boyce B, and Yoneda T. A synthetic antagonist to laminin inhibits the formation of osteolytic metastases by human melanoma cells in nude mice. *Cancer Res*, 1992 Oct;52(19):5395–9.
13. Sasaki A, Boyce BF, Story B, Wright KR, Chapman M, Boyce R, Mundy GR, and Yoneda T. Bisphosphonate risedronate reduces metastatic human breast cancer burden in bone in nude mice. *Cancer Res*, 1995 Aug;55(16):3551–7.
14. Snoeks TJA, Kaijzel EL, Que I, Mol IM, Löwik CWGM, and Dijkstra J. Normalized volume of interest selection and measurement of bone volume in microct scans. *Bone*, 2011 Dec;49(6):1264–9.

15. Baiker M, Snoeks TJA, Kaijzel EL, Que I, Dijkstra J, Lelieveldt BPF, and Löwik CWGM. Automated bone volume and thickness measurements in small animal whole-body microct data. *Mol Imaging Biol*, 2011 Oct;.
16. Kaijzel EL, Snoeks TJA, Buijs JT, van der Pluijm G, and Löwik CWGM. Multimodal imaging and treatment of bone metastasis. *Clin Exp Metastasis*, 2009;26(4):371–9.
17. Hsieh CL, Xie Z, Liu ZY, Green JE, Martin WD, Datta MW, Yeung F, Pan D, and Chung LWK. A luciferase transgenic mouse model: visualization of prostate development and its androgen responsiveness in live animals. *J Mol Endocrinol*, 2005 Oct; 35(2):293–304.
18. Zhang N, Fang Z, Contag PR, Purchio AF, and West DB. Tracking angiogenesis induced by skin wounding and contact hypersensitivity using a vegfr2-luciferase transgenic mouse. *Blood*, 2004 Jan;103(2):617–26.
19. Bremer C, Tung CH, and Weissleder R. In vivo molecular target assessment of matrix metalloproteinase inhibition. *Nat Med*, 2001 Jun;7(6):743–8.
20. Blum G, von Degenfeld G, Merchant MJ, Blau HM, and Bogyo M. Noninvasive optical imaging of cysteine protease activity using fluorescently quenched activity-based probes. *Nat Chem Biol*, 2007 Oct;3(10):668–77.
21. Blum G, Weimer RM, Edgington LE, Adams W, and Bogyo M. Comparative assessment of substrates and activity based probes as tools for non-invasive optical imaging of cysteine protease activity. *PLoS One*, 2009;4(7):e6374.
22. Blum G, Mullins SR, Keren K, Fonovic M, Jedeszko C, Rice MJ, Sloane BF, and Bogyo M. Dynamic imaging of protease activity with fluorescently quenched activity-based probes. *Nat Chem Biol*, 2005 Sep;1(4):203–9.
23. Edgington LE, Berger AB, Blum G, Albrow VE, Paulick MG, Lineberry N, and Bogyo M. Noninvasive optical imaging of apoptosis by caspase-targeted activity-based probes. *Nat Med*, 2009 Aug;15(8):967–73.
24. Kato D, Boatright KM, Berger AB, Nazif T, Blum G, Ryan C, Chehade KAH, Salvesen GS, and Bogyo M. Activity-based probes that target diverse cysteine protease families. *Nat Chem Biol*, 2005 Jun;1(1):33–8.
25. Kozloff KM, Weissleder R, and Mahmood U. Noninvasive optical detection of bone mineral. *J Bone Miner Res*, 2007 Aug;22(8):1208–16.
26. Kovar J, Xu X, Simpson M, and Olive D. Effective bone labelling for in vivo noninvasive imaging in nude mice. In *Joint Molecular Imaging Conference, Providence Rhode Island*. 2007; .
27. Snoeks TJA, Khmelinskii A, Lelieveldt BPF, Kaijzel EL, and Löwik CWGM. Optical advances in skeletal imaging applied to bone metastases. *Bone*, 2011 Jan;48(1):106–14.
28. Ben-Haim S and Israel O. Breast cancer: role of spect and pet in imaging bone metastases. *Semin Nucl Med*, 2009 Nov;39(6):408–15.

29. Chua S, Gnanasegaran G, and Cook GJR. Miscellaneous cancers (lung, thyroid, renal cancer, myeloma, and neuroendocrine tumors): role of spect and pet in imaging bone metastases. *Semin Nucl Med*, 2009 Nov;39(6):416–30.
30. Wadas TJ, Deng H, Sprague JE, Zheleznyak A, Weilbaecher KN, and Anderson CJ. Targeting the alphavbeta3 integrin for small-animal pet/ct of osteolytic bone metastases. *J Nucl Med*, 2009 Nov;50(11):1873–80.
31. Rogers IS and Tawakol A. Imaging of coronary inflammation with fdg-pet: feasibility and clinical hurdles. *Curr Cardiol Rep*, 2011 Apr;13(2):138–44.
32. Wang TC, Hsiao IT, Cheng YK, Wey SP, Yen TC, and Lin KJ. Noninvasive monitoring of tumor growth in a rat glioma model: comparison between neurological assessment and animal imaging. *J Neurooncol*, 2011 Sep;104(3):669–78.
33. Zhao S, Kuge Y, Yi M, Zhao Y, Hatano T, Magota K, Nishijima Ki, Kohanawa M, and Tamaki N. Dynamic 11c-methionine pet analysis has an additional value for differentiating malignant tumors from granulomas: an experimental study using small animal pet. *Eur J Nucl Med Mol Imaging*, 2011 Oct;38(10):1876–86.
34. Gauvain KM, Garbow JR, Song SK, Hirbe AC, and Weilbaecher K. Mri detection of early bone metastases in b16 mouse melanoma models. *Clin Exp Metastasis*, 2005; 22(5):403–11.
35. Weber MH, Sharp JC, Latta P, Hassard TH, and Orr FW. Early detection and quantification of murine melanoma bone metastases with magnetic resonance imaging. *Skeletal Radiol*, 2007 Jul;36(7):659–66.
36. Bäuerle T, Merz M, Komljenovic D, Zwick S, and Semmler W. Drug-induced vessel remodeling in bone metastases as assessed by dynamic contrast enhanced magnetic resonance imaging and vessel size imaging: a longitudinal in vivo study. *Clin Cancer Res*, 2010 Jun;16(12):3215–25.
37. Lelieveldt BPF, Botha CP, Kaijzel EL, Hendriks EA, Reiber JHC, Löwik CWGM, and Dijkstra J. Towards integrated analysis of longitudinal whole-body small animal imaging studies. In *ICASSP*. IEEE. ISBN 978-1-4577-0539-7, 2011; pages 5768–5771.
38. Khmelinskii A, Baiker M, Kok P, de Swart J, Reiber JHC, de Jong M, and Lelieveldt BPF. Atlas-based articulated skeleton segmentation of spect mouse data. In *ISBI*. IEEE. ISBN 978-1-4244-4128-0, 2011; pages 437–440.

5

An *in vitro* Model That Can Distinguish Between Effects on Angiogenesis and on Established Vasculature: Actions of TNP-470, Marimastat and the Tubulin-Binding Agent Ang-510

Jens van Wijngaarden¹ & Thomas J.A. Snoeks¹
Ermond R. van Beek¹
Henny Bloys¹
Eric L. Kaijzel¹
Victor W.M. van Hinsbergh²
Clemens W.G.M. Löwik¹

Biochem Biophys Res Commun. 2010 Jan 8;391(2):1161-5

¹Dept. of Endocrinology, LUMC, Leiden, The Netherlands

²Dept. for Physiology, Inst. of Cardiovasc. Res., VU-MC, Amsterdam, The Netherlands

Abstract

In anti-cancer therapy, current investigations explore the possibility of two different strategies to target tumor vasculature; one aims at interfering with angiogenesis, the process involving the outgrowth of new blood vessels from pre-existing vessels, while the other directs at affecting the already established tumor vasculature. However, the majority of *in vitro* model systems currently available examine the process of angiogenesis, while the current focus in anti-vascular therapies moves towards exploring the benefit of targeting established vasculature as well. This urges the need for *in vitro* systems that are able to differentiate between the effects of compounds on angiogenesis as well as on established vasculature. To achieve this, we developed an *in vitro* model in which effects of compounds on different vascular targets can be studied specifically. Using this model, we examined the actions of the fumagillin derivate TNP-470, the matrix metalloproteinase inhibitor marimastat and the recently developed tubulin-binding agent Ang-510. We show that TNP-470 and marimastat solely inhibited angiogenesis, whereas Ang-510 potently inhibited angiogenesis and caused massive disruption of newly established vasculature. We show that the use of this *in vitro* model allows for specific and efficient screening of the effects of compounds on different vascular targets, which may facilitate the identification of agents with potential clinical benefit. The indicated differences in the mode of action between marimastat, TNP-470 and Ang-510 to target vasculature are illustrative for this approach.

Introduction

A functioning and continuously expanding vascular network is essential for tumor development, growth, survival and metastasis. Given its pivotal role in these processes, tumor vasculature is a highly attractive target in anti-cancer therapy. Moreover, anti-vascular treatment may present with a low risk of developing drug resistance and promises to be effective against a broad spectrum of tumors.^{1,2} Currently, two key approaches to target the tumor's blood vessel network have been developed.^{3,4} One is directed at interfering with angiogenesis while the other aims to affect the already established tumor vasculature.

Angiogenesis is the process involving the outgrowth of new blood vessels from pre-existing vessels, and many compounds that affect tumor angiogenesis *in vitro* have been identified and are currently being investigated in clinical trials. Anti-angiogenic agents that have been tested interfere with different targets, such as angiogenic stimuli, receptor activity and endothelial cells.⁴⁻⁶ The second approach aims at preferential targeting of the already established tumor vascular network and makes use of so-called vascular-disruptive agents (VDAs).⁷⁻⁹ All VDAs currently examined draw on the differences between tumor and healthy vasculature to allow for highly selective targeting of tumor blood vessels.^{10,11}

The VDAs can be divided into two categories: biologic and small-molecule agents (SMAs). Biologic agents include peptides and antibodies that deliver effectors to the tumor endothelium, where SMAs exploit the differences between healthy and tumor vasculature to induce selective vascular dysfunction.¹²⁻¹⁴ Targeting angiogenesis and already established vasculature could both have their role in anti-cancer therapy.

Where tumor angiogenesis is well suited for treating micrometastatic disease and early-stage cancer, disrupting established tumor vasculature leads to rapid vascular collapse, vessel congestion and tumor necrosis and is therefore more efficacious against large, already established tumors. Both approaches have shown promising results in ongoing preclinical studies, but treatments either targeting tumor angiogenesis or established tumor vasculature alone are not fully effective.^{10,15-19} For this reason, current research explores the benefit of combining these anti-vascular treatment strategies.^{13,20-22}

When developing new anti-vascular compounds it would be of great benefit if one could determine if the overall anti-vascular action is mainly due to effects on inhibition of angiogenesis or to suppression of established vasculature or a combination of both. Therefore, in the present study, we developed an assay in which effects of substances on angiogenesis can easily be studied next to those on established vasculature in the same *in vitro* model. In order to validate this model system, we examined the actions of a number of different anti-vascular agents, among which a recently developed combretastatin like tubulin-binding agent Ang-510 (Figure 5.1).

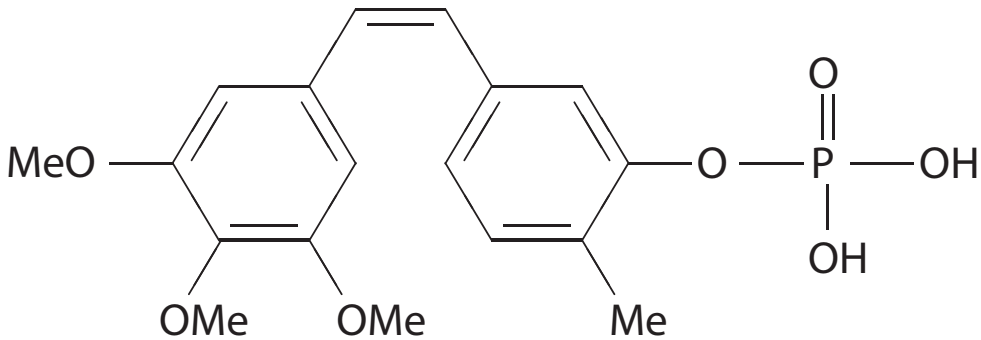


Figure 5.1: Chemical structure of the tubulin-binding agent Ang-510.

Materials & methods

Chemicals & reagents

Culture medium was α -MEM from Gibco BRL, Breda, The Netherlands, supplemented with 10% fetal calf serum (FCS) and penicillin/streptomycin. rhVEGF-A was from Oncogene, Sanbio, Uden, The Netherlands. ER-MP12 directed against murine PECAM-1 (CD31) was kindly provided by Dr. P. Leenen, Erasmus University, Rotterdam, The Netherlands. The matrix metalloproteinase (MMP)-inhibitor marimastat was kindly provided by Chiroscience Inc. (Cambridge, United Kingdom). TNP-470, a kind gift from W. Landuyt, University Hospital, K.U. Leuven, Belgium. The newly developed tubulin-binding agent Ang-510 was a kind gift from Graeme J. Dougherty and Peter D. Davis, Angiogene Pharmaceuticals Ltd. (United Kingdom).

In vitro vascularization models

In vitro angiogenesis was measured as outgrowth of endothelial capillary structures from cultures of 17-day-old fetal mouse metatarsal bone explants, as described previously.²³ In short, isolated metatarsals were cultured for 48h in 24-well plates in 125 μ l α -MEM medium to allow for attachment to bottom of the culture plate. Subsequently, medium was replaced by 500 μ l fresh medium containing vascular endothelial growth factor (VEGF) (50ng/ml) and the test substances and the medium was replaced every 3-4 days. After a total of 10 days of culture, the explants were fixed and stained for PECAM-1.

In the pre-culture experiments, the explants were treated for 24h with the test substances, after attachment to the bottom of the plate, and were subsequently cultured for another 10 days in the presence of VEGF (50ng/ml).

The area of PECAM-1-positive tubular structures was determined by image anal-

ysis using Image Pro Plus 3.0 for Windows 95/NT (Media Cybernetics, Carlsbad, CA). Images were obtained using a digital camera with a fixed window of 768×576 pixels. Data are depicted as number of pixels per area.

In vitro effects on newly established vasculature were examined in fetal mouse bone explant cultures that were first cultured for 10 days in the presence of VEGF (50ng/ml) to stimulate capillary network formation. Subsequently, the medium was replaced with 500 μ l fresh medium containing the test substances and were cultured for another 24h after which they were fixed and stained for PECAM-1 and further analyzed as described above. After obtaining images for the quantification of PECAM-1 positive structures, the cultures were counterstained with Mayer's hematoxylin (H) for 30 seconds and eosin (1% in 96% ethanol) (E) for 90 seconds.

Statistics. Results are depicted as mean value standard error of the mean (SEM). Differences between groups were determined by one-way analysis of variance for multiple comparisons followed by Fisher's LSD test.

Results

Effects on angiogenesis

Figure 5.2a shows dose-inhibition curves of the effects of marimastat, TNP-470 and Ang-510 on VEGF (50ng/ml) stimulated PECAM-1 positive capillary outgrowth from 17-day-old fetal mouse metatarsal bone organ cultures. VEGF-stimulated outgrowth was significantly and dose-dependently suppressed by marimastat, TNP-470 and Ang-510 with IC_{50} values of approximately 0.6, 0.6 and 0.06 μ M, respectively. The effects of these agents on endothelial outgrowth are further illustrated in Figure 5.2b-d. Figure 5.2b shows a large PECAM-1 positive endothelial network that has been formed after 10 days stimulation with VEGF. Figure 5.2c and d show VEGF-stimulated cultures in the presence of 1 μ M TNP-470 and 1 μ M Ang-510, respectively. Both compounds inhibited the outgrowth of a capillary network, with Ang-510 being more potent than TNP-470. Explants cultured with 1 μ M marimastat showed inhibition of vascular outgrowth, similar to those treated with TNP-470 (not shown).

In order to study the effect of the three agents in our anti-angiogenic model in more detail, we examined the effect of pre-treatment with these agents on subsequent VEGF-stimulated vascular outgrowth. At time of explantation, PECAM-1 positive endothelial precursor cells are located in the perichondrium of the explants, as previously shown.²³ From these precursor cells the capillary structures sprout and form the vascular network. To target these precursor cells, directly after adhesion to the culture plate, the fetal bone explants were pre-treated for 24 h with the different anti-vascular compounds and were then subsequently cultured for 10 days in the presence of VEGF. As shown in Figure 5.3, pre-treatment with marimastat did not affect VEGF-stimulated capillary outgrowth, while both TNP-470 and Ang-510 significantly suppressed subsequent VEGF-stimulated outgrowth with IC_{50} values of approximately 0.7 and 0.08 μ M, respectively.

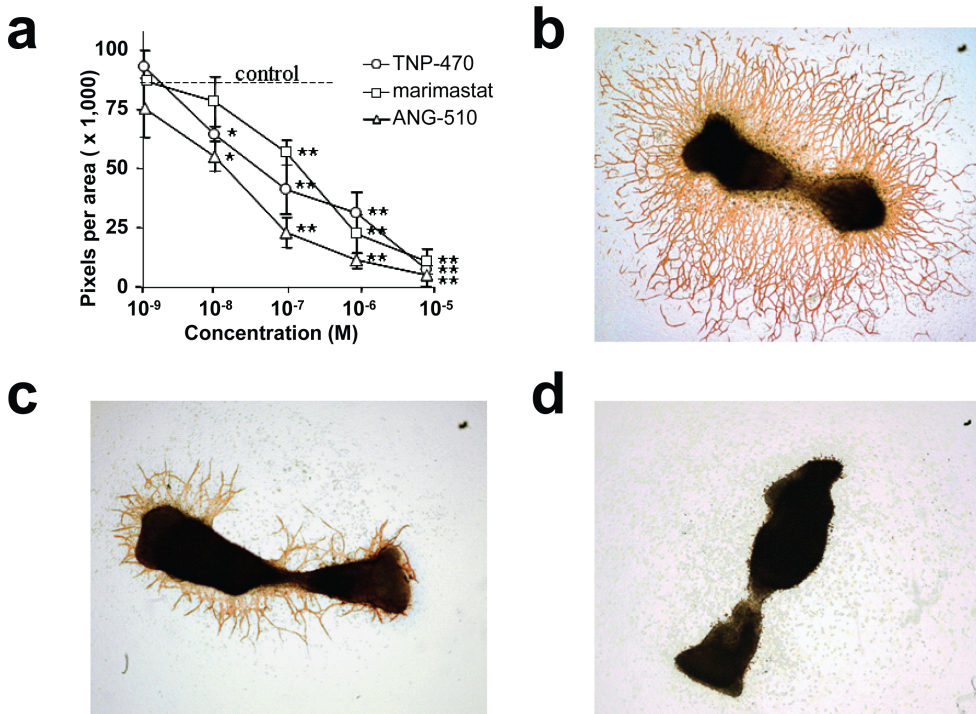


Figure 5.2: Effects on angiogenesis. (a) 17-day-old fetal mouse bone explants were stimulated for 10 days with VEGF (50ng/ml) in the absence or presence of different concentrations marimastat, TNP-470 or Ang-510 ($n = 6$). Quantification of the number of PECAM-1 positive pixels per area is given as mean \pm SEM ($*p < 0.05$; $**p < 0.01$ compared to controls). (b-d) Endothelial outgrowth after stimulation with VEGF (b) and after stimulation with VEGF together with TNP-470 (1 μ M) (c) and together with Ang-510 (1 μ M) (d).

Effects on newly established vasculature

To study the effects of the three compounds on newly established capillaries, first endothelial outgrowth was stimulated with VEGF (50ng/ml) for 10 days and subsequently the cultures were treated for 24h with the different anti-vascular agents. As shown in Figure 5.4a, marimastat and TNP-470 did not affect the VEGF-stimulated newly formed vasculature while Ang-510 showed a significant suppression of newly established vasculature with an IC_{50} of around 0.01 μ M.

Figure 5.4b shows control capillary outgrowth after 10 days stimulation with VEGF, stained for PECAM-1 and counter stained with HE. Figure 5.4c and d depicts newly formed vasculature after subsequent 24h treatment with TNP-470 (10 μ M) and Ang-510 (1 μ M). As shown, TNP-470 did not affect the established capillary network, similar results were obtained with marimastat (10 μ M) (not shown). In contrast, 24h treatment with Ang-510 caused a significant disintegration of the newly established capillary structures, with only fragments of the original network remaining. Histo-

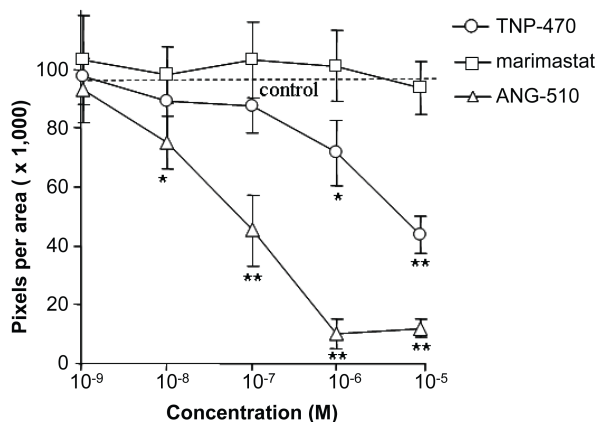


Figure 5.3: Effects of pre-treatment on vascular outgrowth. 17-day-old fetal mouse bone explants were, directly after adhesion to the culture plate, cultured for 24h with different concentrations of marimastat, TNP-470 or Ang-510 and subsequently stimulated for another 10 days with VEGF (50ng/ml) ($n = 6$). Quantification of the number of PECAM-1 positive pixels per area is given as mean \pm SEM (* $p < 0.05$; ** $p < 0.01$ compared to controls).

logical HE staining revealed that this degenerative effect was specific for the capillary network, as the layer of fibroblastic cells, originating from the periosteum on which the capillary network grows and expands,²³ remained morphologically fully intact.

Discussion

In this study, we developed an *in vitro* model that can distinguish between effects of compounds on angiogenesis and on newly established vasculature. We examined the effects of three anti-vascular agents, among which the recently developed tubulin-binding agent Ang-510. We showed that this compound effectively interfered with both angiogenesis as well as newly established vasculature, whereas the synthetic fumagillin derivate TNP-470 and the MMP-inhibitor marimastat selectively affected angiogenesis alone.

Angiogenesis is the process of generating new blood vessels from pre-existing vasculature, which is indispensable for solid tumor growth and metastasis. As such, targeting tumor angiogenesis, in anti-cancer therapy, is an intense field of interest. Current investigations towards the development of agents that inhibit tumor vascularization, however, not only focus on interference with the process of angiogenesis, but also on intervention with already established tumor vasculature.^{3,4} Compounds that belong to this group are called VDAs; agents that selectively target tumor vasculature on basis of structural and functional abnormalities of these vessels.⁷⁻⁹ In the development of new and more effective anti-vascular agents, it is of importance to have model systems available that can give accurate information about their mode

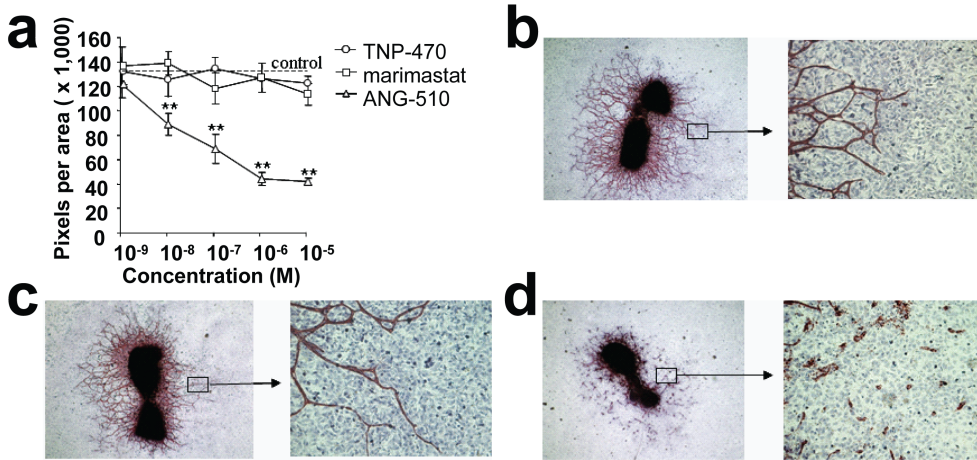


Figure 5.4: Effects on newly established vasculature. (a) 17-day-old fetal mouse bone explants were stimulated for 10 days with VEGF (50ng/ml) followed by 24h treatment with different concentrations marimastat, TNP-470 or Ang-510 ($n = 6$). Quantification of the number of PECAM-1 positive pixels per area is given as mean \pm SEM ($*p < 0.05$; $**p < 0.01$ compared to controls). After culture, bone explant capillary outgrowth was visualized by staining for PECAM-1 in combination with HE. (b-d) The combined PECAM-1 and HE staining are shown for explants stimulated for 10 days with VEGF without subsequent treatment (control) (b), and for explants stimulated with VEGF with subsequent 24h treatment with TNP-470 (10 μ M) (c) or Ang-510 (1 μ M) (d).

of action and vascular targets involved and thus can differentiate between effects on angiogenesis or newly established vasculature. For this, we adapted our previously developed angiogenesis assay consisting of the outgrowth of capillaries from cultured fetal mouse metatarsals and suited it to study effects on established vasculature as well.²³ To validate this *in vitro* model, we examined the effects of three different compounds in several experimental settings.

We examined the anti-angiogenic actions of two well-known inhibitors of angiogenesis, marimastat and TNP-470, respectively, and that of the newly developed tubulin-binding agent Ang-510. In previous studies, it has been shown that both the synthetic MMP-inhibitor marimastat, as well as the synthetic fumagillin derivate TNP-470 possess strong anti-angiogenic properties in various *in vitro* models by interfering with endothelial cell invasion and proliferation.²⁴⁻²⁸ In concordance with these observations, in our model, marimastat and TNP-470 potently and dose dependently inhibited angiogenesis, indicated by suppressed outgrowth of PECAM-1 positive capillaries. Moreover, the newly developed tubulin-binding agent Ang-510 also showed strong anti-angiogenic properties in our model system.

Previously, we have shown that PECAM-1 positive endothelial precursor cells are present in the perichondrium of the bone explants, before the outgrowth of vasculature.²³ In order to determine whether the observed anti-angiogenic effects might involve a direct action on these early-stage endothelial precursor cells from which

the capillaries are formed, we pre-incubated the bone explants with the different agents for 24h and subsequently cultured them for 10 days in the presence of VEGF. After pre-treatment of the bone explants with marimastat, at doses that actively suppressed angiogenesis, there was no effect on the subsequent outgrowth of vasculature. Recent studies have shown that MMP-inhibitors such as marimastat inhibit angiogenesis by blocking the invasion and migration of endothelial cells into the extracellular matrix,^{24,29,30} which might explain why in our model, marimastat does not have a direct effect on endothelial precursors and their subsequent vascular outgrowth after pre-treatment, but strongly inhibits angiogenesis when it is continuously present. In line with this, it was previously shown that in a three-dimensional rat aortic model, marimastat potently inhibited angiogenesis, without affecting the proliferation of rat aortic endothelial cells in monolayer cultures.²⁴

In contrast to marimastat, TNP-470, and even more potently Ang-510, inhibited vascular outgrowth after 24h pre-treatment of the bone explants. TNP-470 is a known angiogenesis inhibitor, which has been shown to induce a cell cycle arrest in the G1-phase, resulting in inhibition of endothelial cell proliferation and network formation, indicating that this compound acts via a cytostatic rather than a cytotoxic mode of action.²⁵⁻²⁸ However, in our model, at higher concentrations, inhibition of outgrowth of vasculature by TNP-470 was not reversible after stimulation with VEGF, suggesting that, at these doses, the mode of action is cytotoxic and not cytostatic. Interestingly, a similar dual mode of action of TNP-470 has been described on the *in vitro* growth of human umbilical vein endothelial cells (HUVECs), showing cytostatic inhibition at lower doses and a cytotoxic suppression at higher doses.³¹ Furthermore, we found that Ang-510 strongly inhibited the outgrowth of capillaries after pre-treatment of the bone explants, suggesting that this agent possess an irreversible cytotoxic mode of action on endothelial precursor cells. This observation is in line with findings of Ahmed *et al.* and Iyer *et al.* who showed that the combretastatin analog A4 phosphate (CA4P) was cytotoxic to proliferating HUVECs.^{6,32}

Finally, we studied the effects of the three compounds on newly established vasculature. In contrast to their actions on angiogenesis, marimastat and TNP-470 did not affect newly established capillaries. *In vitro* studies exploring the effects on established vasculature are very rare, however, in one study, using cultures of rat aorta, marimastat showed to stabilize rather than to inhibit existing microvessels and to prevent their regression, resulting in the prolonged survival of microvascular networks.³³ To date, no studies on the effects of TNP-470 on established vasculature have been published. However, our observations, that this agent has no effect on established vasculature may be perceivable, since TNP-470 has been shown to act on endothelial cells via a cytostatic action through suppression of the cell cycle.²⁸ Furthermore, as expected, next to its strong inhibitory effects on angiogenesis and capillary outgrowth after pre-treatment of bone explants, Ang-510 showed to have a marked disintegrative effect on newly established vasculature. This damaging effect of Ang-510 was most likely specific for endothelial cells, as concomitant HE staining revealed that the underlying layer of fibroblastic cells remained unaffected. In line

with our findings, the VDA CA4P showed *in vitro* and *in vivo* rapid disruption of the tubulin cytoskeleton and changes in the three-dimensional shape of proliferating endothelial cells.^{34–36}

In conclusion, the current search for more specific and more active VDAs is hampered by a lack of *in vitro* models that can accurately distinguish between effects on angiogenesis and on established vasculature, urging the need for models which can specifically differentiate between the two. The overlap in action of VDAs on angiogenesis and on newly established vasculature illustrates the usefulness of this *in vitro* model, which is able to differentially recognize effects on both vascular targets. This *in vitro* model provides an efficient and rapid way to screen for biological activity of anti-vascular compounds, which could prove of great benefit in the field of vascular research. Moreover, the ability to make a clear distinction between different vascular targets may facilitate the identification of pharmacological compounds with potential clinical benefit. The indicated differences between marimastat, TNP-470 and Ang-510 in targeting vascular networks are illustrative for this approach.

Acknowledgments

This study was supported by The Netherlands Organization of Scientific Research-Medical Sciences (Grant No. PGN 902-17-090) (JW, VWMH and CL), by the Dutch Cancer Foundation Koningin Wilhelmina Fonds (Grant No. RUL2000-2196) (EB and CL) and (Grant No. UL2007-3801) (CL and EK).

References

1. Folkman J. Angiogenesis in cancer, vascular, rheumatoid and other disease. *Nat Med*, 1995 Jan;1(1):27–31.
2. Hanahan D and Folkman J. Patterns and emerging mechanisms of the angiogenic switch during tumorigenesis. *Cell*, 1996 Aug;86(3):353–64.
3. Denekamp J. Review article: angiogenesis, neovascular proliferation and vascular pathophysiology as targets for cancer therapy. *Br J Radiol*, 1993 Mar;66(783):181–96.
4. Folkman J. Seminars in medicine of the beth israel hospital, boston. clinical applications of research on angiogenesis. *N Engl J Med*, 1995 Dec;333(26):1757–63.
5. Ellis LM, Liu W, Ahmad SA, Fan F, Jung YD, Shaheen RM, and Reinmuth N. Overview of angiogenesis: Biologic implications for antiangiogenic therapy. *Semin Oncol*, 2001 Oct;28(5 Suppl 16):94–104.
6. Siemann DW, Warrington KH, and Horsman MR. Targeting tumor blood vessels: an adjuvant strategy for radiation therapy. *Radiother Oncol*, 2000 Oct;57(1):5–12.
7. Chaplin DJ and Dougherty GJ. Tumour vasculature as a target for cancer therapy. *Br J Cancer*, 1999 Jul;80 Suppl 1:57–64.
8. Denekamp J. Vascular attack as a therapeutic strategy for cancer. *Cancer Metastasis Rev*, 1990 Nov;9(3):267–82.
9. Siemann D. Vascular targeting agents. *Horizons in Cancer Therapeutics*, 2002;3:4–15.
10. Gaya AM and Rustin GJS. Vascular disrupting agents: a new class of drug in cancer therapy. *Clin Oncol (R Coll Radiol)*, 2005 Jun;17(4):277–90.
11. Tozer GM, Kanthou C, and Baguley BC. Disrupting tumour blood vessels. *Nat Rev Cancer*, 2005 Jun;5(6):423–35.
12. Pilat MJ and Lorusso PM. Vascular disrupting agents. *J Cell Biochem*, 2006 Nov; 99(4):1021–39.
13. Siemann DW, Chaplin DJ, and Horsman MR. Vascular-targeting therapies for treatment of malignant disease. *Cancer*, 2004 Jun;100(12):2491–9.
14. Thorpe PE. Vascular targeting agents as cancer therapeutics. *Clin Cancer Res*, 2004 Jan;10(2):415–27.
15. Cai SX. Small molecule vascular disrupting agents: potential new drugs for cancer treatment. *Recent Pat Anticancer Drug Discov*, 2007 Jan;2(1):79–101.
16. Chaplin DJ, Horsman MR, and Siemann DW. Current development status of small-molecule vascular disrupting agents. *Curr Opin Investig Drugs*, 2006 Jun;7(6):522–8.
17. Hinnen P and Eskens FALM. Vascular disrupting agents in clinical development. *Br J Cancer*, 2007 Apr;96(8):1159–65.

18. Patterson DM and Rustin GJS. Vascular damaging agents. *Clin Oncol (R Coll Radiol)*, 2007 Aug;19(6):443–56.
19. Tozer GM, Kanthou C, Lewis G, Prise VE, Vojnovic B, and Hill SA. Tumour vascular disrupting agents: combating treatment resistance. *Br J Radiol*, 2008 Oct;81 Spec No 1:S12–20.
20. Siemann DW and Shi W. Efficacy of combined antiangiogenic and vascular disrupting agents in treatment of solid tumors. *Int J Radiat Oncol Biol Phys*, 2004 Nov;60(4):1233–40.
21. Siemann DW and Shi W. Dual targeting of tumor vasculature: combining avastin and vascular disrupting agents (ca4p or oxi4503). *Anticancer Res*, 2008;28(4B):2027–31.
22. Siemann DW and Horsman MR. Vascular targeted therapies in oncology. *Cell Tissue Res*, 2009 Jan;335(1):241–8.
23. Deckers M, van der Pluijm G, Dooijewaard S, Kroon M, van Hinsbergh V, Papapoulos S, and Löwik C. Effect of angiogenic and antiangiogenic compounds on the outgrowth of capillary structures from fetal mouse bone explants. *Lab Invest*, 2001 Jan;81(1):5–15.
24. Burbridge MF, Cogé F, Galizzi JP, Boutin JA, West DC, and Tucker GC. The role of the matrix metalloproteinases during in vitro vessel formation. *Angiogenesis*, 2002; 5(3):215–26.
25. Friis T, Hansen AB, Houen G, and Engel AM. Influence of angiogenesis inhibitors on endothelial cell morphology in vitro. *APMIS*, 2006 Mar;114(3):211–24.
26. Lien WH, Chen CK, Lai LY, Chen YH, Wu MP, and Wu LW. Participation of cyclin d1 deregulation in tnp-470-mediated cytostatic effect: involvement of senescence. *Biochem Pharmacol*, 2004 Aug;68(4):729–38.
27. Yeh JR, Mohan R, and Crews CM. The antiangiogenic agent tnp-470 requires p53 and p21cip/waf for endothelial cell growth arrest. *Proc Natl Acad Sci U S A*, 2000 Nov; 97(23):12782–7.
28. Zhang Y, Griffith EC, Sage J, Jacks T, and Liu JO. Cell cycle inhibition by the anti-angiogenic agent tnp-470 is mediated by p53 and p21waf1/cip1. *Proc Natl Acad Sci U S A*, 2000 Jun;97(12):6427–32.
29. Rundhaug JE. Matrix metalloproteinases and angiogenesis. *J Cell Mol Med*, 2005; 9(2):267–85.
30. Taraboletti G, Garofalo A, Belotti D, Drudis T, Borsotti P, Scanziani E, Brown PD, and Giavazzi R. Inhibition of angiogenesis and murine hemangioma growth by batimastat, a synthetic inhibitor of matrix metalloproteinases. *J Natl Cancer Inst*, 1995 Feb; 87(4):293–8.
31. Kusaka M, Sudo K, Matsutani E, Kozai Y, Marui S, Fujita T, Ingber D, and Folkman J. Cytostatic inhibition of endothelial cell growth by the angiogenesis inhibitor tnp-470 (agm-1470). *Br J Cancer*, 1994 Feb;69(2):212–6.

32. Iyer S, Chaplin DJ, Rosenthal DS, Boulares AH, Li LY, and Smulson ME. Induction of apoptosis in proliferating human endothelial cells by the tumor-specific antiangiogenesis agent combretastatin a-4. *Cancer Res*, 1998 Oct;58(20):4510-4.
33. Zhu WH, Guo X, Villaschi S, and Francesco Nicosia R. Regulation of vascular growth and regression by matrix metalloproteinases in the rat aorta model of angiogenesis. *Lab Invest*, 2000 Apr;80(4):545-55.
34. Chaplin DJ, Pettit GR, and Hill SA. Anti-vascular approaches to solid tumour therapy: evaluation of combretastatin a4 phosphate. *Anticancer Res*, 1999;19(1A):189-95.
35. Galbraith SM, Chaplin DJ, Lee F, Stratford MR, Locke RJ, Vojnovic B, and Tozer GM. Effects of combretastatin a4 phosphate on endothelial cell morphology in vitro and relationship to tumour vascular targeting activity in vivo. *Anticancer Res*, 2001; 21(1A):93-102.
36. Grosios K, Holwell SE, McGown AT, Pettit GR, and Bibby MC. In vivo and in vitro evaluation of combretastatin a-4 and its sodium phosphate prodrug. *Br J Cancer*, 1999 Dec;81(8):1318-27.

6

2-Methoxyestradiol Analogue ENMD-1198 Reduces Breast Cancer Induced Osteolysis and Tumor Burden both *In Vitro* and *In Vivo*

Thomas J.A. Snoeks¹
Isabel M. Mol¹
Ivo Que¹
Eric L. Kaijzel¹
Clemens W.G.M. Löwik¹

Mol Cancer Ther. 2011 May;10(5):874–82

¹Dept. of Endocrinology, LUMC, Leiden, The Netherlands

Abstract

It has been estimated that 70% of advanced breast cancer patients will face the complication of bone metastases. Three processes are pivotal during bone metastatic growth of breast cancer, namely, tumor cell proliferation, angiogenesis, and osteolysis. During tumor-induced osteolysis, a number of cytokines and growth factors are released from the degraded bone matrix. These factors stimulate further tumor growth, tumor angiogenesis, and tumor-induced osteolysis. New therapies should target all relevant processes to halt this powerful feedback loop. Here, we characterized the new 2-methoxyestradiol analogue ENMD-1198 and showed that it is cytotoxic to tumor cells. Moreover, ENMD-1198 showed both anti-angiogenic and vascular disruptive properties and was capable of protecting the bone against tumor-induced osteolysis. We confirmed the *in vitro* data with a series of *in vivo* experiments showing the beneficial effects of ENMD-1198 and ENMD-1198 based combination treatments of metastatic breast cancer in bone both on tumor progression and on survival with long-term ENMD-1198 treatment. We confirmed the *in vivo* relevance of the ENMD-1198 protective effect on bone both with X-ray radiographs and micro-computed tomography. In addition, we combined ENMD-1198 treatment with low-dose metronomic cyclophosphamide and the bisphosphonate risedronic acid, leading to a mild increase in treatment efficacy.

Introduction

The preference of breast cancer to metastasize to bone followed by growth and bone destruction involves specific tumor-host interactions. It has been estimated that 70% of advanced breast cancer patients will face complications of bone metastases, which includes osteolytic lesions resulting in severe bone pain, fracture, hypercalcemia, and nerve compression.¹⁻³

Several processes are crucial during bone metastatic growth. These processes include tumor growth and tumor-stroma interactions such as local pro-angiogenic signaling, local activation of the innate immune system, and local suppression of the adaptive immune system.³⁻⁶ Regulatory T (T_{reg}) cells are capable of blocking local immune responses. A local increase in T_{reg} cells is a major factor in the tolerance and immune avoidance of tumors.⁷ Pro-angiogenic signaling and the local alterations of the immune system both have a positive feedback on tumor growth.

In addition, breast cancer cells are capable of releasing parathyroid hormone-related protein (PTHrP), which activates receptor activator for nuclear factor κ B ligand (RANKL) on stromal cells and osteoblasts. RANK-RANKL signaling not only leads to an increase in osteoclastogenesis but also prolongs the lifetime of osteoclasts, resulting in increased bone resorption. During bone resorption, several growth factors and cytokines are released from the bone matrix. These include transforming growth factor- β (TGF- β), insulin like growth factors (IGFs), fibroblast growth factors (FGF-1 and -2), platelet derived growth factor (PDGF) and bone morphogenic proteins (BMPs). The released growth factors stimulate tumor cell proliferation and survival. TGF- β induces the upregulation in vascular endothelial growth factor (VEGF) expression by tumor cells leading to an increase in tumor angiogenesis.⁸ Moreover, TGF- β stimulates the production and release of PTHrP by the tumor cells resulting in a self-sustaining feedback loop known as the vicious cycle of bone metastases.⁹⁻¹²

Because of the complex nature of bone metastasis, new treatments should simultaneously target tumor cell proliferation, angiogenesis, immunologic alterations, and halt the cycle of bone metastases. In this study we describe the *in vitro* and *in vivo* efficacy of a combination therapy targeting these major processes involved in metastatic growth in bone. To do so, we combined low dose "metronomic" cyclophosphamide (CTX), 2-methoxyestradiol (2ME2, Panzem) derivative ENMD-1198 and the bisphosphonate risedronic acid.

Previous research indicated that the therapeutic effect of metronomic chemotherapy is mainly due to a reduction of tumor angiogenesis rather than direct cytotoxicity.^{13,14} In addition, metronomic CTX selectively depletes T_{reg} cells resulting in an enhanced tumor immune response.^{15,16}

The naturally occurring estrogen metabolite 2ME2 (Figure 6.1) has been shown to have anti-tumor, anti-angiogenic and anti-resorptive effects.^{17,18} *In vivo* therapeutic effects of 2ME2 are moderate because of the rapid inactivation via conjugation (positions 3 and 17) and oxidation (position 17). ENMD-1198 is a 2ME2 derivative

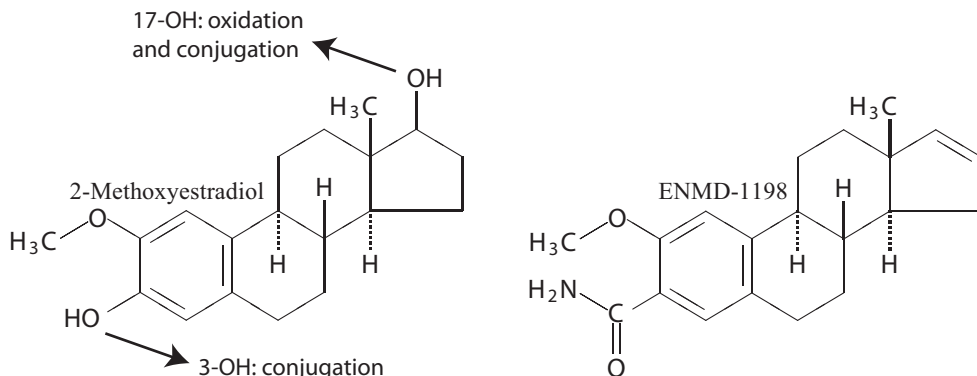


Figure 6.1: 2ME2 and ENMD-1198 structures. (a) Structural formula of the estrogen metabolite 2-methoxyestradiol (2ME2). Rapid inactivation of 2ME2 occurs *in vivo* via oxidation (at position 17) or conjugation (positions 3 & 17). (b) The 2ME2 derivate ENMD-1198 has been altered at positions 3 and 17 resulting in slower inactivation and increased plasma levels of the active compound *in vivo*. Both compounds have very low affinity for the estrogen receptor.

with reduced metabolic liabilities (Figure 6.1b).¹⁹ It displays anti-proliferative effects on tumor cells and neo-angiogenesis very similar to 2ME2. ENMD-1198 inhibits pro-angiogenic signaling through downregulating hypoxia-inducible factor 1 α (HIF-1 α) and STAT3 and it has vascular disruptive effects.^{20–22} To date, no studies on treatment of bone metastases or bone specific effects with ENMD-1198 have been published. ENMD-1198 is currently in clinical trial for treatment of primary breast cancer.²³

Bisphosphonate treatment blocks osteoclast function, thereby halting the cycle of bone metastatic growth.^{24–26} It has been shown *in vivo* that bisphosphonate treatment mainly prevents the development of new metastases while exhibiting a transient effect on already established metastases.²⁷ Also, bisphosphonates reduce skeletal complications and morbidity in patients with bone metastases.²⁸

The combination treatment of metronomic CTX, bisphosphonates, and ENMD-1198 targets all of the aforementioned major processes involved in osteolytic bone metastasis of breast cancer, namely, tumor cell proliferation, angiogenesis, local immune suppression, and osteolysis. By targeting the tumor stroma, in addition to the cancerous cells, less drug resistance is to be expected over time. The aim of this study was to assess the efficacy of ENMD-1198 treatment on tumor growth and bone destruction in a murine model for osteolytic breast cancer metastases and to evaluate a possible synergy between ENMD-1198, metronomic CTX, and bisphosphonates.

Materials and Methods

Animals

Pregnant Swiss albino and female athymic mice (BALB/c nu/nu, 46 weeks old) mice were acquired from Charles River Laboratories, housed in individually ventilated cages, and food and water were provided *ad libitum*. All surgical and analytic procedures were done under isoflurane gas anesthesia. Tumor diameters in the animals were measured routinely. Animals were sacrificed by cervical dislocation at the end of the experimental period or when the tumor diameter exceeded 1cm in concordance with local guidelines for the use of animals in cancer research. Animal experiments were approved by the local committee for animal health, ethics, and research of Leiden University Medical Center.

Cell lines and culture conditions

The cell lines MDA-231-B/Luc+ (hereafter MDA-BO2), a bone-seeking and luciferase-expressing subclone from the human breast cancer MDA-MB-231^{29,30} cell line, and RAW264.7, a murine osteoclast precursor cell line (American Type Culture Collection), were cultured in DMEM (Invitrogen) containing 4.5g glucose/l supplemented with 10% fetal calf serum (FCS; Lonza), 100 units/ml penicillin, 50µg/ml streptomycin (Invitrogen), and 800µg/ml geneticin/G418 (Invitrogen).

Both cell lines were grown in a humidified incubator at 37°C and 5% CO₂. All cell lines were monthly checked for Mycoplasma infection by PCR. Cells were checked routinely for morphologic changes, and no other authentication tests were done on these cell lines because they were acquired in the laboratory.

In vitro viability assays

Both MDA-BO2 and RAW264.7 were plated in a 96-well plate (Costar) in 100µl medium at a density of 10,000 cells per well and left over night to adhere. The next day the medium was replaced with medium containing the experimental compounds, 6 wells per condition. After 24, 48, or 144 hours, cell viability was measured using a nonradioactive colorimetric MTS viability assay (Promega Benelux) according to the manufacturer's protocol. Optical absorption was measured at 490nm with a Versamax absorbance microplate reader (Molecular Devices).

In vitro vascularization models

In vitro angiogenesis was measured as outgrowth of endothelial capillary structures from cultures of 17-day old fetal mouse metatarsal bone explants, as described previously.³¹ In short, pregnant Swiss albino mice were sacrificed by cervical dislocation at day 17 of gestation and isolated fetal metatarsals were cultured in α -MEM medium containing 10% FCS (Lonza), penicillin (100units/ml), and streptomycin (50µg/ml);

Invitrogen) and left for 48 hours to adhere. Thereafter, the feed was replaced with medium containing VEGF (50ng/ml; rhVEGF-A; Oncogene Science). After 10 days of culture, the explants were fixed and stained with ER-MP12 antibody directed against murine PECAM-1 (CD31; kind gift of Dr. P. Leenen, Erasmus University, Rotterdam, the Netherlands).

Images were obtained using a digital camera and the area of PECAM-1-positive tubular structures was quantified by image analysis using ImageJ 1.43r (Wayne Rasband, National Institute of Health, USA).

In vitro effects on newly established vasculature were examined as described previously.³² In short, isolated 17-day old fetal metatarsals were left to adhere and cultured for 10 days in the presence of VEGF (50ng/ml) to stimulate capillary network formation. Thereafter, the feed, was replaced by medium containing the test substances. After 24 hours, bone explants were fixed and stained for PECAM-1 for further analysis as described before.

***In vitro* bone resorption assay**

Bone resorption was assessed as described earlier.³³ In short, pregnant Swiss Albino mice were injected with 30 μ Ci ⁴⁵Ca (1Ci/mmol; PerkinElmer, Waltham, MA USA) on day 16 of gestational age. The animals were sacrificed on day 17 and the ⁴⁵Ca pre-labeled fetal metatarsals were isolated and pre-cultured in 1ml of α -MEM (Invitrogen) supplemented with 0.1% BSA in six well plates (Costar) for 24h. This allowed ⁴⁵Ca exchange in the bones with the culture medium. The metatarsals were then cultured in 250 μ l of (α -MEM, 0.1% BSA) in 24-well plates for 10 days in the presence of 100nM PTHrP (1-34) (Bachem, Bubendorf, Switzerland) with or without additives ($n = 6$ per condition). Finally, medium was removed and residual ⁴⁵Ca was extracted from the bones in 5% trichloroacetic acid for 24h. The amount of ⁴⁵Ca in both the culture media and the decalcification fluid was determined by liquid scintillation using a β -counter (Packard 1600 TR, Groningen, The Netherlands). Resorption was expressed as percentage of ⁴⁵Ca from the pre-labeled explants that is released in the medium during culture (⁴⁵Ca release (%) = $\frac{^{45}\text{Ca in medium (cpm)}}{\text{total } ^{45}\text{Ca (cpm)}} \cdot 100\%$).

***In vivo* treatment of bone metastases**

MDA-BO2 cells were injected into the right tibiae as described previously.³⁰ In brief, 2 holes were drilled through the bone cortex of the upper right tibia with a 25-gauge needle (25G 5/8; BD Micro-Fine) and bone marrow was flushed out. Subsequently, 250,000 MDA-BO2 cells/10 μ l PBS was injected into the right tibiae of 6-week-old nude mice. Three days after intra-osseous inoculation of MDA-BO2 cells, the animals were randomly divided in groups ($n = 10$).

In a first experiment, 4 groups of mice ($n = 10$) received either ENMD-1198 (200mg/kg/day, per oral gavage) or CTX (30mg/kg/day, through the drinking water as described previously³⁰) or a combination of ENMD-1198 and CTX or vehicle

control. Treatment started at day 7 after inoculation and was continued throughout the experiment. After 6 weeks the animals were sacrificed by cervical dislocation hind-limbs were fixed and kept for *ex vivo* X-ray analysis.

In a second experiment, 4 groups of mice ($n = 10$) received ENMD-1198 (200mg/kg/day, per oral gavage) or ENMD-1198 + CTX (30mg/kg/day, through the drinking water) or ENMD-1198 + CTX + Risedronic Acid (Procter & Gamble Pharmaceuticals, Norwich, NY USA) (1.6mol/kg/day, by sub cutaneous injection).

Bioluminescence Imaging

The progression of cancer cell growth was monitored weekly by bioluminescence imaging (BLI) using the IVIS100 Imaging System (Caliper Life Sciences, Hopkinton, MA USA).

X-ray radiographs and CT analysis

At the experimental endpoints, mice were sacrificed and the tumor bearing hindlimbs were removed and assessed for osteolytic lesions by using a Faxitron 43805 (Hewlett Packard). X-ray radiographs were scanned and subsequently analyzed using Adobe Photoshop (Adobe Systems, San Jose, CA, USA).

Micro-computed tomographic (μ CT) scans were made using a SkyScan 1076 CT scanner (SkyScan, Kontich, Belgium) using a source voltage set to 40kV and a source current set to 250 μ A, with a step size of 0.9° over a trajectory of 180°. Images were taken with a frame average of 3 to reduce noise and an image pixel size of 9.03 μ m. Reconstructions were made using nRecon software (SkyScan) with a beam hardening correction set to 20% and a ring artifact correction set to 5. Volume measurements and visualizations were performed using MeVisLab (MeVis Medical Solutions AG, Bremen, Germany).

Statistics

Results are depicted as mean value \pm standard error of the mean (SEM). Differences between groups were determined by one-way analysis of variance for multiple comparisons followed by student's t-test for differences between two specific groups.

Results

ENMD-1198 reduces MDA-BO2 cell viability *in vitro*

The direct effect of the proposed treatment on tumor cells was assessed *in vitro*. In order to do this, the effect of ENMD-1198 on cell viability was investigated using an MTS colorimetric cell viability assay and with drug concentrations ranging from 0.1 μ M to 3.2 μ M. The MTS assay was performed after 48 hours exposure to

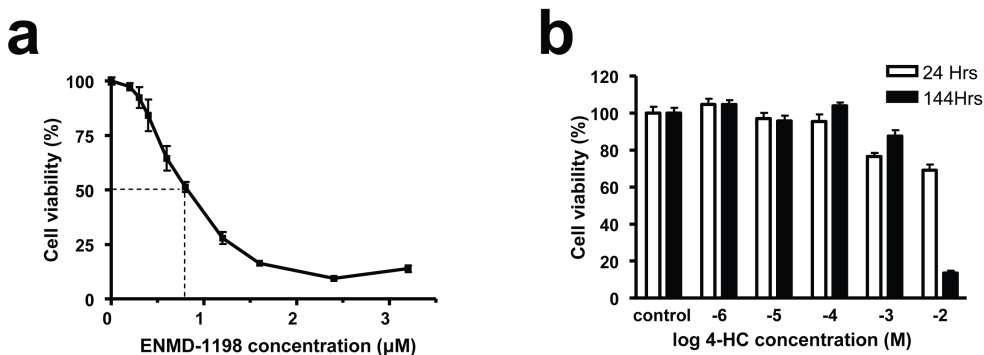


Figure 6.2: ENMD-1198 treatment reduces viability of MDA-BO2 cells *in vitro*, low dose cyclophosphamide does not. (a) ENMD-1198 is reduces MDA-BO2 cell viability. Cell viability was measured after 48 hours of ENMD-1198 treatment. (b) Low doses of 4-hydroperoxycyclophosphamide (4-HC) do not reduce MDA-BO2 cell viability. Cell viability was measured after 24 hours (direct effect) and 144 hours (prolonged metronomic treatment effect) of 4-HC treatment. 4-HC is the main active metabolite of cyclophosphamide.

ENMD-1198. ENMD-1198 inhibited MDA-BO2 cancer cell viability with an IC_{50} of approximately $0.8\mu M$ (Figure 6.2a).

The effect of CTX on cell viability was investigated using an MTS colorimetric cell viability assay and with drug concentrations of the active CTX metabolite Hydroxyperoxycyclophosphamide (4-HC), ranging from $1nM$ to $10\mu M$. The low 4-HC concentrations up to $0.1\mu M$ were similar to concentrations measured *in vivo* during metronomic CTX treatment.³⁴ Cell viability was measured after both 24 and 144 hours exposure to 4-HC to assess the effects of direct treatment and prolonged exposure, respectively. Neither short or long term effects of 4-HC treatment could be observed using drug concentrations up to $0.1\mu M$ (Figure 6.2b).

ENMD-1198 has both an anti-angiogenic effect as well as a vascular disruptive effect *in vitro*

The vascular effect of ENMD-1198 was assessed *in vitro*. The anti-angiogenic effect of ENMD-1198 treatment was investigated using an *in vitro* fetal metatarsal outgrowth angiogenesis assay. The fetal metatarsal explants contain a multitude of stromal and vascular/endothelial precursor cells. This cellular complexity closely mimics the *in vivo* situation during angiogenesis.³¹ Low concentrations of ENMD-1198 slightly enhanced the vascular outgrowth suggesting a possible biphasic effect of ENMD-1198 on angiogenesis. However, this enhancement was not statistically significant. Higher doses of ENMD-1198 had profound dose dependent effects on VEGF stimulated angiogenesis (Figure 6.3a-b).

Next, the effect of ENMD-1198 treatment on previously established vasculature was assessed using metatarsal explants and an optimized vascular disruption protocol

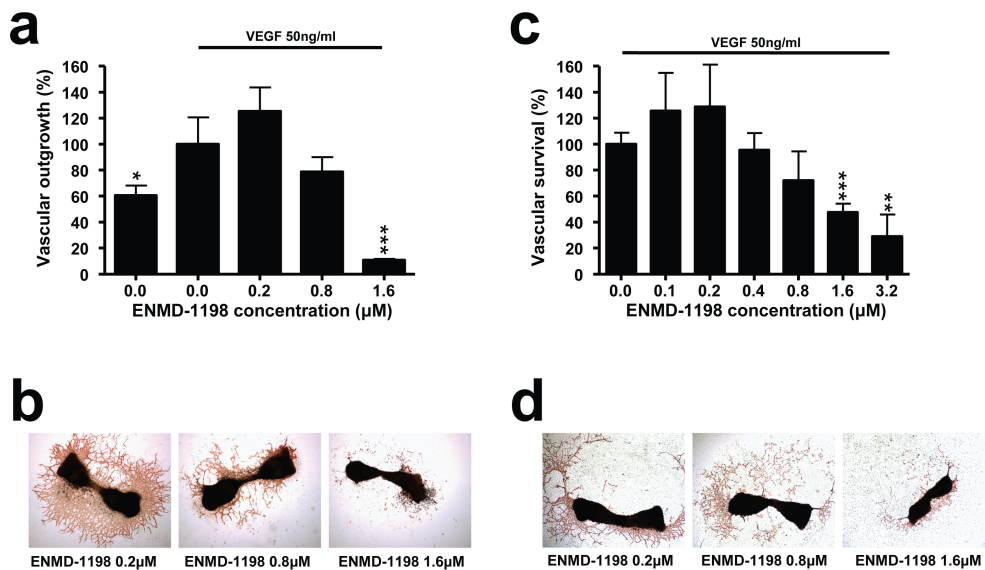


Figure 6.3: ENMD-1198 has both an anti-angiogenic effect as well as a vascular disruptive effect *in vitro*. (a) ENMD-1198 treatment inhibits angiogenesis in a mouse fetal metatarsal explants angiogenesis assay. Metatarsals were cultured for 10 days in the presence of VEGF and ENMD-1198 as indicated in the graph. After CD31 staining, the cultures were photographed and the surface area covered by the vascular outgrowth was quantified using ImageJ. Indicated statistical significant differences are in comparison with the VEGF treated control (* $p < 0.05$; ** $p < 0.001$). All differences in vascular outgrowth between the three ENMD-1198 concentrations are statistically significant. (b) Representative images of the mouse metatarsal angiogenesis assay showing the metatarsal bone surrounded by vascular outgrowth. (c) ENMD-1198 treatment disrupts pre-existing vasculature in a mouse fetal metatarsal explants vascular disruption assay. The fetal explants were treated with ENMD-1198 for 24 hours as depicted in the graph after 10 days of culture in the presence of VEGF (50ng/ml). After CD31 staining, the cultures were photographed and the surface area covered by the vasculature was quantified using ImageJ. Indicated statistical significant differences are in comparison with the untreated control (** $p < 0.01$; *** $p < 0.001$). (d) Representative images of the mouse metatarsal vascular disruption assay. Note the remaining fragments of endothelial structures indicating areas where the vascular network has been disrupted.

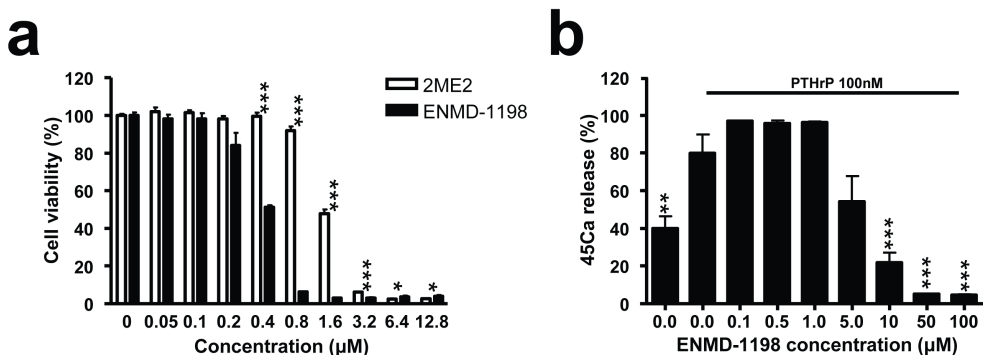


Figure 6.4: ENMD-1198 has anti-resorptive effects *in vitro*. (a) Both 2ME2 and ENMD-1198 reduce the viability of RAW264.7 cells, an osteoclast precursor cell line. ENMD-1198 had an IC_{50} of approximately $0.4\mu M$ and was shown to be four times more potent than 2ME2 ($IC_{50} \sim 1.6\mu M$). Cell viability was measured after 48 hours of 2ME2 or ENMD-1198 treatment. Indicated statistical significant differences are in between 2ME2 and ENMD-1198 ($*p < 0.05$; $**p < 0.001$). (b) ENMD-1198 treatment inhibits bone resorption in a mouse fetal metatarsal explants ^{45}Ca release assay. Radioactive ^{45}Ca -labeled murine fetal metatarsals were culture under the conditions depicted in the graph. The ratio of the amount of ^{45}Ca in the culture medium and the amount of ^{45}Ca in the bone was measured after 10 days of culture. Indicated statistical significant differences are in comparison with the untreated control, stimulated with PTHrP. Although the $5\mu M$ was not significantly different from the untreated control, it was different from the lower treatment concentrations ($p = 0.006$ when compared to $0.1\mu M$) ($*p < 0.01$; $**p < 0.001$).

as previously described.³² Like the metatarsal angiogenesis assay, this assay contains a multiple cell complexity making it a relevant assay mimicking the *in vivo* situation. The newly established vascular bed in this assay, like tumor vasculature, is immature and does not contain pericytes. Comparable to the angiogenesis assay, low doses of ENMD-1198 ENMD-1998 slightly enhanced the vascular outgrowth without statistical significance. Higher doses of ENMD-1198 disrupted newly established vasculature with an IC_{50} of approximately $0.8\mu M$ (Figure 6.3c-d).

ENMD-1198 reduces the viability of RAW264.7 osteoclast precursor cells and inhibits PTHrP stimulated bone resorption

The bone effect of ENMD-1198 was assessed *in vitro*. The effects of ENMD-1198 and 2ME2 on the viability of RAW264.7 osteoclast precursor cells were investigated using an MTS colorimetric cell viability assay and with drug concentrations ranging from $0.1\mu M$ to $12.8\mu M$. The MTS assay was performed after 48 hours of ENMD-1198 or 2ME2 exposure. Both ENMD-1198 and 2ME2 reduced RAW264.7 cell viability. With an IC_{50} of approximately $0.4\mu M$, ENMD-1198 was four times more potent than 2ME2 ($IC_{50} \sim 1.6\mu M$) (Figure 6.4a).

After investigating the effects of ENMD-1198 on osteoclast precursor cells, a ^{45}Ca release assay was performed to investigate whether ENMD-1198 could effectively block PTHrP stimulated bone resorption. The assay was conducted using

^{45}Ca -labeled fetal mouse metatarsals in serum free medium with 0.5% BSA. Bone resorption was stimulated by addition of 100nM PTHrP to the culture medium. This culture condition is especially suitable to study effects on PTHrP induced bone resorption.³³ ENMD-1198 effectively blocks PTHrP stimulated ^{45}Ca release in a dose dependent manner (Figure 6.4b).

ENMD-1198 based combination treatments inhibit tumor growth *in vivo*

Following the *in vitro* characterization of ENMD-1198 on the three major processes involved in skeletal metastatic growth of breast cancer, the ENMD-1198 based combination treatment effects were assessed *in vivo*. To investigate the effect on tumor burden, mice were treated either with ENMD-1198, CTX or ENMD-1198 + CTX. Tumor growth was followed using BLI. In all treated groups the tumor burden was decreased significantly compared to the untreated controls by day 27. There was a trend that ENMD-1198 treatment was more effective than CTX alone. A difference between ENMD-1198 and the ENMD-1198 + CTX combination could not be observed (Figure 6.5a).

Next we wanted to investigate whether adding a bisphosphonate (risedronic acid) to the ENMD-1198 + CTX combination would improve the treatment outcome. The ENMD-1198 + CTX treated group had a significantly reduced tumor burden compared to the control by day 21. There was a trend that the ENMD-1198 and the ENMD-1198 + CTX + risedronic acid treated groups had a reduced tumor burden as well. The animals in the control group were sacrificed before these differences could reach significance because the tumor size in the control group exceeded 1cm in diameter, a defined endpoint stated in the Dutch guidelines for animal experiments in cancer research. However, differences in growth kinetics between the treated groups and the untreated group can still be appreciated. The tumor development in this experiment was more rapid than in the previous experiment. In conclusion, adding risedronic acid to the treatment did not improve treatment outcome (Figure 6.5b).

ENMD-1198 based combination treatments are capable to control tumor growth, but are unable to eradicate the tumor

After investigating the treatment effects on tumor burden, the efficacy of long term treatment with ENMD-1198 or ENMD-1198 based combinations was assessed. Seven days after intra-osseous inoculation with MDA-BO2 cells, mice were treated with either ENMD-1198, ENMD-1198 + CTX, ENMD-1198 + risedronic acid, ENMD-1198 + CTX + risedronic acid or vehicle control. The treatment continued for a maximum of ten weeks. In accordance to the Dutch guidelines for animal experiments in cancer research, mice were sacrificed when the tumor diameter exceeded 1cm. All three ENMD-1198 based combination treatments were able to control tumor growth over a prolonged period of time. The animals receiving the combination

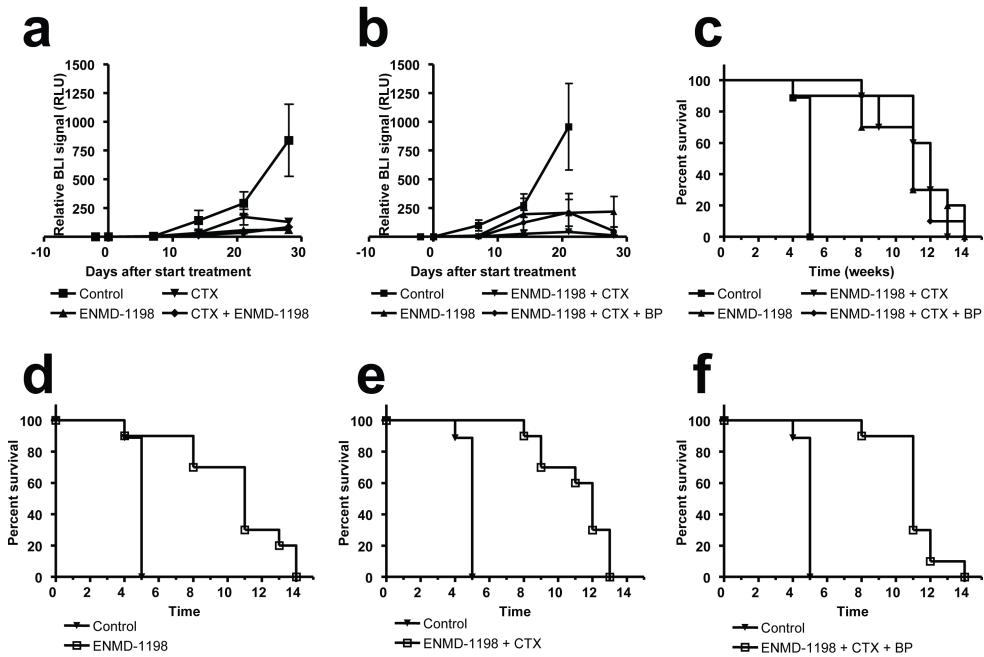


Figure 6.5: ENMD-1198 based combination treatments reduce tumor burden, but does not eradicate the tumor. (a) Treatment started 7 days after inoculation (T0). All treated groups had a reduced tumor burden compared to the untreated control ($*p < 0.05$). There was a trend that the ENMD-1198 treated group had a lower tumor burden compared to the CTX treated group ($p = 0.063$). (b) The ENMD-1198 + CTX combination group had a statistically significant decreased tumor burden compared to the control group at day 21 ($p = 0.026$). There was a trend that the ENMD-1198 and the ENMD-1198 + CTX + risedronic acid treated groups had a reduced tumor burden compared to the untreated controls ($p = 0.088$ and $p = 0.086$ respectively). However, the control mice died before this difference could reach significance. (c) Survival curves of mice treated with ENMD-1198 based combinations. Mice were inoculated intra-osseous with MDA-BO2 cells. Treatment started 7 days after inoculation (T0). Mice were sacrificed when the tumor exceeded 1cm diameter in accordance with local guidelines. Treatment was stopped after 10 weeks. One mouse in the ENMD-1198 treated group died in week 4 due to an accident with the oral gavage. The tumor size reached a steady state in the treated groups during the treatment period, but rapidly expanded after the treatment was stopped. (d-f) Individual graphs for each of the combination treatments. ENMD-1198 versus control (d). ENMD-1198 + CTX versus control (e). ENMD-1198 + CTX + risedronic acid versus control (f).

of ENMD-1198 and risedronic acid appeared less healthy with a thinner skin and aberrant behavior, suggesting possible adverse effects of long term treatment with this combination of drugs. The tumors grew exponentially as soon as the treatment was stopped after ten weeks. The addition of low-dose CTX and/or risedronic acid did not improve treatment outcome (Figure 6.5c-f).

ENMD-1198 protects the bone against tumor-induced osteolysis *in vivo*

Finally, the effect of ENMD-1198 treatment on tumor induced osteolysis was assessed using both X-ray radiographs and high resolution μ CTscans made *ex vivo* after sacrificing the mice. These include untreated controls and groups treated with ENMD-1198 or CTX or a combination of ENMD-1198 + CTX. The corresponding BLI data of these animals are depicted in Figure 6.5a. In the X-ray radiographs, the surface area of osteolytic lesions was measured after manually drawing a region of interest around the lesion. The osteolytic lesions were significantly smaller in groups which received ENMD-1198 than the groups which did not receive ENMD-1198 (Figure 6.6a).

Because the radiograph method is based on a manual definition of the osteolytic lesion we wanted to confirm these results in using a method that is less susceptible to bias. To do so, the bone volumes of the upper half of the tibiae of these mice were measured in μ CTscans. The groups which received ENMD-1198 had a significantly larger bone volume than the groups which did not receive ENMD-1198, confirming the X-ray radiograph data (Figure 6.6b).

Discussion

This study was the first to assess the treatment efficacy of the 2ME2 derived compound ENMD-1198 on osteolytic bone metastasis of breast cancer. Our results indicate that ENMD-1198 interferes with all the crucial processes of bone metastatic growth of breast cancer namely, tumor cell proliferation, angiogenesis and bone resorption. We confirmed our *in vitro* data with a series of *in vivo* experiments showing the beneficial effects of ENMD-1198 and ENMD-1198 based combination treatments of metastatic breast cancer in bone both on tumor progression and survival with long term treatment over a period of 10 weeks. Furthermore, we showed the *in vivo* relevance of the ENMD-1198 protective effect on bone.

The observed *in vitro* effects of ENMD-1198 on cell viability were in line with earlier findings.¹⁹ ENMD-1198 and 2ME2 are microtubule disrupting agents. Similar to other microtubule disrupting agents, they interfere with cell mitosis and thus have profound anti-proliferative effects on tumor cells and during neo-angiogenesis while resting cells are unaffected. Moreover, 2ME2 causes the phosphorylation of Bcl-2 and Bcl-xL leading to an upregulation of the intrinsic and extrinsic apoptotic pathways, a mechanism shared with paclitaxel.³⁵

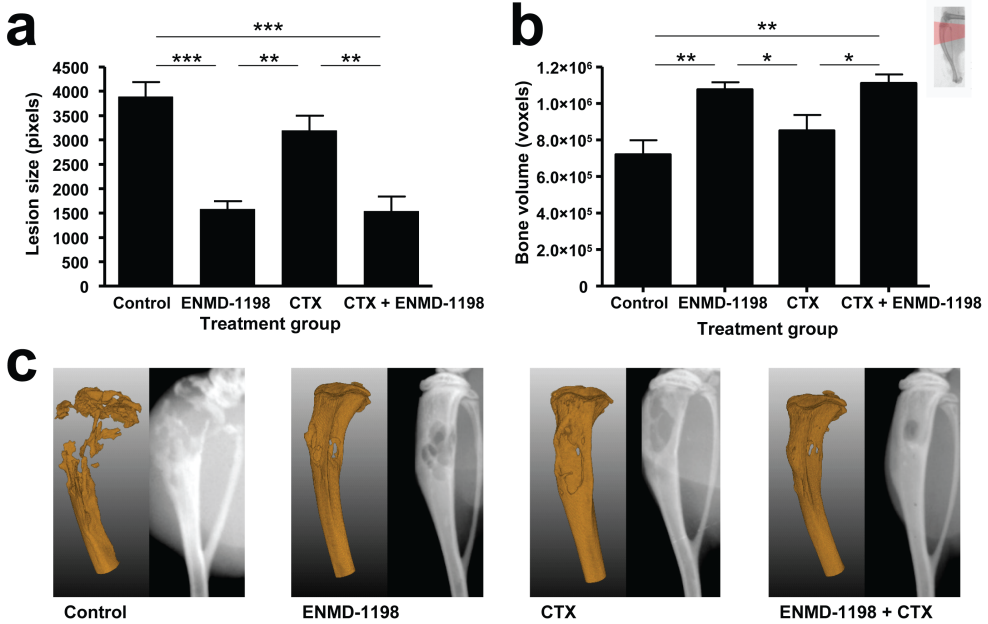


Figure 6.6: ENMD-1198 treatment protects the bone against tumor-induced osteolysis *in vivo*. (a) Quantification of osteolytic lesion size by surface measurement on X-ray radiographs. X-ray radiographs were made after termination of the experiment. The lesion surface was measured in number of pixels. Graphs show the average and standard error of the mean. Groups treated with ENMD-1198 have smaller lesions than the other groups ($**p < 0.01$; $***p < 0.001$). (b) Quantification of osteolytic lesion size volume measurement in μ CTscans. μ CTscans were made after termination of the experiment. Bone volumes of the upper half of the tibia (region of interest is indicated in the inset), cut-off planes were always defined in a 90° degree angle to the bone. Graphs show the average and standard error of the mean. Groups treated with ENMD-1198 had a larger bone volume than the other groups confirming the radiograph data ($*p < 0.05$; $**p < 0.01$). (c) Representative X-ray and μ CT images of all the treatment groups. Both X-ray and μ CT analysis show a reduction in osteolysis in ENMD-1198 treated groups.

ENMD-1198 and 2ME2 reduce angiogenesis by inhibiting the expression and nuclear accumulation of HIF-1. This results in a down regulation of VEGF expression and local pro-angiogenic signaling.^{21,22,36,37} This impaired hypoxia sensing increases local concentrations of radical oxygen species enhancing the pro-apoptotic effects of these compounds.^{21,22} In addition, ENMD-1198 interferes with endothelial cell motility, chemotaxis and morphogenesis into capillary-like structures.²² The results of our *in vitro* angiogenesis assay and vascular disruption assay confirmed these findings.

Metronomic CTX inhibits angiogenesis via three different mechanisms; by direct induction of apoptosis of proliferating tumor endothelial cells, by blocking or reducing the viability of circulating endothelial progenitor cells (EPCs) and by elevating levels of cellular and circulating thrombospondin-1 (TSP-1). These anti-angiogenic effects are enhanced in combination with VEGF inhibitors.^{13,14} Our finding that *in vitro* treatment with 4-HC is not cytotoxic to breast cancer cells were in line with earlier experiments conducted by Bocci *et al.*¹³

We expected to find a strong synergy between the anti-angiogenic effects of ENMD-1198 and metronomic CTX treatments *in vivo* since both treatments have been reported to inhibit angiogenesis via different mechanisms. The CTX + ENMD-1198 combination resulted in a better treatment outcome than CTX treatment alone, but this difference was not profound enough to suggest any synergy between CTX and ENMD-1198. Moreover, adding CTX to ENMD-1198 treatment did improve the overall outcome compared to ENMD-1198 alone in one *in vivo* experiment, but did not in the other.

ENMD-1198 reduced osteoclast precursor cell viability and was able to inhibit PTHrP stimulated bone resorption *in vitro*. When comparing the CTX treated group and the ENMD-1198 treated groups, there was a significant 60% reduction in osteolytic lesion size in the ENMD-1198 treated groups. The differences in tumor burden were much smaller and not significant between all groups. CTX treatment did not improve the osteolytic phenotype compared to the control group even though the tumor burden was significantly lower. Taken together, we conclude a strong bone specific effect of ENMD-1198 treatment.

To date, this is the first study showing these bone-specific effects of ENMD-1198. It has previously been shown that 2ME2 inhibits osteoclast differentiation and bone resorption and is cytotoxic to osteoclasts.³⁸ Interestingly, a 2ME2-mediated upregulation of osteoprotegerin has been described in osteosarcoma cells. This induction of osteoprotegerin can contribute to the anti-resorptive functions of 2ME2 in osteolytic metastatic lesions.^{39,40} Induction of osteoprotegerin might be part of the mechanism in which ENMD-1198 protects the bone matrix from degeneration. The addition of risedronic acid to the combination treatment did not have an effect on tumor growth, nor did it prolong the survival of the animals.

In conclusion, ENMD-1198 treatment of osteolytic bone metastases has profound *in vivo* effects on both tumor growth and osteolysis. ENMD-1198 based combination treatments can control tumor growth; however, the tumor continues growing after treatment is stopped indicating a strong cytostatic effect. Due to the potent

cytostatic and anti-angiogenic effects of ENMD-1198, only a weak additional value of having CTX treatment could be observed. However, any additional value of CTX treatment might be stronger in an immune competent model due to a selective depletion of T_{Reg} cells.⁴¹ ENMD-1198 has strong anti-resorptive properties and the addition of risedronic acid to the treatment did not improve the overall treatment outcome. ENMD-1198 is a promising new compound in the field of metastatic bone disease affecting all processes that are crucial during development and growth of bone metastases.

Acknowledgements

This work has been supported by the Dutch Cancer Society Koningin Wilhelmina Fonds (grant UL2007-3801) (TS) and the 6th FP EU grants EMIL (LSHC-CT-2004-503569) (IM, CL) and DiMI (LSBH-CT-2005-512146) (IQ, EL, CL). ENMD-1198 was a generous gift from Dr. Tony Treston (Entremed Inc. Rockville, MD USA). The authors thank Dr. Alan Chan for proofreading the manuscript.

References

1. Clines GA and Guise TA. Hypercalcaemia of malignancy and basic research on mechanisms responsible for osteolytic and osteoblastic metastasis to bone. *Endocr Relat Cancer*, 2005 Sep;12(3):549–83.
2. Guise TA and Mundy GR. Cancer and bone. *Endocr Rev*, 1998 Feb;19(1):18–54.
3. Mundy GR. Metastasis to bone: causes, consequences and therapeutic opportunities. *Nat Rev Cancer*, 2002 Aug;2(8):584–93.
4. Lin WW and Karin M. A cytokine-mediated link between innate immunity, inflammation, and cancer. *J Clin Invest*, 2007 May;117(5):1175–83.
5. Lorusso G and Rüegg C. The tumor microenvironment and its contribution to tumor evolution toward metastasis. *Histochem Cell Biol*, 2008 Dec;130(6):1091–103.
6. Voorzanger-Rousselot N, Juillet F, Mareau E, Zimmermann J, Kalebic T, and Garnero P. Association of 12 serum biochemical markers of angiogenesis, tumour invasion and bone turnover with bone metastases from breast cancer: a cross-sectional and longitudinal evaluation. *Br J Cancer*, 2006 Aug;95(4):506–14.
7. Sakaguchi S. Naturally arising cd4+ regulatory t cells for immunologic self-tolerance and negative control of immune responses. *Annu Rev Immunol*, 2004;22:531–62.
8. Pertovaara L, Kaipainen A, Mustonen T, Orpana A, Ferrara N, Saksela O, and Alitalo K. Vascular endothelial growth factor is induced in response to transforming growth factor-beta in fibroblastic and epithelial cells. *J Biol Chem*, 1994 Mar;269(9):6271–4.
9. Clines GA and Guise TA. Molecular mechanisms and treatment of bone metastasis. *Expert Rev Mol Med*, 2008;10:e7.
10. Guise TA and Chirgwin JM. Transforming growth factor-beta in osteolytic breast cancer bone metastases. *Clin Orthop Relat Res*, 2003 Oct;415(Suppl):S32–8.
11. Guise TA, Mohammad KS, Clines G, Stebbins EG, Wong DH, Higgins LS, Vessella R, Corey E, Padalecki S, Suva L, and Chirgwin JM. Basic mechanisms responsible for osteolytic and osteoblastic bone metastases. *Clin Cancer Res*, 2006 Oct;12(20 Pt 2):6213s–6216s.
12. Virk MS and Lieberman JR. Tumor metastasis to bone. *Arthritis Res Ther*, 2007;9 Suppl 1:S5.
13. Bocci G, Nicolaou KC, and Kerbel RS. Protracted low-dose effects on human endothelial cell proliferation and survival in vitro reveal a selective antiangiogenic window for various chemotherapeutic drugs. *Cancer Res*, 2002 Dec;62(23):6938–43.
14. Man S, Bocci G, Francia G, Green SK, Jothy S, Hanahan D, Bohlen P, Hicklin DJ, Bergers G, and Kerbel RS. Antitumor effects in mice of low-dose (metronomic) cyclophosphamide administered continuously through the drinking water. *Cancer Res*, 2002 May;62(10):2731–5.

15. Lutsiak MEC, Semnani RT, De Pascalis R, Kashmiri SVS, Schlom J, and Sabzevari H. Inhibition of cd4(+)25+ t regulatory cell function implicated in enhanced immune response by low-dose cyclophosphamide. *Blood*, 2005 Apr;105(7):2862–8.
16. Zhao J, Cao Y, Lei Z, Yang Z, Zhang B, and Huang B. Selective depletion of cd4+cd25+foxp3+ regulatory t cells by low-dose cyclophosphamide is explained by reduced intracellular atp levels. *Cancer Res*, 2010 Jun;70(12):4850–8.
17. Mooberry SL. Mechanism of action of 2-methoxyestradiol: new developments. *Drug Resist Updat*, 2003 Dec;6(6):355–61.
18. Mooberry SL. New insights into 2-methoxyestradiol, a promising antiangiogenic and antitumor agent. *Curr Opin Oncol*, 2003 Nov;15(6):425–30.
19. Agoston GE, Shah JH, Suwandi L, Hanson AD, Zhan X, LaVallee TM, Pribluda V, and Treston AM. Synthesis, antiproliferative, and pharmacokinetic properties of 3- and 17-double-modified analogs of 2-methoxyestradiol. *Bioorg Med Chem Lett*, 2009 Nov;19(21):6241–4.
20. LaVallee TM, Burke PA, Swartz GM, Hamel E, Agoston GE, Shah J, Suwandi L, Hanson AD, Fogler WE, Sidor CF, and Treston AM. Significant antitumor activity in vivo following treatment with the microtubule agent enmd-1198. *Mol Cancer Ther*, 2008 Jun;7(6):1472–82.
21. Moser C, Lang SA, Mori A, Hellerbrand C, Schlitt HJ, Geissler EK, Fogler WE, and Stoeltzing O. Enmd-1198, a novel tubulin-binding agent reduces hif-1alpha and stat3 activity in human hepatocellular carcinoma(hcc) cells, and inhibits growth and vascularization in vivo. *BMC Cancer*, 2008;8:206.
22. Pasquier E, Sinnappan S, Munoz MA, and Kavallaris M. Enmd-1198, a new analogue of 2-methoxyestradiol, displays both antiangiogenic and vascular-disrupting properties. *Mol Cancer Ther*, 2010 May;9(5):1408–18.
23. Zhou Q, Gustafson D, Nallapareddy S, Diab S, Leong S, Lewis K, Gore L, Messersmith WA, Treston AM, Eckhardt SG, Sidor C, and Camidge DR. A phase i dose-escalation, safety and pharmacokinetic study of the 2-methoxyestradiol analog enmd-1198 administered orally to patients with advanced cancer. *Invest New Drugs*, 2011 Apr;29(2):340–6.
24. Buijs JT, Que I, Löwik CWGM, Papapoulos SE, and van der Pluijm G. Inhibition of bone resorption and growth of breast cancer in the bone microenvironment. *Bone*, 2009 Feb;44(2):380–6.
25. Drake MT, Clarke BL, and Khosla S. Bisphosphonates: mechanism of action and role in clinical practice. *Mayo Clin Proc*, 2008 Sep;83(9):1032–45.
26. van der Pluijm G, Vloedgraven H, van Beek E, van der Wee-Pals L, Löwik C, and Papapoulos S. Bisphosphonates inhibit the adhesion of breast cancer cells to bone matrices in vitro. *J Clin Invest*, 1996 Aug;98(3):698–705.

27. van der Pluijm G, Que I, Sijmons B, Buijs JT, Löwik CWGM, Wetterwald A, Thalmann GN, Papapoulos SE, and Cecchini MG. Interference with the microenvironmental support impairs the de novo formation of bone metastases in vivo. *Cancer Res*, 2005 Sep;65(17):7682–90.
28. Body JJ, Diel IJ, Lichinitzer M, Lazarev A, Pecherstorfer M, Bell R, Tripathy D, and Bergstrom B. Oral ibandronate reduces the risk of skeletal complications in breast cancer patients with metastatic bone disease: results from two randomised, placebo-controlled phase iii studies. *Br J Cancer*, 2004 Mar;90(6):1133–7.
29. Peyruchaud O, Winding B, Pécheur I, Serre CM, Delmas P, and Clézardin P. Early detection of bone metastases in a murine model using fluorescent human breast cancer cells: application to the use of the bisphosphonate zoledronic acid in the treatment of osteolytic lesions. *J Bone Miner Res*, 2001 Nov;16(11):2027–34.
30. Wetterwald A, van der Pluijm G, Que I, Sijmons B, Buijs J, Karperien M, Löwik CWGM, Gautschi E, Thalmann GN, and Cecchini MG. Optical imaging of cancer metastasis to bone marrow: a mouse model of minimal residual disease. *Am J Pathol*, 2002 Mar;160(3):1143–53.
31. Deckers M, van der Pluijm G, Dooijewaard S, Kroon M, van Hinsbergh V, Papapoulos S, and Löwik C. Effect of angiogenic and antiangiogenic compounds on the outgrowth of capillary structures from fetal mouse bone explants. *Lab Invest*, 2001 Jan;81(1):5–15.
32. van Wijngaarden J, Snoeks TJA, van Beek E, Bloys H, Kaijzel EL, van Hinsbergh VWM, and Löwik CWGM. An in vitro model that can distinguish between effects on angiogenesis and on established vasculature: actions of tnp-470, marimastat and the tubulin-binding agent ang-510. *Biochem Biophys Res Commun*, 2010 Jan;391(2):1161–5.
33. van beek E, Löwik C, van der Pluijm G, and Papapoulos S. The role of geranylgeranylation in bone resorption and its suppression by bisphosphonates in fetal bone explants in vitro: A clue to the mechanism of action of nitrogen-containing bisphosphonates. *J Bone Miner Res*, 1999 May;14(5):722–9.
34. Emmenegger U, Shaked Y, Man S, Bocci G, Spasojevic I, Francia G, Kouri A, Coke R, Cruz-Munoz W, Ludeman SM, Colvin OM, and Kerbel RS. Pharmacodynamic and pharmacokinetic study of chronic low-dose metronomic cyclophosphamide therapy in mice. *Mol Cancer Ther*, 2007 Aug;6(8):2280–9.
35. Basu A and Haldar S. Identification of a novel bcl-xl phosphorylation site regulating the sensitivity of taxol- or 2-methoxyestradiol-induced apoptosis. *FEBS Lett*, 2003 Mar;538(1-3):41–7.
36. Dunn LK, Mohammad KS, Fournier PGJ, McKenna CR, Davis HW, Niewolna M, Peng XH, Chirgwin JM, and Guise TA. Hypoxia and tgf-beta drive breast cancer bone metastases through parallel signaling pathways in tumor cells and the bone microenvironment. *PLoS One*, 2009;4(9):e6896.

37. Mabweesh NJ, Escuin D, LaVallee TM, Pribluda VS, Swartz GM, Johnson MS, Willard MT, Zhong H, Simons JW, and Giannakakou P. 2me2 inhibits tumor growth and angiogenesis by disrupting microtubules and dysregulating hif. *Cancer Cell*, 2003 Apr; 3(4):363–75.
38. Maran A, Gorny G, Oursler MJ, Zhang M, Shogren KL, Yaszemski MJ, and Turner RT. 2-methoxyestradiol inhibits differentiation and is cytotoxic to osteoclasts. *J Cell Biochem*, 2006 Oct;99(2):425–34.
39. Benedikt MB, Mahlum EW, Shogren KL, Subramaniam M, Spelsberg TC, Yaszemski MJ, and Maran A. 2-methoxyestradiol-mediated anti-tumor effect increases osteoprotegerin expression in osteosarcoma cells. *J Cell Biochem*, 2010 Apr;109(5):950–6.
40. Cicek M, Iwaniec UT, Goblirsch MJ, Vrabel A, Ruan M, Clohisy DR, Turner RR, and Oursler MJ. 2-methoxyestradiol suppresses osteolytic breast cancer tumor progression in vivo. *Cancer Res*, 2007 Nov;67(21):10106–11.
41. Ghiringhelli F, Menard C, Puig PE, Ladoire S, Roux S, Martin F, Solary E, Le Cesne A, Zitvogel L, and Chauffert B. Metronomic cyclophosphamide regimen selectively depletes cd4+cd25+ regulatory t cells and restores t and nk effector functions in end stage cancer patients. *Cancer Immunol Immunother*, 2007 May;56(5):641–8.

7

Summary & Conclusions and a Future Perspective

Summary & Conclusions

Bone metastatic growth is characterized by tumor-induced bone resorption and subsequent tumor stimulation by factors released from the resorbed bone matrix. This feedback mechanism is known as the vicious cycle of bone metastases.

The complex interaction between bone metastases and the bone micro-environment requires a treatment interfering with multiple pathways. Bone resorption is an attractive treatment target to halt the vicious cycle of bone metastases. This, can be targeted alongside other processes such as tumor cell proliferation and survival, angiogenesis and immune modulation. Angiogenesis can be slowed down by inhibiting VEGF signaling and preventing the recruitment of circulating endothelial precursor cells (CEPs). The immune system could potentially be activated by targeting regulatory T-cells (T_{reg}). Transforming growth factor- β (TGF- β) is released and activated during bone resorption. Thus, TGF- β stimulation of the tumor can be stopped by inhibiting osteolysis. The inhibition of osteolysis can either be achieved by direct targeting of osteoclasts activity or by blocking osteoclast differentiation. Decreased levels of TGF- β will lead to a decrease in secretion of pro-osteolytic factors, such as parathyroid hormone-related protein (PTHrP) and macrophage colony-stimulating factor (M-CSF), by the tumor cells. In addition, the tumor will be left more susceptible to apoptosis. Evaluating the treatment result of such a combined intervention in a multi-factorial disease process requires simultaneous measurement and follow up of multiple processes.

Due to their non-invasive nature, whole body molecular imaging techniques are especially suitable for longitudinal studies. Imaging techniques are unique tools. They enable the quantification of structural changes and disease related processes such as angiogenesis and tumor growth in a non-invasive manner and at multiple time points. Altogether, molecular imaging provides the researcher the possibility of evaluating the result of a therapeutic intervention in over time in the same animal.¹⁻³

Radiography and optical imaging techniques are primarily two dimensional (2D). However, recent advances have resulted in fluorescence molecular tomography (FMT) and other three dimensional (3D) fluorescence and bioluminescence data capturing methods as well as specialized small animal micro-CT (μ CT) scanners.^{1,3-5} The transition from 2D to 3D results in more realistic data and possibly better quantification. However, the navigation through 3D datasets is less intuitive than 2D datasets. Moreover, the determination of a volume of interest (VOI) is more complicated than the selection of a two dimensional region of interest (ROI).⁶

Chapter 2 of this thesis describes a method to generate normalized cross-sections and select VOIs in complex data. The method is based on the definition of a centerline through a long-bone of interest. The naturally curved centerline can then be "straightened" to generate a new, normalized volume. This new volume can then be used to extract normalized cross-sections or to define a normalized VOI. The actual measurement of the selected volume is performed in the original volume to prevent measurement artifacts due to the straightening procedure. Following this method,

VOIs are defined relative to the anatomy of the bone.⁶

An automated method has been developed in-house to follow longitudinal studies both qualitatively and quantitatively. This method, described in chapter 3, is based in part on a previously published method to fit an animal atlas over μ CT scan data.^{7,8} Subsequently, a predefined VOI can be segmented and measured. These volume measurements are performed fully automated. The acquired data does not differ significantly from manual segmentation and measurements.⁹

Using a center-line-based approach, sub-volume datasets of long-bones can be transformed into a stack of slices cutting through the bone under a 90° angle (Chapter 2).⁶ A similar approach has been implemented in the automated method, but instead of defining a center-line per scan, the center-line of the segmented atlas bone is used. The thickness of the bone cortex can be determined in these orthogonal slices. All the cortical thickness data of the bone of interest can then be projected as color code on a volume rendering of the bone. This method of generating cortical thickness maps, described in chapter 3 is a valuable tool to study changes in the bone anatomy over time. The user of this method can identify the location of osteolytic and osteosclerotic regions.⁹ This helps in defining regions of interest for further analysis of the acquired imaging datasets or for subsequent histological examination.

μ CT gives a detailed insight in structural changes during the course of a disease and/or treatment. More insight into the direct molecular and mechanistic response can be acquired by combining structural imaging modalities with functional imaging. It is not only possible to acquire 3D optical data, but also to project these 3D optical data sets back onto scans of various other modalities (e.g. μ CT, PET, SPECT and MRI). Combining multiple imaging modalities within one study offers unique research opportunities, but it also lies at the core of the major challenges in data analysis. Datasets are acquired using various highly specialized cameras and machines. Each one of these machines often have specific requirements in terms of anesthetics and animal positioning and produce data in various formats. Animal handling and moving animals from one machine to another introduce variations in animal posture between datasets. Most of these posture variations can be prevented by performing these actions with care. However, the posture variations are even more abundant in longitudinal studies where animals are imaged at multiple time points, often with intervals of several weeks. In these cases, specialized animal holders have proven to be insufficient. Also, during longer studies, for example five or six weeks, growth of the animal between scans becomes a problem.

Chapters 2 and 3 show how posture variation can be normalized in μ CT scans. In chapter 4 an approach to integrated data handling has been described which uses the skeleton as a reference frame in order to compensate for posture variations in datasets acquired with other modalities. This approach is based on the registration and segmentation of μ CT data. In this case 3D optical or nuclear imaging data (positron emission tomography (PET) and single photon emission computed tomography (SPECT)) is coupled to the μ CT data and segmented alongside. Also the handling of MRI data is currently dependent on μ CT, but this could be improved in

future since magnetic resonance imaging (MRI) provides skeletal contrast in addition to soft tissue contrast.

A great number of *in vitro* assays are available which are used to evaluate the effect of possible new treatments in a laboratory setting. There are many different ways to assess the anti-angiogenic capabilities of a compound. These assays include proliferation assays of human umbilical vein endothelial cells (HUVECs) and tube forming assays in three dimensional culture systems. Most of these *in vitro* models for angiogenesis include only one cell type, namely endothelial cells. However, angiogenesis is a complex process in which multiple cell types interact. Moreover, existing assays focus on quantifying the effect of compounds on vascular outgrowth and the formation of new vessels. The vascular disruption capability of a new compound is often not quantified.

A new vascular disruption assay is described in chapter 5. This assay is a variation to an angiogenesis assay developed within the LUMC by Deckers *et al.*¹⁰ The angiogenesis and vascular disruption assay are unique in the sense that they consist of *ex vivo* bone explants containing all cell types involved in vasculogenesis. The newly formed vascular bed in these assays is a model for tumor vasculature which, much like the vessels in these assays, is poorly matured and often lacks support by pericytes and smooth muscle tissue.¹⁰ The vascular disruption assay described in this thesis is the first multicellular assay which can be used to quantify treatment responses on newly established vasculature.¹¹

The *in vitro* angiogenesis and vascular disruption assays and the methods of analyzing μ CT scans have been used in chapter 6 for evaluation of the treatment effect of a combination treatment for bone metastases. The rationale behind the treatment design was to simultaneously target all the important processes during metastatic growth in bone, namely tumor growth, angiogenesis and bone resorption. The treatment consisted of ENMD-1198 (a 2-Methoxyestradiol (2ME2) derivate), low dose “metronomic” cyclophosphamide and the bisphosphonate risedronate.

2ME2 is a microtubule targeting agent (MTA). As such 2ME2 has anti-proliferative effects against fast dividing cells such as cancerous cells and developing endothelial cells during angiogenesis.^{12–15} Moreover, 2ME2 causes the phosphorylation of Bcl-2 and Bcl-xL, leading to an upregulation of the intrinsic and extrinsic apoptotic pathways, a mechanism shared with paclitaxel.¹⁶

The anti-angiogenic effects of 2ME2 are not solely caused by its cytotoxicity towards endothelial cells. It also inhibits hypoxia-inducible factor-1 α (HIF-1 α) expression.^{17,18} HIF-1 α is a pro-angiogenic factor regulating over 70 genes involved in many cancer related processes like angiogenesis, glycolysis, metastasis and cell growth, amongst which VEGF.^{19,20}

Furthermore 2ME2 inhibited intra-osseous growth of 4T1 and MDA-MB-231 breast cancer cells and protects the bone from subsequent cancer-induced osteolysis.^{21,22} This protective effect of 2ME2 on bone is not only a result of a reduced tumor burden. 2ME2 is also capable of suppressing osteoclast differentiation and induces apoptosis of mature osteoclasts.²³ Moreover, 2ME2 effectively represses bone

loss in an animal model of post-menopausal osteoporosis²⁴ and it preserved bone and reduced the frequency and severity of arthritis in a model of postmenopausal rheumatoid arthritis.²⁵

Chapter 6 describes a study where the 2ME2 derived compound ENMD-1198 was used to treat bone metastatic growth following intra-osseous inoculation with MDA-BO2 cells, a bone specific subclone of the MDA-MB-231 breast cancer cell line.²⁶ ENMD-1198 is a slightly modified form of 2ME2 which has better characteristics in terms of metabolic stability, anti-angiogenic activity and cytotoxicity.^{27,28} We showed that ENMD-1198 has direct effects on tumor growth, angiogenesis and bone turnover.²⁹

ENMD-1198 treatment was combined with low dose “metronomic” Cyclophosphamide (CTX) in order to improve the anti-angiogenic and anti-vasculogenic effects of the treatment. CTX is a cytostatic drug which is often in combination with other anti-neoplastic drugs to treat malignant lymphomas at the maximum tolerated dose. It is also used as adjuvant therapy in metastasized ovarian, breast and prostate cancers. CTX is not cytotoxic in its original form but requires activation by P450 metabolism in the liver.^{30,31} Metabolism results in the active metabolite 4-Hydroxyperoxycyclophosphamide (4HC).³² The low dose used in this study has been proposed as anti-angiogenic therapy rather than inducing direct tumor cell death.

It has already been shown that cytotoxic agents can have anti-angiogenic properties at low dose. In 1986, Polverini and Novak were the first to show this with low dosing of mitoxantrone and bisantrene, two cytotoxic agents which were in clinical trial at the time.³³ A dose dependent inhibition of angiogenesis was found using a vascularization model of the rat cornea. Interestingly, the authors explicitly note that there was no untoward toxicity to the tissue at the drug concentrations used in the experiment. There are three suggested mechanisms underlying the antiangiogenic effect of metronomic chemotherapy using CTX. First, by directly inducing apoptosis of proliferating tumor endothelial cells.³⁴ Secondly, by blocking or reducing the viability of circulating endothelial progenitor cells (EPCs).³⁵ Thirdly, by elevating the levels of cellular and circulating thrombospondin-1 (TSP-1).³⁶ The anti-angiogenic effect of metronomic chemotherapy seems to be much stronger in combination with anti-angiogenic compounds such as VEGF inhibitors.³⁷ In addition to the anti-angiogenic effects, metronomic cyclophosphamide causes a selective depletion of T_{reg} cells resulting in an enhanced tumor immune response.^{38,39} Low dose CTX has no, or very low, effect on tissues that are otherwise highly sensitive to maximum tolerated dose CTX treatment.⁴⁰

Both ENMD-1198 and metronomic CTX target angiogenesis and tumor vasculature. The main mechanism of ENMD-1198 is to render the tumor cells irresponsive to hypoxia by interfering with HIF-1 α signalling; thus down-regulating VEGF expression.²⁷ On the other hand, the antiangiogenic effect of metronomic CTX is largely VEGF independent. It targets endothelial cells of tumor vasculature and vascular repair by circulating endothelial cells. The fact that these mechanisms of action are independent suggest a possible synergy between these compounds in combination

treatment. The data presented in chapter 6 however, showed only a mild benefit of combined treatment compared to ENMD-1198 treatment alone. The ENMD-1198 treatment alone was very effective leaving only little room for improvement. Moreover, the experiments were performed in an immune deficient model while part of the low dose CTX treatment effect works through alterations of the local immune system. This results in suboptimal treatment effects in the chosen model.²⁹

In order to halt the vicious cycle of bone destruction, the treatment was combined with bisphosphonates (BPs). BPs are widely used in the clinic for the management of osteoporosis, metastatic bone disease and Paget's disease ever since patient with myositis ossificans was treated with BPs, called diphosphonates at the time, for the first time in 1969.⁴¹⁻⁴⁴

BP treatment halts the cycle of bone metastatic growth by blocking osteoclast function.⁴⁵ BP treatment reduces skeletal complications and morbidity in patients with bone metastases, but it is not curative.⁴⁶ *In vivo* evidence suggests that BPs can prevent the development of new metastases. However, established metastases remain largely unaffected by BP treatment.⁴⁷ A possible explanation for this lies within the vicious cycle which promotes osteolytic bone metastatic growth. The positive feedback within this cycle is so strong that the cancer induced osteolysis becomes practically irresponsive to treatment.

Recent studies suggest that zoledronate treatment stimulates an anti-tumor immune response.⁴⁸⁻⁵⁰ The immune activation of zoledronate is currently studied in phase I and II clinical trials.^{48,51,52} Also, several studies indicate direct cytotoxic and anti-proliferative effects of BPs towards tumor cells.⁵³⁻⁵⁵ The actual clinical relevance of these studies remains unclear as these studies are often performed with very high BP concentrations.⁵⁶

Risedronate was added to the ENMD-1198 based combination therapy. It was postulated that, in a combination, BP and ENMD-1198 may be able to stop local osteolysis altogether. The results presented in chapter 6 were less optimistic. Adding a bisphosphonate to the mixture did not result in improved treatment efficacy. In addition, potentially adverse effects were observed in the animals receiving a combination of ENMD-1198, CTX and BPs.²⁹ Future work should be aimed at optimizing the dose of the individual treatments. Moreover, the role of a possible immune component should be investigated using tumor models suitable for immunological research. Chapter 6 is, apart from its biological significance, an example of how tools like those described in chapter 2, can facilitate research.

Taken together, this thesis describes methods to measure structural changes in the skeleton using μ CT resulting in normalized qualitative and quantitative assessment of bone volume and thickness. In addition, normalized cross sections can be generated to allow side-by-side comparison of scan data. It has been shown that these methods can be used to identify biologically relevant changes. In addition, ENMD-1198 was identified as a promising compound for the treatment of bone metastases.

Future Perspective

Molecular imaging and image analysis are fast developing fields. Constant technological advances result in many new exciting tools and possibilities, but also new challenges to overcome. Much of the published work in the field of image analysis has been generated with custom made source codes and scripts. The translation into more user friendly interfaces often lags behind. This is unfortunate because many good solutions to existing problems stay unnoticed for people using imaging techniques as research tool as these people themselves are often not experts in image analysis. It is therefore important that more user friendly interfaces are developed.

One of the exciting aspects of the field of molecular imaging is the fact that these techniques are at the crossroads of pre-clinical and clinical practice and of diagnosis and treatment. Many of the image analysis techniques, both described in this thesis and in other publications, can potentially be used for clinical purposes as well. The reverse, where clinical applications can be used to solve pre-clinical problems, is often true as well. The use of a kinetic atlas to segment datasets and visualize changes over time is not yet used in the clinic. However, radiologists are positive to the idea of developing this approach for clinical applications.

Optical imaging modalities are becoming more important in diagnosis and treatment. Fluorescence imaging is already being used in operation theaters for sentinel lymph-node procedures. Also, peri-operative use of topically applied tumor specific probes on excised tissue is under clinical evaluation. Optical mammography is under clinical evaluation as a method of monitoring early treatment response to neo-adjuvant therapy. Further development of clinically approved cancer specific probes could have a great impact on this field, in the operation theatre, for diagnosis and during patient follow up.

Currently, methods of aligning partial and whole body clinical CT and MRI data are being developed within the LUMC department of radiology. The basic principles of these techniques have their origin in the atlas based approaches developed for pre-clinical image processing.

References

1. Kaijzel EL, Snoeks TJA, Buijs JT, van der Pluijm G, and Löwik CWGM. Multimodal imaging and treatment of bone metastasis. *Clin Exp Metastasis*, 2009;26(4):371–9.
2. Snoeks TJA, Löwik CWGM, and Kaijzel EL. 'in vivo' optical approaches to angiogenesis imaging. *Angiogenesis*, 2010 Jun;13(2):135–47.
3. Snoeks TJA, Khmelinskii A, Lelieveldt BPF, Kaijzel EL, and Löwik CWGM. Optical advances in skeletal imaging applied to bone metastases. *Bone*, 2011 Jan;48(1):106–14.
4. Kozloff KM, Weissleder R, and Mahmood U. Noninvasive optical detection of bone mineral. *J Bone Miner Res*, 2007 Aug;22(8):1208–16.
5. Ntziachristos V, Tung CH, Bremer C, and Weissleder R. Fluorescence molecular tomography resolves protease activity in vivo. *Nat Med*, 2002 Jul;8(7):757–60.
6. Snoeks TJA, Kaijzel EL, Que I, Mol IM, Löwik CWGM, and Dijkstra J. Normalized volume of interest selection and measurement of bone volume in microct scans. *Bone*, 2011 Dec;49(6):1264–9.
7. Baiker M, Milles J, Dijkstra J, Henning TD, Weber AW, Que I, Kaijzel EL, Löwik CWGM, Reiber JHC, and Lelieveldt BPF. Atlas-based whole-body segmentation of mice from low-contrast micro-ct data. *Med Image Anal*, 2010 Dec;14(6):723–37.
8. Kok P, Baiker M, Hendriks EA, Post FH, Dijkstra J, Löwik CWGM, Lelieveldt BPF, and Botha CP. Articulated planar reformation for change visualization in small animal imaging. *IEEE Trans Vis Comput Graph*, 2010;16(6):1396–404.
9. Baiker M, Snoeks TJA, Kaijzel EL, Que I, Dijkstra J, Lelieveldt BPF, and Löwik CWGM. Automated bone volume and thickness measurements in small animal whole-body microct data. *Mol Imaging Biol*, 2011 Oct;.
10. Deckers M, van der Pluijm G, Dooijewaard S, Kroon M, van Hinsbergh V, Papapoulos S, and Löwik C. Effect of angiogenic and antiangiogenic compounds on the outgrowth of capillary structures from fetal mouse bone explants. *Lab Invest*, 2001 Jan;81(1):5–15.
11. van Wijngaarden J, Snoeks TJA, van Beek E, Bloys H, Kaijzel EL, van Hinsbergh VWM, and Löwik CWGM. An in vitro model that can distinguish between effects on angiogenesis and on established vasculature: actions of tnp-470, marimastat and the tubulin-binding agent ang-510. *Biochem Biophys Res Commun*, 2010 Jan;391(2):1161–5.
12. D'Amato RJ, Lin CM, Flynn E, Folkman J, and Hamel E. 2-methoxyestradiol, an endogenous mammalian metabolite, inhibits tubulin polymerization by interacting at the colchicine site. *Proc Natl Acad Sci U S A*, 1994 Apr;91(9):3964–8.
13. Dubey RK, Gillespie DG, Jackson EK, and Keller PJ. 17beta-estradiol, its metabolites, and progesterone inhibit cardiac fibroblast growth. *Hypertension*, 1998 Jan;31(1 Pt 2):522–8.

14. Fotsis T, Zhang Y, Pepper MS, Adlercreutz H, Montesano R, Nawroth PP, and Schweigerer L. The endogenous oestrogen metabolite 2-methoxyoestradiol inhibits angiogenesis and suppresses tumour growth. *Nature*, 1994 Mar;368(6468):237–9.
15. Pribluda VS, Gubish ER Jr, Lavallee TM, Treston A, Swartz GM, and Green SJ. 2-methoxyestradiol: an endogenous antiangiogenic and antiproliferative drug candidate. *Cancer Metastasis Rev*, 2000;19(1-2):173–9.
16. Basu A and Haldar S. Identification of a novel bcl-xl phosphorylation site regulating the sensitivity of taxol- or 2-methoxyestradiol-induced apoptosis. *FEBS Lett*, 2003 Mar; 538(1-3):41–7.
17. Mabjeesh NJ, Escuin D, LaVallee TM, Pribluda VS, Swartz GM, Johnson MS, Willard MT, Zhong H, Simons JW, and Giannakakou P. 2me2 inhibits tumor growth and angiogenesis by disrupting microtubules and dysregulating hif. *Cancer Cell*, 2003 Apr; 3(4):363–75.
18. Ricker JL, Chen Z, Yang XP, Pribluda VS, Swartz GM, and Van Waes C. 2-methoxyestradiol inhibits hypoxia-inducible factor 1alpha, tumor growth, and angiogenesis and augments paclitaxel efficacy in head and neck squamous cell carcinoma. *Clin Cancer Res*, 2004 Dec;10(24):8665–73.
19. Giaccia A, Siim BG, and Johnson RS. Hif-1 as a target for drug development. *Nat Rev Drug Discov*, 2003 Oct;2(10):803–11.
20. Semenza GL. Targeting hif-1 for cancer therapy. *Nat Rev Cancer*, 2003 Oct;3(10):721–32.
21. Cicek M, Iwaniec UT, Goblirsch MJ, Vrabel A, Ruan M, Clohisy DR, Turner RR, and Oursler MJ. 2-methoxyestradiol suppresses osteolytic breast cancer tumor progression in vivo. *Cancer Res*, 2007 Nov;67(21):10106–11.
22. Dunn LK, Mohammad KS, Fournier PGJ, McKenna CR, Davis HW, Niewolna M, Peng XH, Chirgwin JM, and Guise TA. Hypoxia and tgf-beta drive breast cancer bone metastases through parallel signaling pathways in tumor cells and the bone microenvironment. *PLoS One*, 2009;4(9):e6896.
23. Maran A, Gorny G, Oursler MJ, Zhang M, Shogren KL, Yaszemski MJ, and Turner RT. 2-methoxyestradiol inhibits differentiation and is cytotoxic to osteoclasts. *J Cell Biochem*, 2006 Oct;99(2):425–34.
24. Sibonga JD, Lotinun S, Evans GL, Pribluda VS, Green SJ, and Turner RT. Dose-response effects of 2-methoxyestradiol on estrogen target tissues in the ovariectomized rat. *Endocrinology*, 2003 Mar;144(3):785–92.
25. Stubelius A, Andréasson E, Karlsson A, Ohlsson C, Tivesten A, Islander U, and Carlsten H. Role of 2-methoxyestradiol as inhibitor of arthritis and osteoporosis in a model of postmenopausal rheumatoid arthritis. *Clin Immunol*, 2011 Jul;140(1):37–46.

26. Wetterwald A, van der Pluijm G, Que I, Sijmons B, Buijs J, Karperien M, Löwik CWGM, Gautschi E, Thalmann GN, and Cecchini MG. Optical imaging of cancer metastasis to bone marrow: a mouse model of minimal residual disease. *Am J Pathol*, 2002 Mar;160(3):1143–53.
27. Moser C, Lang SA, Mori A, Hellerbrand C, Schlitt HJ, Geissler EK, Fogler WE, and Stoeltzing O. Enmd-1198, a novel tubulin-binding agent reduces hif-1alpha and stat3 activity in human hepatocellular carcinoma(hcc) cells, and inhibits growth and vascularization in vivo. *BMC Cancer*, 2008;8:206.
28. Pasquier E, Sinnappan S, Munoz MA, and Kavallaris M. Enmd-1198, a new analogue of 2-methoxyestradiol, displays both antiangiogenic and vascular-disrupting properties. *Mol Cancer Ther*, 2010 May;9(5):1408–18.
29. Snoeks TJA, Mol IM, Que I, Kaijzel EL, and Löwik CWGM. 2-methoxyestradiol analogue enmd-1198 reduces breast cancer-induced osteolysis and tumor burden both in vitro and in vivo. *Mol Cancer Ther*, 2011 May;10(5):874–82.
30. Clarke L and Waxman DJ. Oxidative metabolism of cyclophosphamide: identification of the hepatic monooxygenase catalysts of drug activation. *Cancer Res*, 1989 May;49(9):2344–50.
31. Colvin M and Hilton J. Pharmacology of cyclophosphamide and metabolites. *Cancer Treat Rep*, 1981;65 Suppl 3:89–95.
32. Emmenegger U, Shaked Y, Man S, Bocci G, Spasojevic I, Francia G, Kouri A, Coke R, Cruz-Munoz W, Ludeman SM, Colvin OM, and Kerbel RS. Pharmacodynamic and pharmacokinetic study of chronic low-dose metronomic cyclophosphamide therapy in mice. *Mol Cancer Ther*, 2007 Aug;6(8):2280–9.
33. Polverini PJ and Novak RF. Inhibition of angiogenesis by the antineoplastic agents mitoxantrone and bisantrene. *Biochem Biophys Res Commun*, 1986 Nov;140(3):901–7.
34. Bocci G, Nicolaou KC, and Kerbel RS. Protracted low-dose effects on human endothelial cell proliferation and survival in vitro reveal a selective antiangiogenic window for various chemotherapeutic drugs. *Cancer Res*, 2002 Dec;62(23):6938–43.
35. Bertolini F, Paul S, Mancuso P, Monestiroli S, Gobbi A, Shaked Y, and Kerbel RS. Maximum tolerable dose and low-dose metronomic chemotherapy have opposite effects on the mobilization and viability of circulating endothelial progenitor cells. *Cancer Res*, 2003 Aug;63(15):4342–6.
36. Bocci G, Francia G, Man S, Lawler J, and Kerbel RS. Thrombospondin 1, a mediator of the antiangiogenic effects of low-dose metronomic chemotherapy. *Proc Natl Acad Sci U S A*, 2003 Oct;100(22):12917–22.
37. Man S, Bocci G, Francia G, Green SK, Jothy S, Hanahan D, Bohlen P, Hicklin DJ, Bergers G, and Kerbel RS. Antitumor effects in mice of low-dose (metronomic) cyclophosphamide administered continuously through the drinking water. *Cancer Res*, 2002 May;62(10):2731–5.

38. Lutsiak MEC, Semnani RT, De Pascalis R, Kashmiri SVS, Schlom J, and Sabzevari H. Inhibition of cd4(+)25+ t regulatory cell function implicated in enhanced immune response by low-dose cyclophosphamide. *Blood*, 2005 Apr;105(7):2862–8.
39. Zhao J, Cao Y, Lei Z, Yang Z, Zhang B, and Huang B. Selective depletion of cd4+cd25+foxp3+ regulatory t cells by low-dose cyclophosphamide is explained by reduced intracellular atp levels. *Cancer Res*, 2010 Jun;70(12):4850–8.
40. Emmenegger U, Man S, Shaked Y, Francia G, Wong JW, Hicklin DJ, and Kerbel RS. A comparative analysis of low-dose metronomic cyclophosphamide reveals absent or low-grade toxicity on tissues highly sensitive to the toxic effects of maximum tolerated dose regimens. *Cancer Res*, 2004 Jun;64(11):3994–4000.
41. Bassett CA, Donath A, Macagno F, Preisig R, Fleisch H, and Francis MD. Diphosphonates in the treatment of myositis ossificans. *Lancet*, 1969 Oct;2(7625):845.
42. Guyatt GH, Cranney A, Griffith L, Walter S, Krolicki N, Favus M, and Rosen C. Summary of meta-analyses of therapies for postmenopausal osteoporosis and the relationship between bone density and fractures. *Endocrinol Metab Clin North Am*, 2002 Sep;31(3):659–79, xii.
43. Lipton A. Implications of bone metastases and the benefits of bone-targeted therapy. *Semin Oncol*, 2010 Oct;37 Suppl 2:S15–29.
44. Silverman SL. Paget disease of bone: therapeutic options. *J Clin Rheumatol*, 2008 Oct;14(5):299–305.
45. Drake MT, Clarke BL, and Khosla S. Bisphosphonates: mechanism of action and role in clinical practice. *Mayo Clin Proc*, 2008 Sep;83(9):1032–45.
46. Body JJ, Diel IJ, Lichinitzer M, Lazarev A, Pecherstorfer M, Bell R, Tripathy D, and Bergstrom B. Oral ibandronate reduces the risk of skeletal complications in breast cancer patients with metastatic bone disease: results from two randomised, placebo-controlled phase iii studies. *Br J Cancer*, 2004 Mar;90(6):1133–7.
47. van der Pluijm G, Que I, Sijmons B, Buijs JT, Löwik CWGM, Wetterwald A, Thalmann GN, Papapoulos SE, and Cecchini MG. Interference with the microenvironmental support impairs the de novo formation of bone metastases in vivo. *Cancer Res*, 2005 Sep;65(17):7682–90.
48. Caccamo N, Meraviglia S, Scarpa F, La Mendola C, Santini D, Bonanno CT, Misiano G, Dieli F, and Salerno A. Aminobisphosphonate-activated gammadelta t cells in immunotherapy of cancer: doubts no more. *Expert Opin Biol Ther*, 2008 Jul;8(7):875–83.
49. Naoe M, Ogawa Y, Takeshita K, Morita J, Shichijo T, Fuji K, Fukagai T, Iwamoto S, and Terao S. Zoledronate stimulates gamma delta t cells in prostate cancer patients. *Oncol Res*, 2010;18(10):493–501.
50. Thompson K, Roelofs AJ, Jauhainen M, Mönkkönen H, Mönkkönen J, and Rogers MJ. Activation of t cells by bisphosphonates. *Adv Exp Med Biol*, 2010;658:11–20.

51. Bennouna J, Bompas E, Neidhardt EM, Rolland F, Philip I, Galéa C, Salot S, Saiagh S, Audrain M, Rimbert M, Lafaye-de Micheaux S, Tiollier J, and Négrier S. Phase-I study of innacell gammadelta, an autologous cell-therapy product highly enriched in gamma9delta2 t lymphocytes, in combination with il-2, in patients with metastatic renal cell carcinoma. *Cancer Immunol Immunother*, 2008 Nov;57(11):1599–609.
52. Urban T, Bréchet JM, Capron F, Allard P, Prudent J, Lebeau B, and Rochemaure J. [wegener's granulomatosis. therapeutic indications and follow-up course. apropos of 5 cases]. *Rev Mal Respir*, 1991;8(5):487–92.
53. Antonov P, Pancheva R, and Naplatarova M. Membrane-related thermo-osmotic effect as measured by medium conductivity in isotonic cell suspensions. *J Biochem Biophys Methods*, 1990;21(4):285–8.
54. Guise TA. Antitumor effects of bisphosphonates: promising preclinical evidence. *Cancer Treat Rev*, 2008;34 Suppl 1:S19–24.
55. Shmeeda H, Amitay Y, Gorin J, Tzemach D, Mak L, Ogorka J, Kumar S, Zhang JA, and Gabizon A. Delivery of zoledronic acid encapsulated in folate-targeted liposome results in potent in vitro cytotoxic activity on tumor cells. *J Control Release*, 2010 Aug; 146(1):76–83.
56. Bosch-Barrera J, Merajver SD, Menéndez JA, and Van Poznak C. Direct antitumour activity of zoledronic acid: preclinical and clinical data. *Clin Transl Oncol*, 2011 Mar; 13(3):148–55.

8

Miscellaneous

Nederlandse Samenvatting
List of Abbreviations
Dankwoord
Curriculum Vitae
List of Publications

Nederlandse Samenvatting

Dit proefschrift beschrijft een aantal methodes om structurele veranderingen in het skelet te kwantificeren en het verloop van deze veranderingen door de tijd te volgen. Daarnaast worden er methodes beschreven die gebruikt kunnen worden voor de kwalitatieve beoordeling van botdikte en structurele afwijkingen van het bot. Ook wordt er een *in vitro* methode beschreven waarmee de eventuele effecten van stoffen op nieuw gevormde bloedvaten kan worden gemeten. De relevantie van een aantal van deze methodes wordt aangetoond door deze met succes te gebruiken in een preklinische studie naar de effecten van verschillende combinatiebehandelingen van botmetastasen van borstkanker. Een van de hoofdconclusies van deze studie is dat de stof ENMD-1198 een veelbelovende stof is voor de behandelingen van dit soort metastasen.

Sommige soorten kanker, met name die van de borst en de prostaat, zaaien bij voorkeur uit naar botweefsel. In het bot leiden deze zogenaamde botmetastasen tot een zeer specifiek ziektebeeld dat wordt gekenmerkt door ongecontroleerde botafbraak of juist overvloedige botaanmaak. De botmetastasen van borstkanker die in dit proefschrift aan de orde komen geven over het algemeen metastasen die de botafbraak sterk stimuleren.

De verhoogde botafbraak rondom botmetastasen komt doordat de tumorcellen botafbraak-stimulerende signaalmoleculen produceren en uitscheiden. Uit het afgebroken bot zelf komen vervolgens ook aantal stoffen vrij. Sommige van deze vrijgekomen stoffen stimuleren op hun beurt de tumorcellen tot groeien en tot verdere productie van botafbraak stimulerende moleculen. Op deze manier ontstaat er lokaal rond de botmetastase een vicieuze cirkel van signalen gericht op tumorgroei en botafbraak.

Een behandeling van botmetastasen is idealiter gericht tegen botafbraak, tegen de groei en overleving van tumorcellen, tegen de uitgroei van bestaande en vorming van nieuwe bloedvaten en vóór de activering van het immuunsysteem in een specifieke respons tegen de tumor. Omdat het hier gaat om zeer uiteenlopende processen is een behandeling met één stof als “magic bullet” waarschijnlijk niet haalbaar en is het noodzakelijk op zoek te gaan naar een combinatie van stoffen die gezamenlijk de gewenste behandeling vormen.

De vicieuze cirkel van botafbraak kan worden doorbroken door het geven van bisfosfonaten, een klasse moleculen die de botafbraak stil leggen. Daarnaast kan door, onder andere, het blokkeren van de vasculaire endotheliale groei factor kan ook de vorming van nieuwe bloedvaten worden afgeremd. Dit effect kan nog eens worden versterkt door het voorkomen dat endotheliale voorlopercellen, een celtype dat betrokken is bij het herstel van bestaande en vorming van nieuwe bloedvaten, door de tumor worden aangetrokken. Het immuunsysteem kan onder andere worden geactiveerd door bijvoorbeeld de immuunrespons onderdrukkende regulatorische T-cellen te inactiveren. Om het resultaat van een dergelijke combinatiebehandeling te kunnen volgen tijdens een preklinische studie zijn er meetmethodes nodig waarmee

het verloop van verschillende processen, zoals tumorgroei, angiogenese en botafbraak, door de tijd en tegelijkertijd gevolgd kunnen worden.

Moleculaire beeldvormende technieken zijn geschikt voor het verrichten van kwantitatieve en kwalitatieve bepalingen van relevante factoren in preklinische dierstudies. Deze technieken zijn veelal niet invasief. Dat betekent dat metingen meerdere momenten tijdens het verloop van een experiment kunnen worden uitgevoerd worden op een levend dier zonder dat het dier daarbij wordt opengemaakt of gedood. Daardoor is het mogelijk om met deze technieken structurele veranderingen in het skelet en andere ziekte gerelateerde processen zoals bloedvatgroei en tumorgroei te kwantificeren en het verloop daarvan door de tijd, in één en hetzelfde dier te volgen.

Röntgenfoto's en opnames gemaakt met optische beeldvormende technieken, zoals fluorescentie- en bioluminescentieopnames, zijn in principe tweedimensionaal. Tegenwoordig is het ook mogelijk om met deze technieken driedimensionale opnames te maken. Een driedimensionale Röntgenfoto is beter bekend als *computed tomografie* (CT). Driedimensionale technieken hebben een aantal voordelen ten opzichte van tweedimensionale technieken, zo geven driedimensionale technieken een realistischer weergave van de werkelijkheid en betere mogelijkheden tot kwantificering. Het is echter lastig en tijdrovend om driedimensionale datasets te analyseren. Het is bijvoorbeeld moeilijk om in een driedimensionale dataset een gestandaardiseerd deelvolume te selecteren.

Hoofdstuk 2 van dit proefschrift beschrijft een methode om in CT scans deelvolumes te selecteren en weergaves van doorsneden van botten te genereren. De methode maakt gebruik van een nieuwe, genormaliseerde, ruimte die gegenereerd is uit de scan data door het bot van interesse recht te maken en het zo te roteren dat het bot parallel loopt aan de z-as. Deze nieuwe ruimte wordt gegenereerd op basis van een handmatig gedefinieerde middellijn van het bot. Vervolgens wordt de nieuwe ruimte gecreëerd die geheel bestaat uit doorsneden onder een hoek van 90° ten opzichte van de middellijn. Deze nieuwe ruimte kan dan worden gebruikt voor het genereren van weergaven van genormaliseerde doorsneden van het betreffende bot of voor het definiëren van deelvolumes van een bot. Eventuele volumemetingen worden uitgevoerd in de originele scandataset, nadat het geselecteerde deelvolume uit de genormaliseerde data is terug geprojecteerd in de originele scandataset, dit om meetfouten als gevolg van de databewerking te voorkomen.

Een van de problemen met longitudinale studies, waarbij een dier op verschillende momenten tijdens een studie gescand wordt, is dat iedere scan gemaakt wordt terwijl het dier in een andere houding in de scanner ligt. Hoofdstuk 3 beschrijft een geautomatiseerde methode om CT data uit longitudinale studies zowel kwalitatief als kwantitatief te analyseren. Deze methode maakt onder andere gebruik van een eerder gepubliceerde methode om te compenseren voor variaties in houding waarin een het dier op verschillende momenten is gescand. Deze variaties worden gecompenseerd door een muiscatlas over het skelet van het dier in de scandataset te passen. Vervolgens wordt het skelet in de scan op basis van de atlas opgedeeld in deelvolumes en in een genormaliseerde houding gebracht. Hoofdstuk 3 beschrijft hoe binnen

deze deelvolumes een vooraf bepaald botdeel automatisch kan worden geselecteerd en hoe het volume van dit botdeel vervolgens automatisch gemeten kan worden. De meetresultaten van deze geautomatiseerde methode wijken niet significant af van meetresultaten die handmatig zijn verkregen volgens de methode uit hoofdstuk 2.

In hoofdstuk 3 wordt er ook, net als in hoofdstuk 2 gebruik gemaakt van een middellijn. In dit geval wordt de middellijn niet handmatig per scan bepaald, maar wordt een middellijn vanuit de atlas op de scandataset geprojecteerd. In de orthogonale doorsneden wordt de dikte van het corticale bot gemeten. De gemeten botdikte wordt als kleur, rood voor dik en blauw voor dun bot, op een driedimensionale reconstructie van het bot weergegeven. Deze methode om de corticale botdikte overzichtelijk weer te geven is nuttig om de locatie van osteolytische en osteoslerotische gebieden in het bot snel en eenvoudig te identificeren. Op die manier kunnen deze weergaven de onderzoeker helpen bij het vinden van gebieden die interessant zijn om nader te bestuderen met, bijvoorbeeld, histologische technieken.

CT kan worden gebruikt bij het visualiseren en kwantificeren van structurele veranderingen die als gevolg van een ziekte of een behandeling optreden. Optische beeldvormende technieken, gebaseerd op fluorescentie en bioluminescentie, geven juist meer functionele dan structurele informatie. Deze technieken kunnen onder andere worden gebruikt voor het volgen van tumorgroei of het visualiseren van moleculaire interacties en enzymatische activiteit. Om een compleet beeld te krijgen van alle structurele en functionele veranderingen tijdens een experiment is het dus nodig om de data van deze verschillende technieken met elkaar te combineren.

Naast CT zijn er een aantal beeldvormende technieken om driedimensionale data te verkrijgen. Zo zijn er bijvoorbeeld driedimensionale bioluminescentie- en fluorescentiecameras, PET, SPECT en MRI. Iedere techniek heeft zijn eigen specifieke sterke en zwakke punten. De combinatie van deze technieken biedt unieke mogelijkheden en toepassingen binnen het biologische en medisch onderzoek, maar de gecombineerde analyse van deze zeer uiteenlopende soorten data gaat gepaard met een aantal grote uitdagingen. Ieder apparaat dat wordt gebruikt om de datasets te verkrijgen komt met specifieke eisen omtrent anesthesie en positionering van het dier. Dit leidt ertoe dat het moeilijk is om het dier iedere keer in exact dezelfde houding te scannen. Dit wordt helemaal onuitvoerbaar als een dier op meerdere momenten tijdens een proef gescand moet worden. Ook wanneer er speciaal ontwikkelde houders gebruikt worden waar het dier in kan worden gelegd blijken er toch nog verschillen in houding aan te zijn.

De hoofdstukken 2 en 3 van dit proefschrift beschrijven methodes om te compenseren voor de variatie in houding in CT datasets. In hoofdstuk 4 wordt meer ingegaan op een geïntegreerde verwerking van datasets die zijn verkregen met verschillende technieken. Het skelet wordt telkens gebruikt als referentiekader bij het compenseren van variaties in houding. Als gevolg is de verwerking van PET-, SPECT-, MRI-, bioluminescentie- en fluorescentiedata nu nog afhankelijk van een gelijktijdig verkregen CT dataset. Het verwerken van MRI data is in theorie mogelijk zonder een CT scan omdat deze datasets naast zacht weefsel contrast ook specifieke informatie

over het skelet bevatten.

Naast de hierboven beschreven technieken om het effect van behandelingen op verschillende processen *in vivo* te beoordelen is het ook belangrijk om de effectiviteit van stoffen vooraf *in vitro* te testen. Om te evalueren wat de effecten zijn van stoffen op de uitgroei van bloedvaten zijn er tal van *in vitro* tests beschikbaar. De meeste van deze tests zijn gebaseerd op het meten van de groeisnelheid van endotheel cellen, bijvoorbeeld HUVECs. Naast de groeisnelheid kan er als maat van angiogenese ook gekeken worden naar het vermogen van deze cellen om in een driedimensionale matrix buisachtige structuren te vormen. Angiogenese is echter een complex proces waar vele celtypes bij betrokken zijn. Bovendien kunnen stoffen niet alleen de uitgroei van vaten beïnvloeden, maar ook effecten hebben op nieuw gevormde vaten.

In hoofdstuk 5 wordt een *in vitro* test beschreven die als doel heeft het specifieke effect van stoffen op bestaande vaten te meten. Deze test is een uitbreiding op een eerder beschreven test om het effect van stoffen op de uitgroei van bloedvaten te meten. Beide tests zijn uniek omdat er gebruik wordt gemaakt van *ex vivo* groeiende embryonale botjes. Deze botjes bevatten alle celtypes bevatten die betrokken zijn bij bloedvatgroei. De vaten die uit deze botjes groeien zijn goed te vergelijken met het soort bloedvaten dat wordt aangetroffen in tumoren omdat in beide gevallen ondersteunende cellen en structuren, zoals bijvoorbeeld pericyten en glad spierweefsel, ontbreken. De test beschreven in hoofdstuk 5 is de eerste test om effecten van stoffen op bestaande vaten te meten in een systeem waarin diverse celtypes aanwezig zijn.

Zowel de *in vitro* test voor het meten van effecten van stoffen op bloedvatvorming en bestaande vaten als de CT analyse methodes zijn gebruikt in hoofdstuk 6 voor de evaluatie van diverse combinatiebehandelingen van osteolytische botmetastasen van borstkanker. De combinatiebehandeling is zo samengesteld dat alle relevante processen voor de groei van botmetastasen in theorie worden geremd. Deze processen zijn tumorgroei, de uitgroei en vorming van nieuwe bloedvaten en botafbraak. De combinatiebehandeling bestond uit ENMD-1198 (een 2-methoxyestraadiol (2ME2)-achtige stof), lage dosis cyclofosfamide (CTX), en het bisfosfonaat risedronaat (BP).

2ME2 is een stof die interfereert met de microtubuli van het cytoskelet van cellen. Op die manier werkt 2ME2 antiproliferatief op snel delende cellen zoals kankercellen en geactiveerde endotheelcellen tijdens angiogenese. Bovendien maakt 2ME2 cellen gevoeliger voor geprogrammeerde celdood (apoptose). Daarnaast is het aangetoond dat 2ME2 *in vivo* de groei van de borstkanker cellijnen 4T1 en MDA-MB-231 kan remmen. 2ME2 beschermt het bot ook tegen botafbraak. Dit laatste komt doordat 2ME2 de differentiatie van nieuwe osteoclasten remt en apoptose veroorzaakt in bestaande osteoclasten. Het beschermende effect van 2ME2 op het bot is ook aangetoond in diermodellen voor postmenopauzale osteoporose en postmenopauzale reumatoïde artritis. ENMD-1198 is een licht gewijzigde vorm van 2ME2 die stabiel is en een sterkere cytotoxische werking heeft dan 2ME2. De mogelijke effecten van ENMD-1198 op bot zijn echter nooit onderzocht.

Lage dosis CTX heeft, in tegenstelling tot de traditionele maximum dosis, geen direct effect op de tumorcellen. Lage dosis CTX remt de uitgroei en vorming van nieuwe

bloedvaten doordat het cytotoxisch is voor geactiveerd endotheel en circulerende endotheliale voorlopercellen. Daarnaast is lage dosis CTX cytotoxisch voor regulatoire T-cellen. Dit is een celtype dat de immuunrespons kan remmen. Door deze cellen weg te halen wordt het dus makkelijker om een tumor specifieke immuunrespons te veroorzaken.

Om de vicieuze cirkel van botafbraak te doorbreken werd in hoofdstuk 6 gebruik gemaakt van het BP risedronaat. BPs worden in de kliniek gebruikt voor de behandeling van bijvoorbeeld osteoporose. BPs binden aan het skelet en remmen vervolgens de osteoclasten.

In de studie beschreven in hoofdstuk 6 werd in een preklinisch model gebruik gemaakt van ENMD-1198 bij de behandeling van botmetastasen. In dit model worden botten geïnoculeerd met de bot specifieke osteolytische borstkanker cellijn MDA-BO2. De MDA-BO2 cellijn is een subkloon van de MDA-MD-231 cellijn, een veel gebruikt model voor borstkanker. In het hoofdstuk wordt aangetoond dat ENMD-1198 een gunstig effect heeft op de tumorgroei, bloedvatvorming en botafbraak.

Naast de effecten van ENMD-1198 op de groei van osteolytische botmetastasen werd er ook gekeken naar het effect van diverse combinatiebehandelingen met ENMD-1198, CTX en BP. De resultaten beschreven in hoofdstuk 6 laten zien dat de combinatiebehandeling van ENMD-1198 en lage dosis CTX niet veel effectiever is dan een behandeling met ENMD-1198 alleen. Daar dient bij te worden opgemerkt dat deze experimenten zijn uitgevoerd in een diermodel zonder immuunsysteem terwijl het werkingsmechanisme van lage dosis CTX wel deels via het immuunsysteem loopt. Het toevoegen van BP behandeling aan de combinatie leidde niet tot een significante verbetering van het behandelingsresultaat. Waarschijnlijk komt dit doordat de behandeling met ENMD-1198 al een sterk effect op het bot had.

Hoofdstuk 6 is naast de biologische betekenis een voorbeeld van hoe de technieken die staan beschreven in de hoofdstukken 2 en 5 kunnen worden gebruikt binnen het kankeronderzoek.

List of Abbreviations

2D	Two Dimensional
2ME2	2-Methoxyestradiol
3D	Three Dimensional
4-HC	Hydroxyperoxycyclophosphamide
μ CT	Micro-Computed Tomography
ABPs	Activity-Based Probes
APR	Articulated Planar Reformation
BLI	Bioluminescence Imaging
BMP	Bone Morphogenic Protein
BP	Bisphosphonate
CA4P	Combretastatin Analog A4 Phosphate
CEPs	Circulating Endothelial Progenitor Cells
CT	Computed Tomography
CTX	Cyclophosphamide
CV	Coefficient of Variation
EPCs	Endothelial Progenitor Cells
FCS	Fetal Calf Serum
FGF	Fibroblast Growth Factor
FLI	Fluorescence Imaging
FMT	Fluorescence Molecular Tomography
HE	Hematoxylin Eosin
HIF-1 α	Hypoxia-Inducible Factor-1 α
HUVECs	Human Umbilical Vein Endothelial Cells
IGF	Insulin-Like Growth Factor
M-CSF	Macrophage Colony-Stimulating Factor

MMP	Matrix Metalloproteinase
MPR	Multi-Planar Reformation
MRI	Magnetic Resonance Imaging
MTA	Microtubule Targeting Agent
NIR	Near Infra-Red
PBS	Phosphate Buffered Saline
PCR	Polymerase Chain Reaction
PDGF	Platelet Derived Growth Factor
PET	Positron Emission Tomography
PTHrP	Parathyroid Hormone-Related Protein
RANK	Receptor Activator for Nuclear Factor- κ B
RANKL	Receptor Activator for Nuclear Factor- κ B Ligand
ROI	Region of Interest
SEER	Surveillance Epidemiology and End Results
SEM	Standard Error of the Mean
SMA	Small Molecule Agents
SNR	Signal to Noise Ratio
SPECT	Single Photon Emission Computed Tomography
STAT3	Signal Transducer and Activator of Transcription 3
T _{reg}	Regulatory T-Cells
TGF- β	Transforming Growth Factor- β
TSP-1	Thrombospondin-1
VDA	Vascular Disruptive Agent
VEGF	Vascular Endothelial Growth Factor
VOI	Volume of Interest

Dankwoord

Een proefschrift schrijven doe je niet alleen. Dit is te onder andere te zien aan het aantal auteurs en vernoemingen in de *acknowledgements* per hoofdstuk. Maar, de conclusie dat de mensen die op deze plaatsen genoemd worden de enige zijn die een waardevolle contributie aan mijn promotie hebben geleverd zou te kort door de bocht zijn. Daarom wil ik hier van de gelegenheid gebruik maken om een aantal mensen hier alsnog te bedanken. Het gevaar van dit soort lijstjes is natuurlijk dat je niet iedereen kan noemen. Ik hoop dat zij die vergeten zijn mij dit niet kwalijk nemen.

Allereerst ben ik mijn promotores en copromotores dankbaar voor de mogelijkheid om dit promotie onderzoek uit te voeren en de altijd inspirerende begeleiding. Daarnaast wil ik iedereen die op het lab rondloopt bedanken voor hun gezelligheid en constante bereidwilligheid een helpende hand te bieden. In het bijzonder wil ik daarbij noemen: Chris voor alle onmogelijke bestellingen, Hetty voor het bijbrengen van duizend-en-één laboratoriumvaardigheden, Henny voor de vele botjes en hilarische momenten als alles mis lijkt te gaan, Ivo voor alle zuurstof die ik op het LGP 's nachts per ongeluk uit de fles heb laten lopen, Laura for her enthusiasm, smile and great scientific advice, Isabel voor het (bijna) altijd bereid zijn om in de avonden en weekeinden door te werken en de uitstekende pizza-keuze. En als laatste Stijn en Pieter, de afgelopen tijd vormden we een perfect team en de komende tijd gaan we nog veel meer mooie dingen doen in PDT-land.

Naast het harde werken is het ook van belang om voldoende afleiding te hebben. Gelukkig kon ik daarbij altijd vertrouwen op mijn kamergenoten van C4-67. Zo maar een moment op de kamer: Antoon dweilt zijn derde kop koffie van de dag op, terwijl ik probeer te voorkomen dat Linda de verwarming omhoog draait. Datzelfde moment is Marjolein bezig om de laatste feitjes van een eerder gevoerde discussie op te zoeken en roept Jitske dat we al te laat zijn voor de stresscommissie. Ondertussen is Esther aan de telefoon met een van haar patiënten en voeren Andrea en Maria een uitvoerige discussie (of is het ruzie?) over de lijn van hun nieuwe artikel. Na een vermoeiende dag kon ik dan 's avonds rustig aanschuiven bij Patrick in het restaurant om bij te komen, de week door te nemen en snode diplomatieke plannen te smeden.

Ook buiten het LUMC moet ik een aantal mensen speciaal bedanken. Duarte, thanks for all the nice movies, dinners, museum visits and your support over the last years. Richard, we moeten snel weer een tripje maken naar Keulen, Berlijn of München. Janneke en Evelien bedankt voor alle mooie momenten in zee en in Friesland. Valerius en BSO, dank voor alle muzikale momenten. Sebby en Sebas, bedankt voor het lekkere eten en drinken uit alle windstreken (met name Zuid Afrika). Debbie en Caroline, tijdens mijn studie stonden jullie als huisgenootjes altijd aan mijn zijde, nu doen jullie dat als paranimfen en in de toekomst doen jullie dat hopelijk nog steeds met een advocaatje in Huize Avondrood.

Als laatste wil ik mijn familie bedanken voor alle steun en vertrouwen. Papa, mama, André, Edwin, Joke, Renske, Lizan en Veerle, zonder jullie had ik het nooit zo ver kunnen brengen. Het is klaar, laten we snel een hapje gaan eten.

Curriculum Vitae

Thomas Jan Adriaan Snoeks is geboren op 19 februari 1981 te Naarden. Hij heeft zijn middelbare schooltijd doorgebracht op het Willem de Zwijger College te Bussum alwaar hij in 1999 zijn VWO diploma behaalde.

Najaar 1999 begon hij aan zijn studie Biomedische Wetenschappen aan de Universiteit Leiden. Tijdens zijn studie heeft hij drie onderzoeksstages verricht. De eerste stage was aan de afdeling Parasitologie van het Leids Universitair Medisch Centrum onder leiding van Dr. A.M. Polderman, de tweede stage was aan de afdeling Endocrinologie en Stofwisselingsziekten van het LUMC onder leiding van Prof. Dr. C.W.G.M. Löwik en de derde stage bij Regeneron Pharmaceuticals (Tarrytown NY, Verenigde Staten) onder leiding van Dr. A.N. Economides.

De Bachelor Biomedische Wetenschappen werd gevolgd door een Master Biomedische Wetenschappen met als specialisatie Science Based Business. Tijdens deze master heeft hij extra keuzevakken gevolgd die oriënteren op het ondernemerschap in de technologische sector. De master Biomedische Wetenschappen werd eind 2006, begin 2007 afgesloten met een afstudeerstage bij TI Pharma (Leiden) waar hij heeft gewerkt aan opzetten van de primaire werkprocessen tijdens de opstartfase van het instituut. Tijdens zijn studie is hij altijd enthousiast als violist betrokken geweest bij het Leids Studenten Koor en Orkest Collegium Musicum.

Na zijn afstuderen begon hij voorjaar 2007 aan zijn promotieonderzoek aan de afdeling Endocrinologie en Stofwisselingsziekten van het LUMC onder leiding van Prof. Dr. C.W.G.M. Löwik. Dat onderzoek was gericht op toepassingen van nieuwe beeldanalyse methodes binnen het onderzoek naar nieuwe behandelingen van botmetastasen van borstkanker. Dit onderzoek heeft geleid tot het huidige proefschrift. Inmiddels is Thomas als postdoc werkzaam in het LUMC waar hij onderzoek doet naar photodynamische therapie in combinatie met tumor specifieke nanodeeltjes.

List of Publications

CT-based handling and analysis of pre-clinical multi-modality imaging data of bone metastases.

Snoeks TJA, Baiker M, Kaijzel EL, Lelieveldt BPF, Löwik CWGM.
IBMS BoneKey, in press.

Dual-wavelength imaging of tumor progression by activatable and targeting near-infrared fluorescent probes in a bioluminescent breast cancer model.

Xie BW, Mol IM, Keereweer S, Van Beek ER, Que I, Snoeks TJA, Chan B, Kaijzel EL, Löwik CWGM.
Plos One. 2012 Feb;7(2):e31875.

Bioluminescence imaging of bone metastasis in rodents.

Snoeks TJA, van Beek E, Que I, Kaijzel EL, Löwik CWGM.
Methods Mol Biol. 2012;816:507-15.

Normalized volume of interest selection and measurement of bone volume in MicroCT scans.

Snoeks TJA, Kaijzel EL, Que I, Mol IM, Löwik CWGM, Dijkstra J.
Bone. 2011 Dec;49(6):1264-9.

Automated bone volume and thickness measurements in small animal whole-body micro-CT data.

Baiker M and Snoeks TJA, Kaijzel EL, Que I, Dijkstra J, Lelieveldt BPF, Löwik CWGM.
Mol Imaging Biol. 2011 Oct 13.

Pre-clinical optical imaging and MRI for drug development in alzheimer's disease.

Rotman M, Snoeks TJA, Van der Weerd L.
Drug Disc Today. Summer 2011;8(2-4):e117-25.

Detection of oral squamous cell carcinoma and cervical lymph node metastasis using activatable near-infrared fluorescence agents.

Keereweer S, Mieog JSD, Mol IM, Van Driel PBAA, Snoeks TJA, Baatenburg de Jong RJ, Vahrmeijer AL, Kerrebijn JDF, Löwik CWGM.
Arch Otolaryngol Head Neck Surg. 2011 Jun;137(6):609-15.

Optical image-guided surgery – where do we stand?

Keereweer S, Kerrebijn JDF, van Driel PBAA, Xie B, Kaijzel EL, Snoeks TJA, Que I, Hutteman M, van der Vorst JR, Mieog JSD, Vahrmeijer AL, van de Velde CJH, Baatenburg de Jong RJ, Löwik CWGM.

Mol Imaging Biol. 2011 Apr;13(2):199-207.

2-methoxyestradiol analogue ENMD-1198 reduces breast cancer-induced osteolysis and tumor burden both *in vitro* and *in vivo*.

Snoeks TJA, Mol IM, Que I, Kaijzel EL, Löwik CWGM.

Mol Cancer Ther. 2011 May;10(5):874-82.

Optical advances in skeletal imaging applied to bone metastases.

Snoeks TJA, Khmelinskii A, Lelieveldt BPF, Kaijzel EL, Löwik CWGM.

Bone. 2011 Jan;48(1):106-14.

Chapter 12 “In Vivo” Molecular Imaging.

Kaijzel EL, Snoeks TJA, Que I, Baiker M, Kok P, Lelieveldt BPF, Löwik CWGM.

Chemiluminescence and Bioluminescence, The Royal Society of Chemistry 2010, page 425-42.

‘*In vivo*’ optical approaches to angiogenesis imaging.

Snoeks TJA, Löwik CWGM, Kaijzel EL.

Angiogenesis. 2010 Jun;13(2):135-47.

An *in vitro* model that can distinguish between effects on angiogenesis and on established vasculature: actions of TNP-470, marimastat and the tubulin-binding agent Ang-510.

van Wijngaarden J and Snoeks TJA, van Beek E, Bloys H, Kaijzel EL, van Hinsbergh VWM, Löwik CWGM.

Biochem Biophys Res Commun. 2010 Jan 8;391(2):1161-5.

Multimodal imaging and treatment of bone metastasis.

Kaijzel EL, Snoeks TJA, Buijs JT, van der Pluijm G, Löwik CWGM.

Clin Exp Metastasis. 2009;26(4):371-9.

